Università degli Studi di Catania
Scuola Superiore di Catania

International PhD

in

Nuclear and Particle Astrophysics

XXIV cycle

Multispacecraft observations of Coronal Mass Ejections

ANDREA ORLANDO

Coordinator of PhD

Prof. Umberto Lombardo

Tutor

Prof. Francesca Zuccarello

ANNO ACCADEMICO 2010-2011

To my family

CONTENTS

«Se non che la scienza è vana se non è utile, e la meteorologia è fortunatamente di quelle scienze da cui l'umanità può ricever grandi ed utili servigi. È vero che lo scienziato non può impedire la formazione delle burrasche, né variare il regime delle piogge, può però cogli avvisi prevenire molti danni delle tempeste e ciò non solo in terra, ma molto più in mare»

Angelo Secchi, *1875*.

INTRODUCTION

The Sun-Earth environment is strongly influenced by the coupling level between the Earth magnetosphere and the interplanetary magnetic field. The latter is closely related to the solar wind, a flux of plasma continuously flowing from the Sun and propagating in the interplanetary space medium. This plasma is constituted by electrons, protons and heavier particles, and propagates with a speed of 400-800 km/s, reaching Earth in 2.4 – 4.6 days.

A sudden increase of the solar wind's speed is achieved by two types of phenomena: flares and Coronal Mass Ejections (CMEs).

Flares are strong explosions that involve different layers of the solar atmosphere: they are due to a sudden release of energy (10^{22}-10^{25}J) in areas previously characterized by variations in the configuration of the magnetic field. Flares have an evolution time variating from 10 minutes to some hours. The phenomena that occurr during a flare produce heating of the chromospheric and coronal plasma and intense electric fields that accelerate charged particles.

Coronal Mass Ejections (CMEs) are expulsions of material from the solar corona and, from an energetic point of view, they reach the same order of magnitude of the flares; they can moreover pour in the space up to many billion tons of coronal plasma. Such phenomena can occur many times a day and can accelerate the solar plasma up to 3000 km/s. Even if they have been extensively studied since their discovery, back in the '70s, a complete model for their explanation is still lacking. From our present knowledge, it seems that CMEs are strongly linked to the photospheric (sunspots, active regions), chromospheric (filaments) and coronal (flares) activity.

Starting 1996, the Large Angle and Spectrometric COronograph (LASCO) instrument, on board of the SOlar and Heliospheric Observatory (SOHO) satellite, permitted for the first time to observe the corona with a large field of view, in the range of about 1.1 to 30 solar radii. Moreover observations at different wavelengths (visible, X and EUV bands) are of primary interest in the study of a CME development from its initial phase, in lower corona, to great distances from the Sun.

The online Goddard Space Flight Center catalogue (GSFC/NASA) contains data about the CMEs observed by the LASCO coronographs when the SOHO satellite was lying in the lagrangean point L1 of its orbit. These data can nowadays be correlated to the ones taken by the two twin Solar TErrestrial RElations Observatory (STEREO) satellites, that allow a stereoscopic view of CMEs.

In this context, this thesis concerns the study of the physical processes that lie at the base of the CME formation and of their effects on the Sun-Earth environment. Such an investigation can be done utilizing data taken from satellites that study solar wind, interplanetary magnetic field, flares and CMEs.

A source of data lies in the Sun Earth Connection and Heliospheric Investigation (SECCHI) remote sensing instruments, onboard of the STEREO-A and STEREO-B satellites. SECCHI allows the realization of synchronization techniques for the two satellites and the construction of stereoscopic pictures, that can be employed to build a 3-D description of the Sun and of the 1 AU heliosphere.

Another source of data is the Michelson Doppler Imager (MDI) instrument onboard of SOHO satellite: MDI provides magnetograms that are useful to study the magnetic configuration of active regions. Moreover, the Auger Observatory and others neutron monitor stations are used for the detection of cosmic rays and for the analysis of the correlation between Forbush decreases and CMEs.

CHAPTER 1. *SOLAR PHENOMENA*

1.1 The Corona and the Solar Wind

The corona is the outermost region of the solar atmosphere and is located above the so-called "transition region". In the visible part of the electromagnetic spectrum, its emission is much fainter than the photosphere (about 10^{-6} $L_{\odot}$)[1] and can be commonly observed during the Sun's total eclipse (Figure 1), or using a special tool, called *coronagraph*, which shields the solar disk simulating a total eclipse.

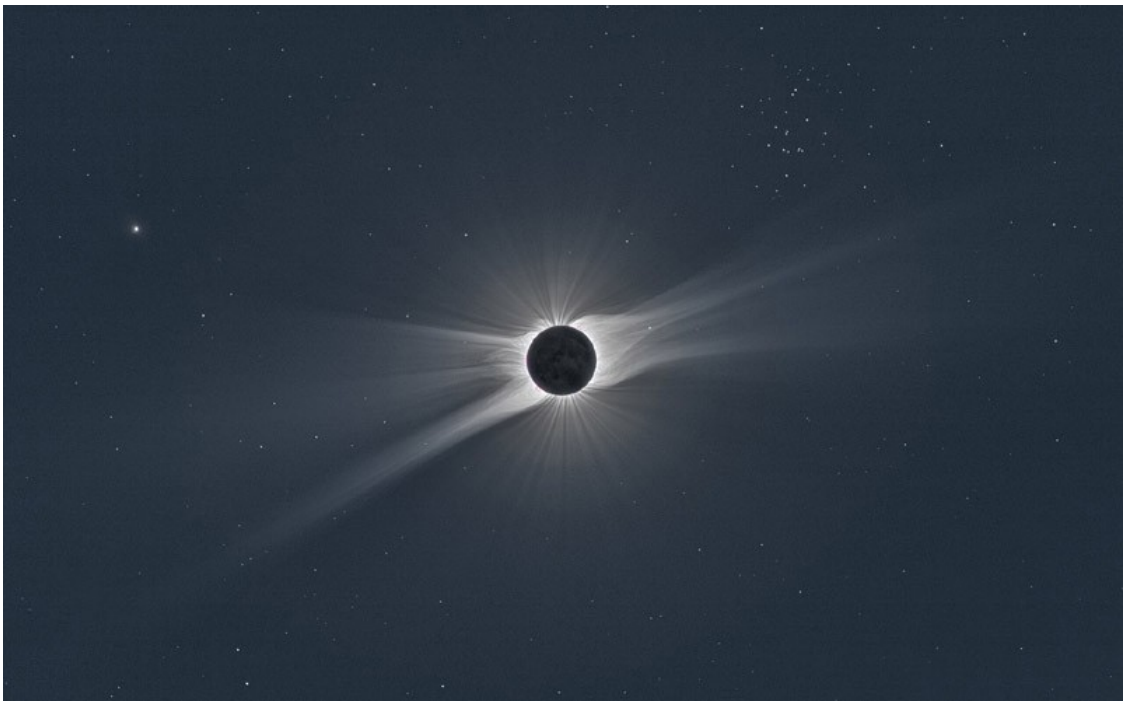

Figure 1. The corona during a total solar eclipse in 2008 (photo credit: Druckmüller, Aniol, Rušin).

However, the solar corona appears much brighter than the photosphere outside the visible spectrum, especially in X-band, EUV and radio band. The coronal plasma is a very tenuous plasma (density of the order of 10^{14} particles m^{-3}), characterized by a temperature of about $1.5\text{-}2 \cdot 10^{6}$ K.

[1] $L_{\odot}$ refers to the brightness of the Sun: $L_{\odot} = 3{,}84 \cdot 10^{33}$ erg/s.

The images in the X-band show that the corona consists of a set of distinct structures, which can be very different between them in terms of size and physical conditions (Figure 2).

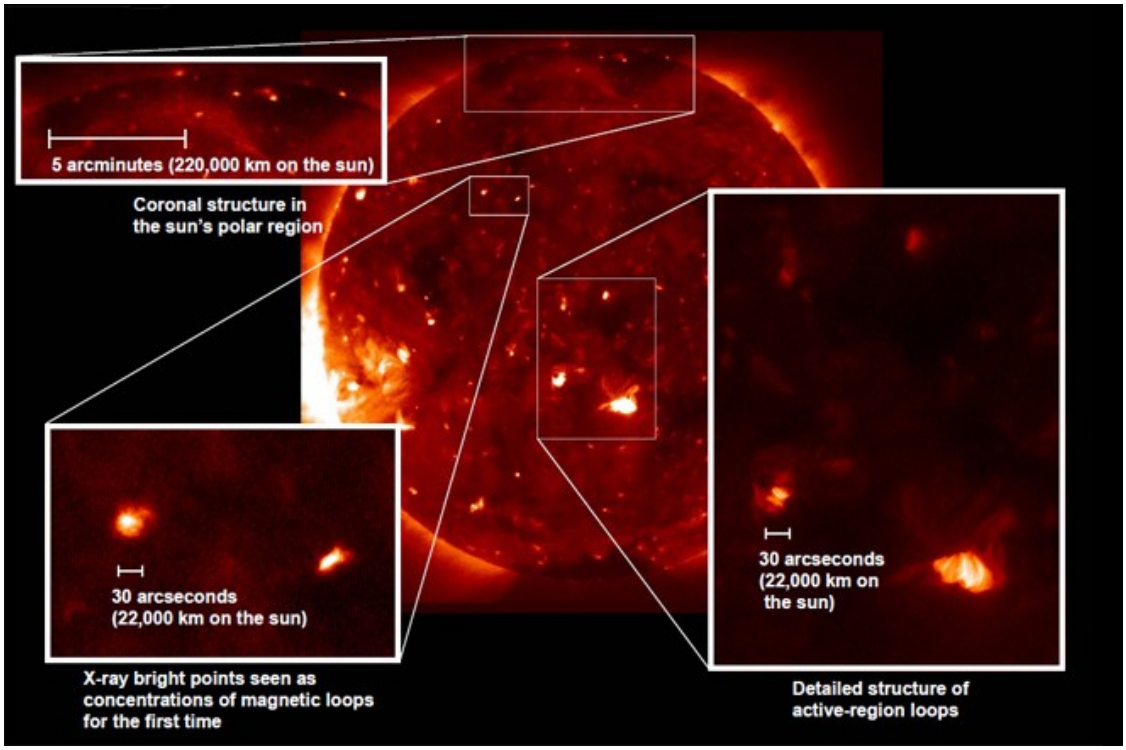

Figure 2. The solar corona observed in X-ray from the Hinode satellite.

We can distinguish *bright points* (about $2 \cdot 10^4$ km in diameter), short-lived structures (less than two days) that, unlike other typical phenomena of solar activity such as spots, are distributed evenly across the solar disk. Larger structures ($\geq 10^5$ km), of longer duration (days and weeks), which are typically associated with the spots and faculae are called *bright regions*, and are characterized by a higher density of particles and higher temperature than the surrounding coronal regions.

There are also other regions, commonly observed in the Sun's polar region and showing almost no X-ray emission, which have been called *coronal holes*. They have an average life of over six months and for this reason they are the most persistent solar phenomena. Coronal holes appear dark because their temperature and their density are smaller than the surrounding corona.

In the area below a coronal hole, the photospheric magnetic field is weak (~1 G) compared to surrounding regions and predominantly of the same polarity. The coronal holes are usually formed at the poles and then slowly extend to lower latitudes.

Contrary to what happens in bright regions, coronal holes rotate rigidly, so their angular velocity does not vary significantly with latitude and the rotation period decreases by only 3% from the pole to the equator, and is about 27 days.

The coronal holes are closely related to another phenomenon of the solar activity: the solar wind, a stream of plasma that flows continuously from the Sun and propagates in the interplanetary medium. In particular, coronal holes are the sources of the *fast solar wind*, which propagates with an average speed of 750 km/s and is relatively constant over time (Figure 3 and 4).

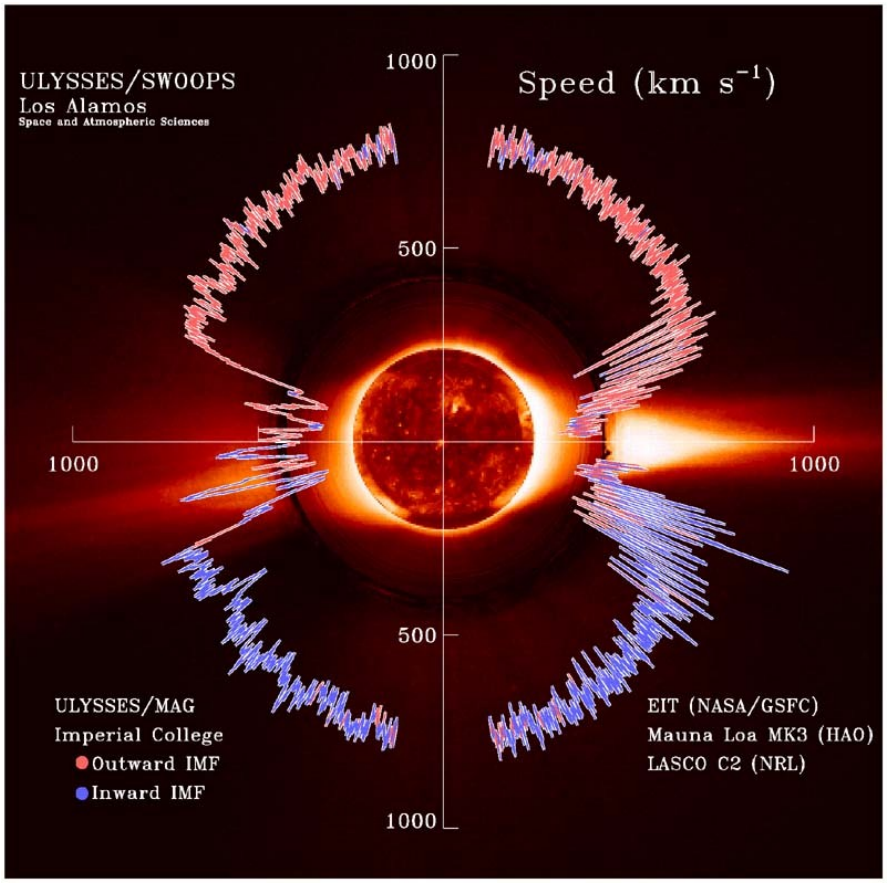

Figure 3. This composite image shows in the form of polar pattern the speed of the solar wind as a function of solar latitude, measured from Ulysses spacecraft during solar minimum of the cycle 23. The speed of the solar wind is almost constant and of the order of about 750 km/s at high solar latitudes ($|\varphi| > 30°$) while it is lower and more variable at the low latitudes. At the graph's speed is superimposed an image of the corona.

The *slow solar wind* stems from structures of closed coronal magnetic field lines, such as the *streamers*. They appear as large gothic arch-shaped structures that trap ionized coronal gas. The slow solar wind consists of particles moving at an average speed of 400 km/s and is highly variable (Figures 3 and 4).

Proton density	6.6 cm^{-3}	Gas pressure	30 pPa
Electron density	7.1 cm^{-3}	Sound speed	60 km s^{-1}
He^{2+} density	0.25 cm^{-3}	Magnetic pressure	19 pPa
Flow speed (nearly radial)	450 km s^{-1}	Alfvén speed	40 km s^{-1}
Proton temperature	$1.2 \cdot 10^5$ K	Proton-proton time collision	$4 \cdot 10^6$ s
Electron temperatue	$1.4 \cdot 10^5$ K	Electron-electron time collision	$3 \cdot 10^5$ s
Magnetic field (induction)	7 nT	Time for wind to flow from corona to 1 AU	$3.5 \cdot 10^5$ s ~ 4 days

Table 1. Observed properties of the solar wind near the orbit of the Earth (from Kivelson et al., 1995).

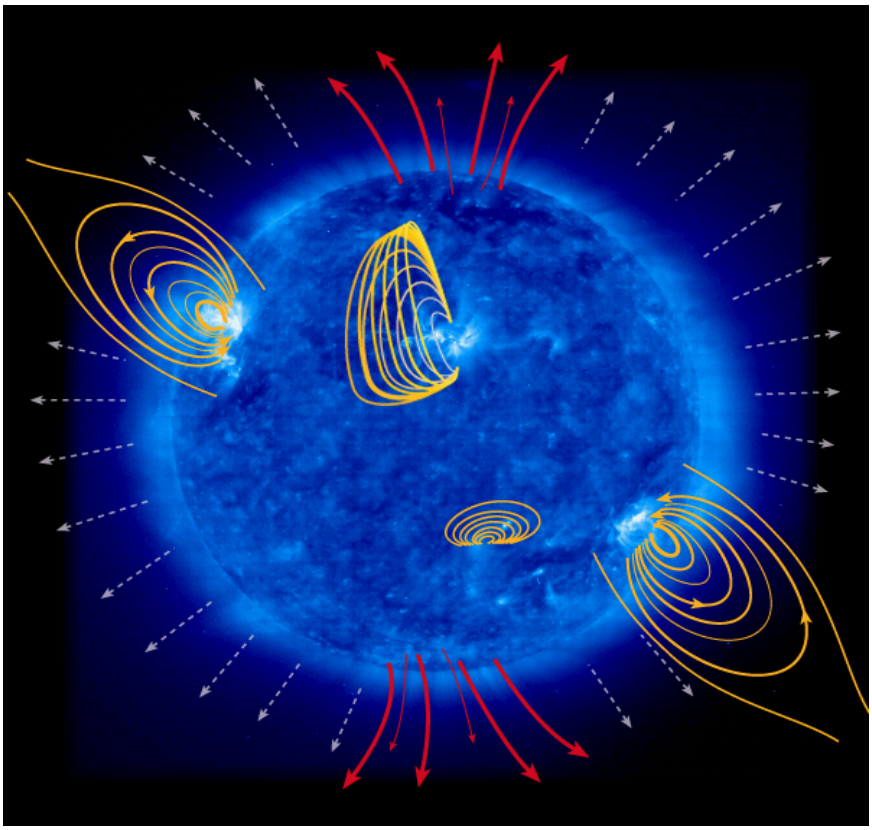

Figure 4. The Sun is permeated by magnetic fields. Red arrows indicate the open magnetic field lines emerging from the poles. The gray arrows represent the solar wind particles. The yellow arrows indicate the closed magnetic field lines of the active regions (photo credit: NASA/GSFC).

There are two classes of phenomena that can produce sudden increases in solar wind speed, they are the *flares* and the *coronal mass ejections* (CMEs).

1.2 Coronal Mass Ejections (CMEs)

CMEs are the most spectacular large-scale demonstration of solar activity and there is currently no single model that can fully explain this phenomenon, although several models have been proposed (Figures 5). The multi-wavelength observations are thought to be crucial to a complete understanding of CMEs [Hudson and Cliver, 2001]. Recently, it was proposed that Lyα line at the ultra-violet (UV) wavelength might be very suitable for the detection of CMEs [Vial et al., 2007].

The white-light emission of the corona comes from the photospheric radiation Thomson-scattered by free electrons in the corona, and any enhanced brightness means that the coronal density somewhere along the line of sight is increased.

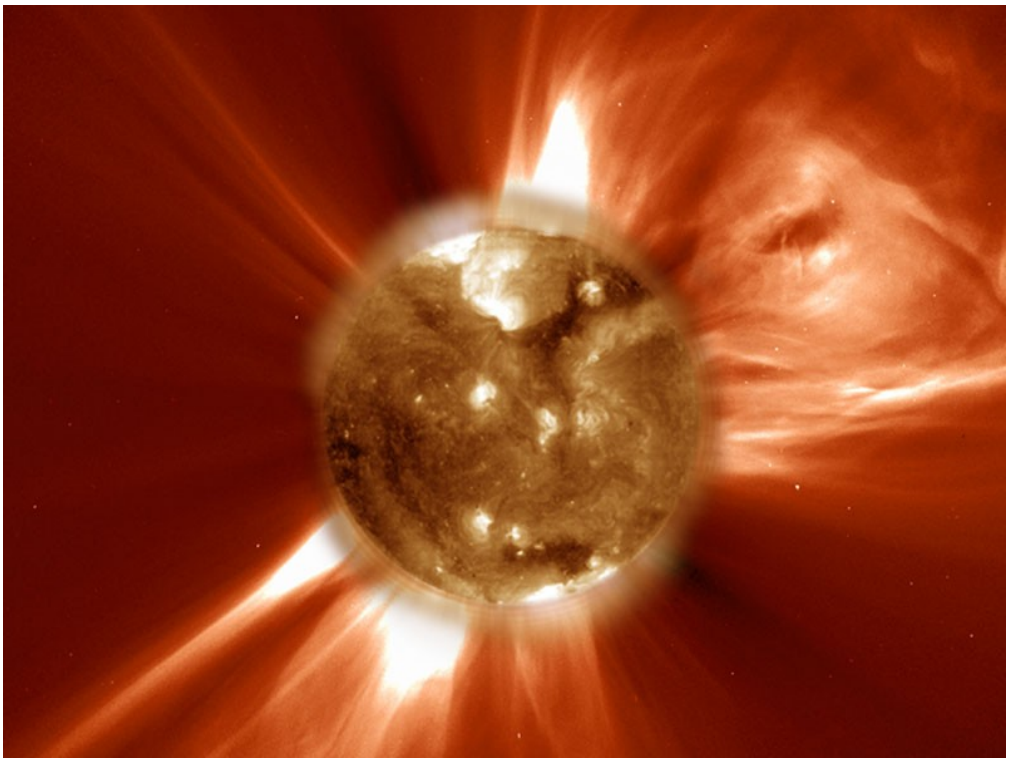

Figure 5. CME observed by SOHO in 2002. The image was taken by the LASCO C2 instrument, which blocks out the Sun with an occulting disk so that we can see the fine details of the faint corona. An EIT 284 Å image of the Sun itself, taken at about the same time, is superimposed on the occulting disk.

In addition to the density enhancement, the Thomson scattered radiation depends on the photospheric radiation incident to the electrons and the angle between the incidence and the line of sight, which makes CMEs favorably observed near the plane of the sky.

With the continual observations from various ground-based and space-born coronagraphs, more than ten thousand CME events have been recorded, which enables the statistical investigation of their properties [Chen, 2011].

Since the beginning of 1996 the instrument LASCO (Large Angle Spectrometric and Coronograph) onboard the SOHO satellite, has allowed, for the first time, to observe the corona with a large field of view, from about 1.1 to about 30 solar radii $(R_\odot)$[2].

In general, the CMEs appear as eruptions of magnetic arches that connect regions of opposite magnetic polarity on either side of a photospheric magnetic neutral line[3]. Where it is possible to observe CMEs in the low corona, we note that most of them originated from a system of two large magnetic arches. The observations of the corona in the FeXIV emission line recently showed the almost systematic quadrupolar nature of the CME [Schwenn et al., 1997]. In fact the structure of the corona is governed by the solar magnetic field and the magnetic topology is that of a simple magnetic dipole, but often multipole components are involved.

Based on the Thomson-scattering formulae [Billings, 1966], the mass of a CME can be estimated [Hundhausen, 1993]. Without the knowledge of the exact position of the density-enhanced structure, it is often assumed that the CME is close to the plane of the sky, which would underestimate the mass of the CME.

Typically, the mass of a CME falls in the range of $1 \cdot 10^{11}$–$4 \cdot 10^{13}$ kg, averaged at $3 \cdot 10^{12}$ kg [Jackson, 1985; Gopalswamy and Kundu, 1992; Hudson et al., 1996].

About 15% of the CMEs have a mass less than 10^{11} kg [Vourlidas et al., 2002]. The angular width of CMEs projected in the plane of the sky ranges widely from ~ 2° to 360° [Yashiro et al., 2004], with a significant fraction in the low end (e.g., < 20°) and a small fraction in the high end (e.g., > 120°).

[2] 1 $R_\odot$ = 696000 km.
[3] A neutral line is the locus of points where the magnetic field component along the line of sight is zero.

The observations indicate that we can divide CMEs into at least two categories. The CMEs with the angular width less than ~ 10° can be called *narrow CMEs* [Wang et al., 1998], and the others are sometimes called *normal CMEs* [Yashiro et al., 2004] (Figures 6 and 7 show the two CME's categories). Note that *halo* CMEs (see paragraph 1.2.2), with an apparent angular width of or close to 360°, might simply due to that the CMEs, probably with an angular width of tens of degrees, propagate near the Sun-Earth line, either toward or away from the Earth.

During the solar cycle 23, the LASCO provided unprecedented observations of CMEs. The occurrence rate of CMEs was found to basically track the solar activity cycle, but with a peak delay of 6-12 months [Raychaudhuri, 2005; Robbrecht et al., 2009]. Before the SOHO era, the averaged occurrence rate was found to increase from 0.2 per day at solar minimum to 3.5 per day at solar maximum [Webb and Howard, 1994].

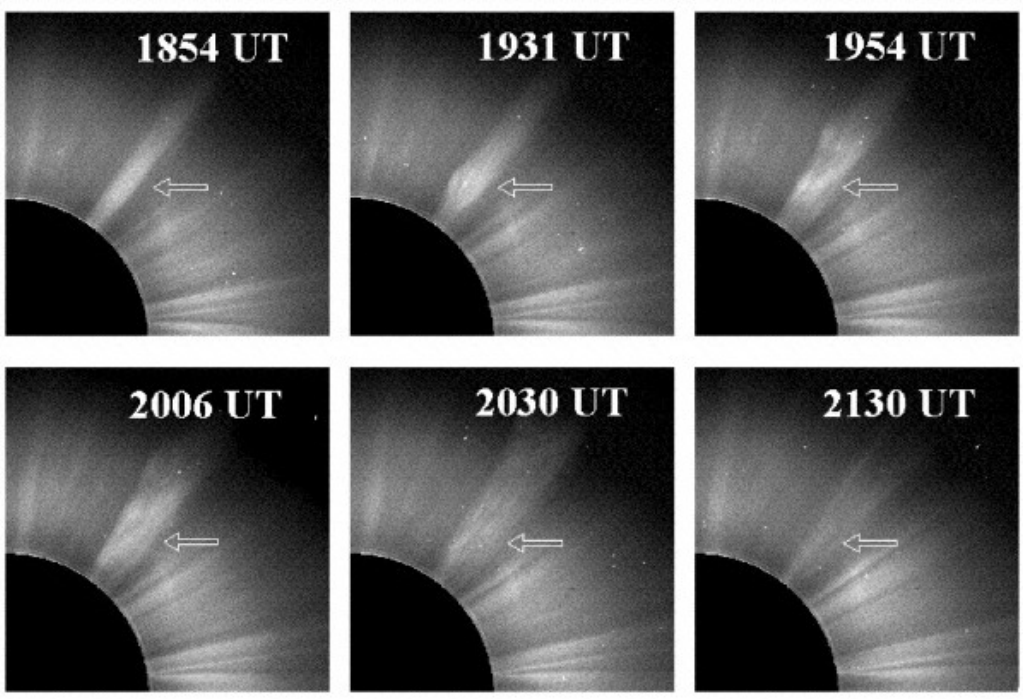

Figure 6. Example of a narrow CME seen in LASCO C2 data on 1999 April 24. Sun center is in the lower left corner of each image, and the edge of the occulting disk is at 2 $R_{\odot}$ (from Gilbert et al., 2001).

With the increased sensitivity and wider field of view, the SOHO/LASCO coronagraph assembly, including C1, C2, and C3 components with different fields of view, detected CMEs more frequently.

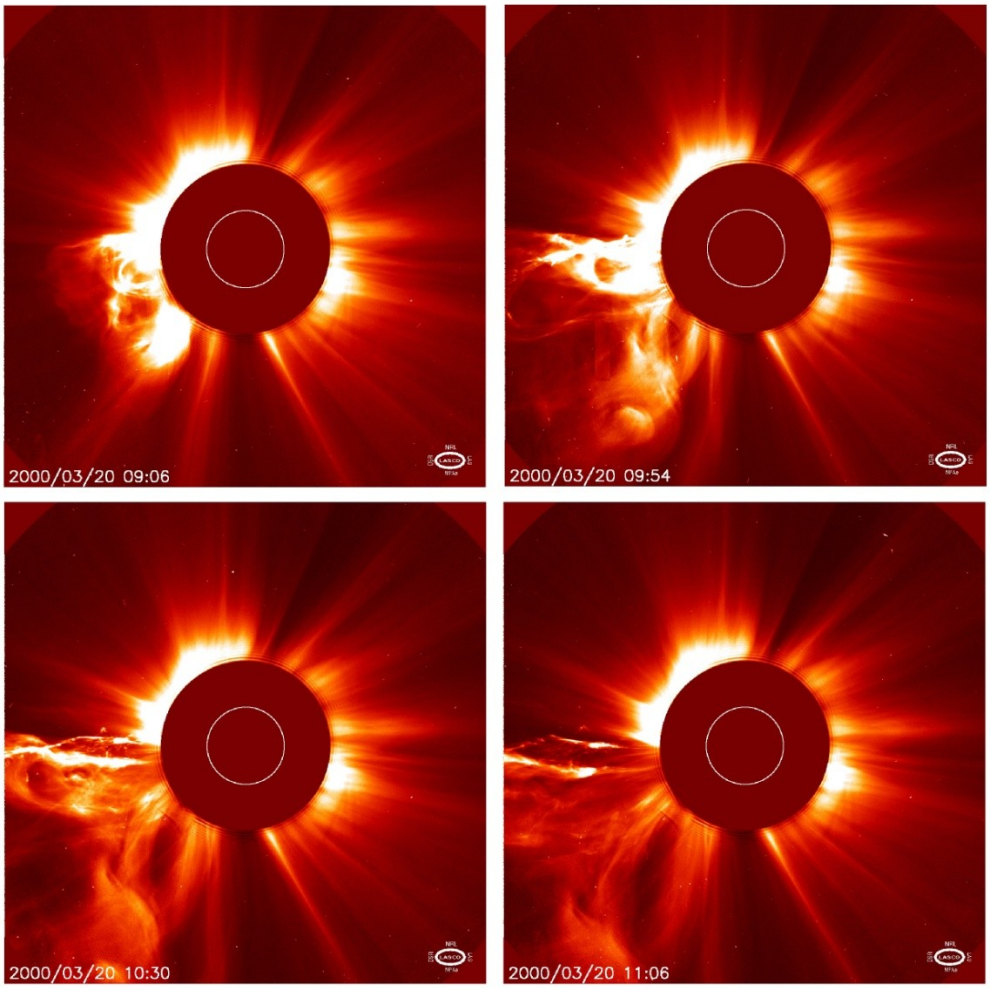

Figure 7. Example of a normal CME seen in LASCO C2 on 2000 March 20 (SOHO/LASCO).

The CME catalog in the NASA CDAW data center, where CMEs are identified by eye, shows that the CME occurrence rate increases from ~ 0.5 per day near solar minimum to ~ 6 near solar maximum, summing up to more than 13000 CMEs during the solar cycle 23 [Gopalswamy et al., 2003; Yashiro et al., 2004].

However, for the same observational period, the automated software (CACTus) identified much more events, with the occurrence rate increasing from < 2 per day near solar minimum to ~ 8 per day near solar maximum [Robbrecht et al., 2009]. Figure 8

shows the comparison of the CME daily occurrence rate detected by the two methods, along with the sunspot number.

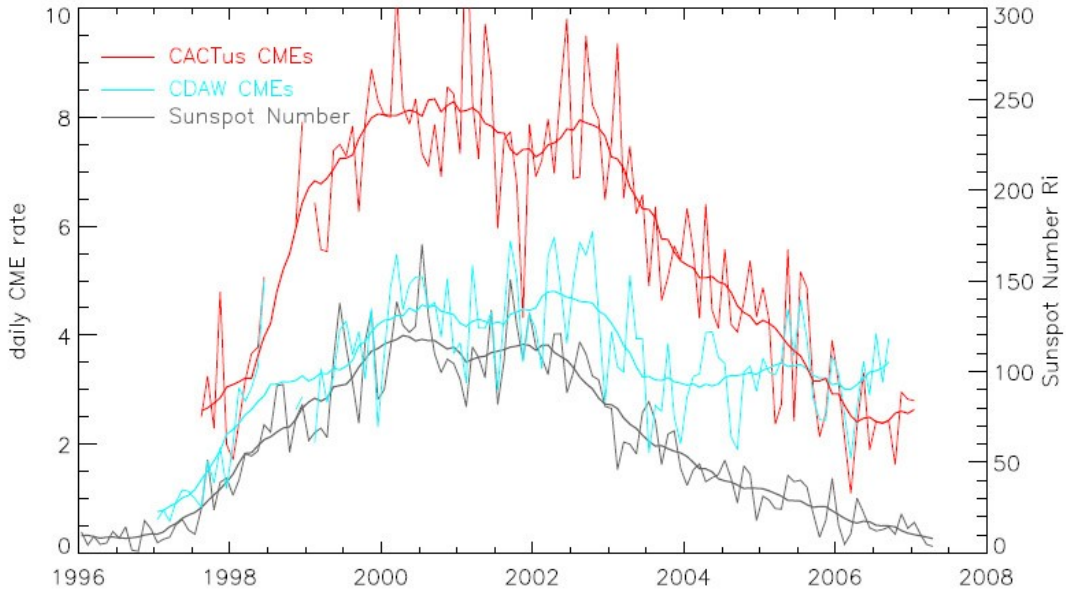

Figure 8. The CME daily occurrence rate detected by the CACTus archive (red) and the CDAW archive (blue) compared with the daily sunspot number (gray) during solar cycle 23. Thin curves: smoothed per month, thick curves: smoothed over 13 months (from Robbrecht et al., 2009).

Constructing CME models is extremely important, not only because CMEs are a spectacular astronomical phenomenon, but also because they are the main driver for the space weather disturbances that strongly affect our high-tech life. It is important to emphasize here that any successful model should be based on the combination of observations and magnetohydrodynamic (MHD) theory.

The same as any other eruptive phenomenon, CMEs, along with solar flares, involve the energy conversion from one kind to the kinetic, potential, thermal, and nonthermal energies, as well as the radiative energy in flaring loops. It should be noted that there are secondary conversions between different energies, e.g., part of the nonthermal energy would be converted into the thermal energy, which would finally radiate out. They should not be double counted when estimating the CME and flare energies. With the assumption that a typical CME involves a volume of 10^{24} m^3, the

energy density of a CME ranges from 10^{-2}–10 J m^{-3}. The typical energy density of possible energy sources is shown in Table 2 [Forbes, 2000].

Form of energy	Energy density (J m^{-3})	Observed averaged value
Kinetic ($\frac{1}{2}m_p nV^2$)	8×10^{-4}	$n = 10^{15}$ m^{-3}, $V = 1$ km s^{-1}
Thermal (nkT)	1×10^{-2}	$T = 10^6$ K
Potential ($nm_p gh$)	5×10^{-2}	$h = 10^5$ km
Magnetic ($B^2/2\mu_0$)	40	$B = 10^{-2}$ T

Table 2. Estimates of the coronal energy sources.

We can see that for energetic CME events, which are the most interesting in the space weather context, the only possible source is the magnetic energy, whereas for very weak CME events, thermal and potential energies in the pre-eruption corona may contribute to the CME explosions. In the case that these two sources are available, thermal energy is converted to the CME energy by the work of pressure gradient, similar to the acceleration of solar wind, and the potential energy is converted to the CME energy in the form of buoyancy.

In those eruptive cases, the CMEs energy comes from the partial release of the magnetic free energy, i.e., the excess energy compared to the potential field with the same flux distribution at the solar photosphere. It is demonstrated that in the case of force-free field that is often applicable in the low corona [Gary, 2001], the magnetic free energy is of the order of the magnetic energy of the corresponding potential field [Aly, 1984].

1.2.1 CME's classification

CMEs generally have a three parts structure (see Figure 9 (left)): proceeding from outside to inside, a bright loop is observed, superimposed on a coronal cavity with no emission, which in turn contains high plasma density from an eruptive prominence.

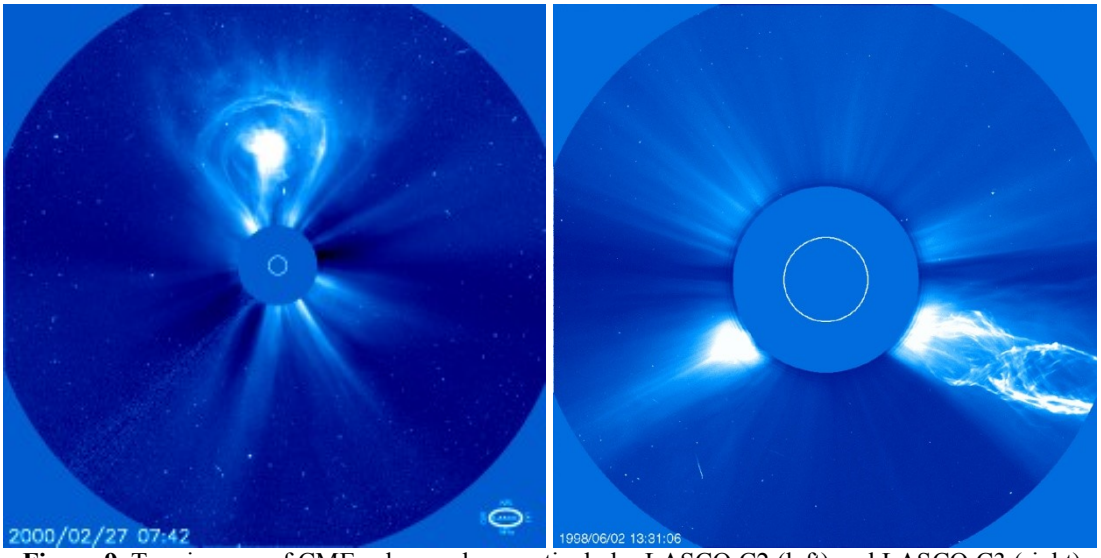

Figure 9. Two images of CMEs observed respectively by LASCO C2 (left) and LASCO C3 (right), respectively, in which the typical CME structure in three parts and the helical structure are shown.

The observations made with the instruments onboard SOHO, EIT and LASCO C1 in particular, have shown that these three components are present in the low corona during the early stages of development of a CME. In addition, many CMEs observed with LASCO instrument showed a helical structure (Figure 9 (right)). Along with these types of CMEs, others have been identified: for example, a CME that originates at a given latitude can cause the destabilization of a multi-polar region on a larger scale, and the resulting CME can cover a range of latitude exceeding 60°.

CMEs often occur in association with flares, in which case we refer to flare-CME events. During flare-CME events, accelerated electron beams that propagate along the magnetic field lines produce radio bursts. The LASCO instrument has confirmed the existence of two classes of CMEs, which have different speeds of propagation.

The first class, called *impulsive CME*, is formed by the CMEs having a high speed and a small acceleration. Speeds are typically in excess of 750 km/s. Impulsive CMEs are often associated with flares and Moreton waves[4] on the disk.

The second class, the *gradual CME*, is formed by CMEs that evolve slowly and then accelerate. Speeds are in the range of 400–600 km/s, while the accelerations measured varies from event to event and can reach up to 30 m/s^2. Gradual CMEs are

[4] A *Moreton wave* is the chromospheric signature of a large-scale solar coronal shock wave. Described as a kind of solar 'tsunami', they can be generated by solar flares.

apparently formed when prominences and their cavities rise up from below coronal streamers. The CME associated with the quiescent prominences probably fit this category. Both classes can reach speeds of 3000 km/s.

More recently, a new class of CME has been identified by LASCO. These events were seen as a slow accretion of densities that originate above the cusps of helmet streamers and move radially outward with almost constant acceleration of about 3-5 m/s^2 [Sheeley et al., 1997].

They resemble small CME evolving gradually. Based on their radial motions and the slow speed increases, besides than the fact that originate in the streamer belt, Sheeley et al. [1997] have concluded that they are the traces of the flow of slow solar wind.

In order to explain the different kinematics, Low and Zhang [2002] proposed an idea for the two types of CMEs, i.e., the normal polarity flux rope eruptions correspond to the fast CMEs, whereas the inverse polarity flux rope eruptions correspond to the slow CMEs. On the other hand, it was found that, even for the inverse type only, the CME speed can be high or low [Chen and Krall, 2003; Wu et al., 2004].

1.2.2 Halo CME

As already stated, CMEs can also manifest as events that have an angular width of ~360°, and in this case they are called *halo* events.

These types of events were identified for the first time with the coronagraph onboard the satellite P78-1 and were defined as an increase in brightness that surrounds the solar disk [Koomen et al., 1975]. The halo events are CMEs that originate close to the centre of the solar disk and are directed along the line joining the Sun and the Earth.

It is widely accepted that they are nothing but CMEs propagating near the Sun-Earth direction, either toward or away from the Earth [Howard et al., 1982]. However, statistical investigations indicate that the average velocity of halo CMEs, ~ 957 km/s,

is twice as large as that of normal CMEs (e.g., Yashiro et al., 2004), which seems to make halo CMEs special.

It may be natural to think that the nearly circular front of halo CMEs is just the face-on view of the dome-like CME frontal loop. For simplicity, we assume that the CME frontal loop is represented as the shell of a cone-shaped dome as illustrated by Figure 10 [Chen, 2011].

When it is observed edge-on as a limb event, it would appear as a loop structure, i.e., the green lines linking points A, B, C, D, and E, since the optical thickness is much larger here. When the CME is observed face-on as a halo event, however, the optical thickness is large only near the torus linking points B and D, i.e., the blue lines in Figure 10, which surrounds the solar disk to the observer. If so, the nature of halo CMEs would be the same as the normal CMEs.

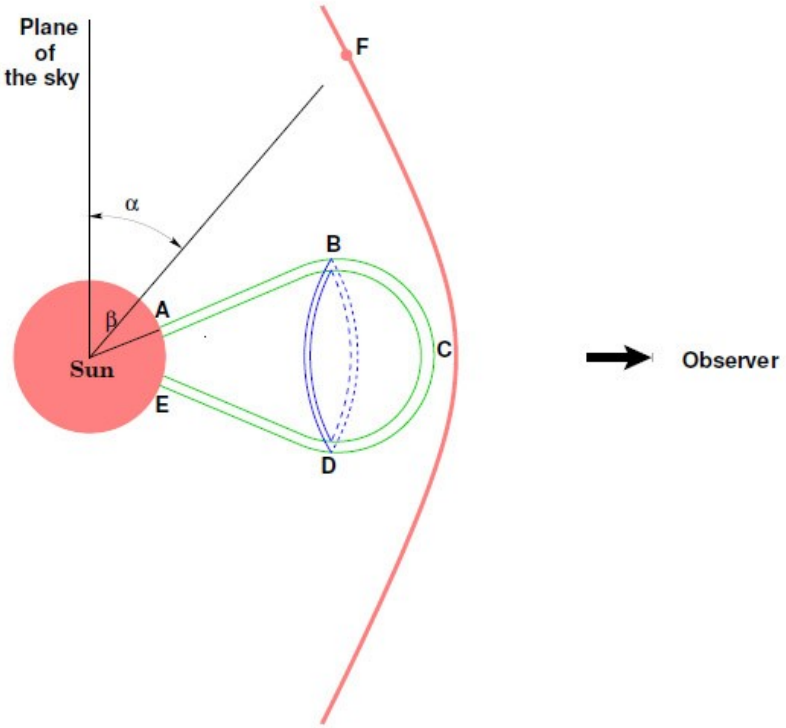

Figure 10. A sketch showing how a dome-like CME would be observed as a limb event (green lines) and as a halo event (blue lines). The red line ahead of the CME is a fast-mode piston-driven shock wave. α is the inclination angle between the radial direction of point F and the plane of the sky, whereas β is the angle between the CME leg and the plane of the sky. It is seen that the far wing, say, near point F, propagates in a direction closer to the plane of the sky than the CME does (since $\alpha < \beta$) (from Chen, 2011).

For example, Krall et al. [2006] extended the flux rope model (see Section 1.2.3), which was demonstrated to be applicable to limb CMEs [Chen, 1996; Krall et al., 2001], to halo CMEs, and found that the model can reproduce both quantitative near-Sun properties of the 2003 October 28 CME and the timing, strength, and orientation of the fields measured in situ near the Earth orbit. Of course, the nature of CME frontal loops is still under debate, and there are other possibilities, such as that the CME frontal loop is due to the compression of magnetic field lines which are stretched successively.

If the nature of halo CME fronts is the same as normal CMEs, there is a serious problem: why halo CMEs are on average twice faster than normal CMEs? Noticing that the Thomson scattering is significantly reduced for halo CMEs, Andrews [2002] proposed that many dim and slow halo CMEs are missed by coronagraphs so that the average velocity of the observed halo CMEs is high.

Following this line of thought, Zhang et al. [2010] performed Monte Carlo simulations to investigate how the white-light brightness of CMEs with an average velocity of 523 km/s is reduced when they are observed as halo events. They found that the brightness of many narrow and slow CMEs, when they are observed as full halo CMEs, is reduced to a level comparable to the solar wind fluctuations, and therefore, these events would be missed to be identified in the coronagraph images. The remaining observable halo CMEs have an average velocity of ~ 922 km/s, quite similar to the value in observations.

An alternative view is that the halo CME fronts are completely different from the frontal loops of limb CMEs in physics. For example, Lara et al. [2006] proposed that the halo CME fronts might be the combination of the CME-driven shock wave and the CME material itself. Based on MHD numerical simulations, Manchester et al. [2008] synthesized the white-light images of a halo CME event, and found that the halo CME front can be identified as the CME-driven shock wave.

Since the fast-mode wave in the corona is of the order of 1000 km/s, it easily explains why the average velocity of halo CMEs is as high as 957 km/s. One may argue that the piston-driven shock wave is much weaker in white light than the CME

frontal loop, and therefore can be barely visible in the coronal images. This is true for the limb events (e.g., Vourlidas et al., 2003).

However, for halo CMEs, as illustrated by Figure 10, the situation may change. If we consider the Thomson scattering, which remarkably favors the plasma moving in a direction closer to the plane of the sky, the scattered white-light emission of the shock wave front at point F in Figure 10 could be stronger than that of the CME frontal loop near point B when both points are observed at the same projected heliocentric distance in the plane of the sky, although the plasma density is higher at point B than point F.

1.2.3 CME's Models

The study of the CMEs has not yet allowed us to establish with certainty what is the mechanism responsible for the formation of such events. The knowledge gained through observations have led to discard the possibility of a mechanism due to a sudden increase of the plasma pressure. Current models consider a mechanism driven by a magnetic force.

Low [1996] developed a model in which a CME is a magnetic flux rope[5] expulsion which is gravitationally confined within the cavity of a helmet streamer. At a certain moment this twisted magnetic flux tube becomes unstable and starts to rise towards the outer layers of the atmosphere and blows off breaking helmet streamer's field lines. This study led to the elaboration of a three-dimensional MHD flow of a flux rope, and simulations show the characteristic three components structure of the CME (Figure 11).

[5] A magnetic flux rope can be defined as a structure consisting of magnetized plasma, with a shape similar to a twisted rope (see Figure 11).

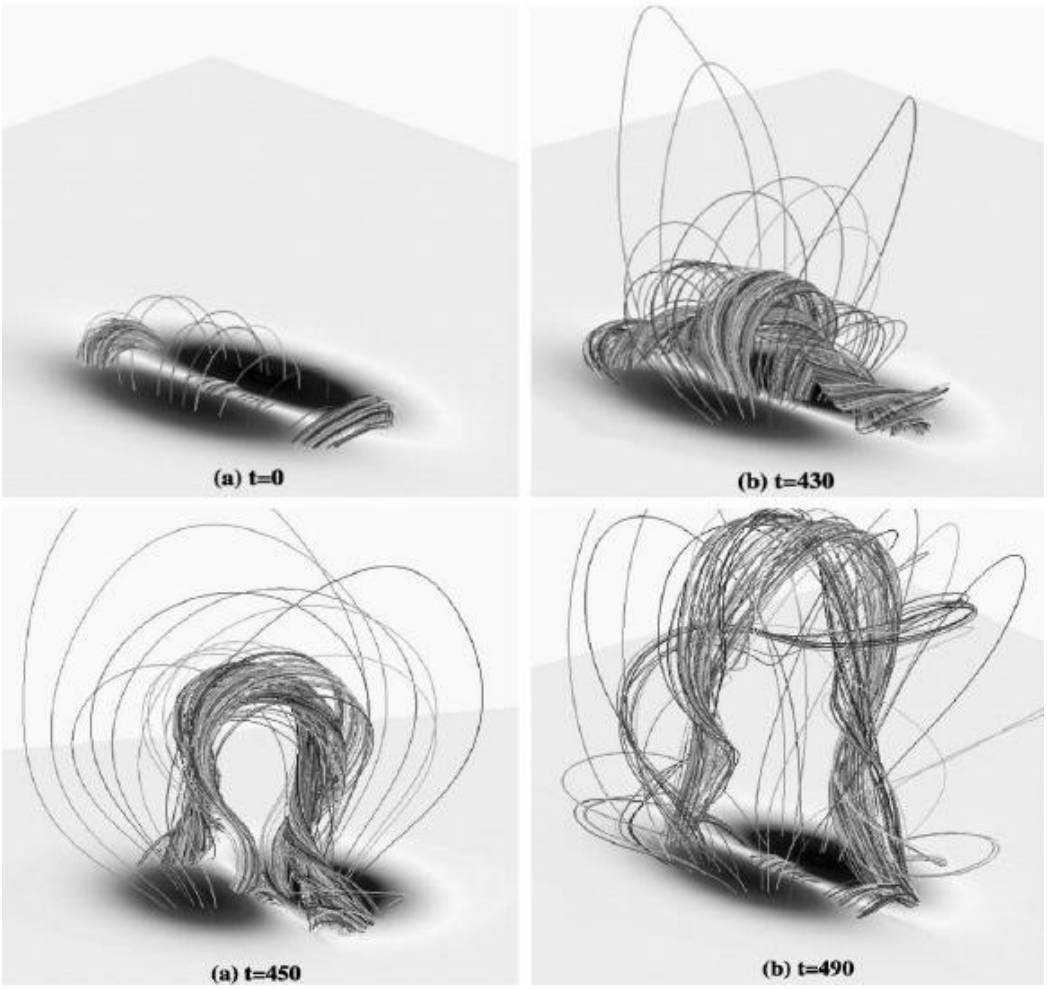

Figure 11. The evolution of the magnetic field in the 3D MHD numerical simulation of Amari et al. [2000], which shows the formation and eruption of a twisted flux rope as a simple magnetic arcade experiences shearing motions and the opposite-polarity magnetic emergence.

Another line of research considers the presence of a global instability (*catastrophe model*). A possible magnetic configuration is characterized by a twisted magnetic flux tube enclosed in an arch (Figure 12).

The photospheric motions or the weakening of the magnetic field can bring the system to a point of non-equilibrium and the flux tube rises rapidly. It then forms a current sheet in the region below and this induces a process of magnetic reconnection so that the flux tube is ejected. This evolution can take place in a bipolar magnetic configuration, but it is more likely to occur in a quadrupolar configuration.

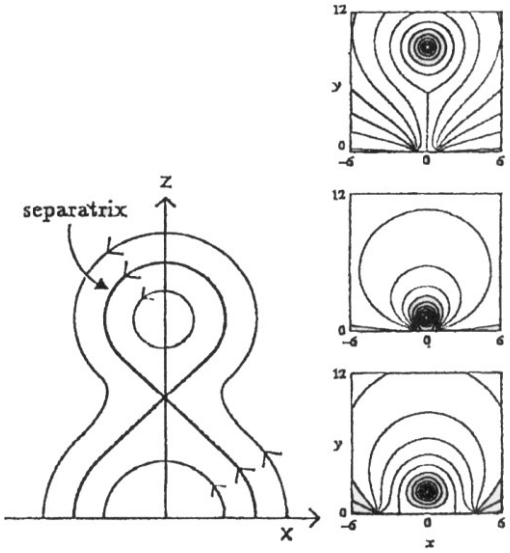

Figure 12. Catastrophe Model. Evolution of a twisted flux tube. Figure on the right, from bottom to top: the flux tube is initially in equilibrium near the photosphere; the evolution of the photospheric flow takes the system to a critical point with the formation of a current sheet below. Magnetic reconnection takes place changing the topology of the field (left), and the twisted flux tube is then expelled (adapted from Forbes and Priest, [1995]).

A different approach was adopted by Antiochos et al. [1999], that assume a topology of quadrupolar field (*break-out model*) (Figure 13).

When the lower central arch is sheared, it extends up through contact with the arch above it, forming a current sheet. It is assumed that the reconnection takes place initially with a low efficiency, the distorted arch is bounded by the highest and that the magnetic energy is progressively stored.

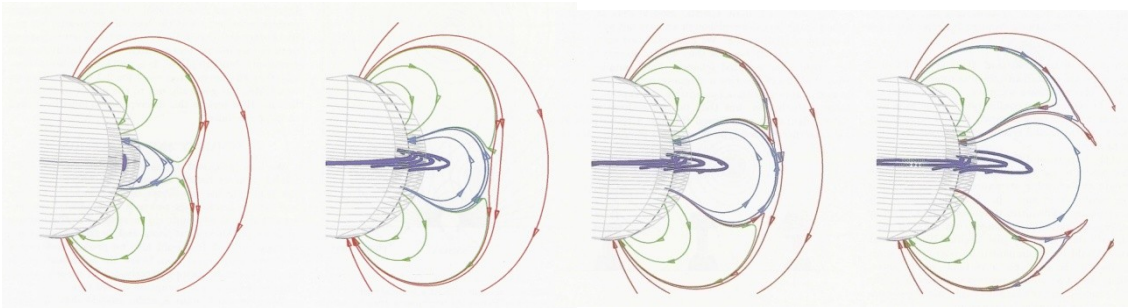

Figure 13. Break-out model. In the first figure on the left there is the potential quadrupolar configuration (the field is symmetrical about the axis of rotation and the equator). In the two following figures the system evolves due to photospheric distortion that is applied to the lower part of the central arch. Its expansion results in the formation of a current sheet.

When the efficiency of reconnection becomes significant, the confinement of the upper arcade fails, while the lower arcade spreads rapidly upwards.

The complexity of the observed CMEs requires the development of more realistic models. A plausible configuration consists of a twisted flux tube enclosed in a large quadrupolar region. This model is the combination of a catastrophe model [Forbes and Priest, 1994, Lin et al, 1998] with a break-out model [Antiochos et al, 1999], where the kinked arch is replaced by a twisted flux tube.

However, none of these models explains the wide variety of CMEs observed.

1.3 Influence of solar phenomena on Space Weather

The solar wind and the magnetic field frozen in it, produce many effects on Earth, such as, for example, variations of the geomagnetic field (geomagnetic storms), of the currents flowing in the magnetosphere-ionosphere system (geomagnetic substorms, auroras) and of the flow of high energy charged particles (in the polar regions). These effects are now framed within a context that is called *Space Weather*.

The term Space Weather has been coined to emphasize how the solar activity and the conditions of interplanetary space can have a direct impact on the terrestrial environment and also on daily life, so it is important to study and possibly forecast these conditions. The solar wind is responsible for the so-called *auroral oval*, a thin halo of permanent light of 4000 km in diameter that surrounds the Earth's magnetic poles at a height of about 110 km.

The most evident effect of geomagnetic activity is the increase of the ionospheric current system along the auroral oval which moves toward the equator. As a result, significant increases in current (sometimes even millions of Amperes) can be induced in long conductors of artificial nature, such as power, gas and oil pipelines. In the case of oil and gas pipelines, local damage may occur due to electro-corrosion. In the case of the power lines, other than the damages caused by the dissipation of energy delivered, if the induced current reaches transformers, they can also destroy them, causing major blackouts. Malfunctions due to induced currents induced by

disturbances of the ionosphere have been repeatedly found in railway signaling systems, particularly in Finland and Canada.

It should also be reminded the influence on "normal" mobile phone, without the use of satellites. Providers tend to deny firmly, but there are studies at the New Jersey Institute of Technology/Bell Labs, showing that during the strong solar activity, when there is an alignment between the Sun, distribution cell phone and mobile device (especially when the sun is low on the horizon), can occur that the solar radio emissions deceive the cell, losing the attachment to the cell in use. This phenomenon is not really dramatic for our daily activities. However it exists and probably will be more important with the development of mobile networks of third generation (UMTS).

The other serious consequence of disturbances in space weather is the chance of a damage to satellites in orbit around the Earth. In fact, it may cause faults to internal electronic components or damage of the surface of the satellite (especially critical are the photovoltaic panels that provide power). For example, broadcasting satellites, which provide connections to the telephone and television programs, depend on space weather. Other things that are harmful to the satellites are repeated passages through the Van Allen[6] radiation belts (the intensity of the radiation belt is related to space weather) and the debris left by comets and humans. High-energy particles can also endanger the health of the astronauts onboard, for example, the Space Shuttle or space station in orbit, and in case of intense events may also affect passengers on airliners flying over the polar routes.

[6] The Van Allen radiation belts are regions of high density of charged particles surrounding Earth. The belts are made of very energetic electrons and protons. The inner belt is made up of high-energy protons (10-100 MeV), while the outer belt is formed by protons and electrons of lower energy (1-10 MeV).

CHAPTER 2. *STEREO SATELLITE*

2.1 STEREO Mission

The twin NASA STEREO (Solar Terrestrial RElations Observatory) spacecraft (A and B) were launched on a single Delta rocket from Cape Canaveral on October 25, 2006. Using a lunar encounter, each spacecraft was inserted into an individual final orbit, one spacecraft (B) gradually falling behind Earth in orbit and the other (A) increasingly ahead of Earth. The two spacecrafts drift away from Earth at an average rate of about 22.5 degrees per year (Figure 14). After the two year nominal operations phase the spacecraft were about 90 degrees apart, each about 45 degrees from Earth. STEREO-A had to drift ahead of Earth and STEREO-B behind. In order to accomplish this drift, STEREO-A had to be travelling faster than Earth around the Sun and so must have had an orbit slightly closer to the Sun than Earth's. Similarly, the STEREO-B had to be travelling slower than Earth and must have had an orbit slightly further than Earth.

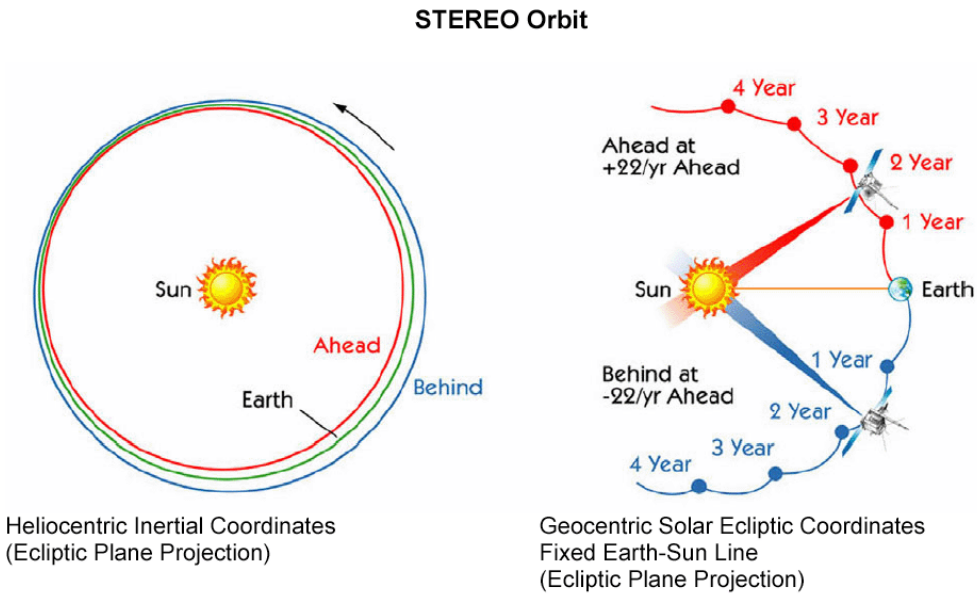

Figure 14. A sketch showing the positions of the two STEREO satellites taken during the first years.

Over time, the STEREO spacecraft continue to separate from each other at a combined rate of approximately 44 degrees per year. There are no final positions for the spacecraft. They achieved 90 degrees separation on January 24, 2009, a condition

known as *quadrature*. This is of interest because the mass ejections seen from the side on the limb by one spacecraft can potentially be observed by the in situ particle experiments of the other spacecraft.

As they passed through Earth's Lagrangian points L4 and L5, in late 2009, they searched for Lagrangian (trojan) asteroids (Figure 15). On February 6, 2011, the two spacecraft were exactly 180 degrees apart from each other, allowing the entire Sun to be seen at once for the first time (Figure 16).

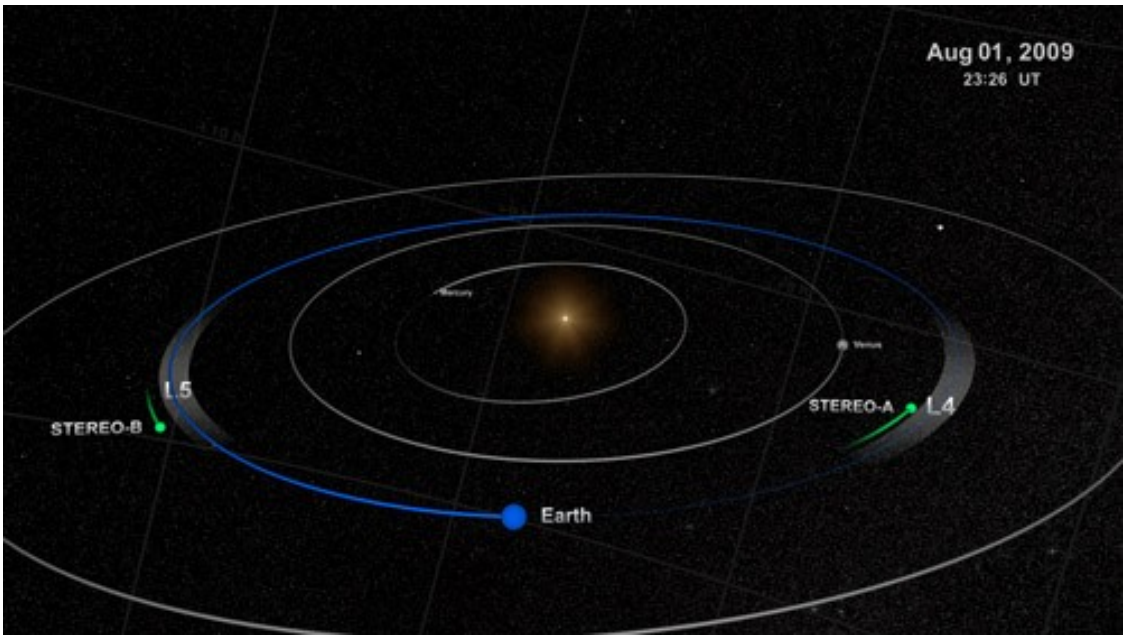

Figure 15. Image shows the position of STEREO satellites near Earth's Lagrangian points L4 and L5 in August 2009.

The STEREO mission is the third in the line of Solar-Terrestrial Probes (STP) and is a strategic element of the Sun-Earth Connections Roadmap. STEREO is designed to view the three-dimensional (3D) and temporally varying heliosphere by means of an unprecedented combination of imaging and in situ experiments mounted on virtually identical spacecraft flanking the Earth in its orbit.

The primary goal of the STEREO mission is to advance the understanding of the three-dimensional structure of the Sun's corona, especially regarding the origin of coronal mass ejections (CMEs), their evolution in the interplanetary medium, and the dynamic coupling between CMEs and the Earth environment.

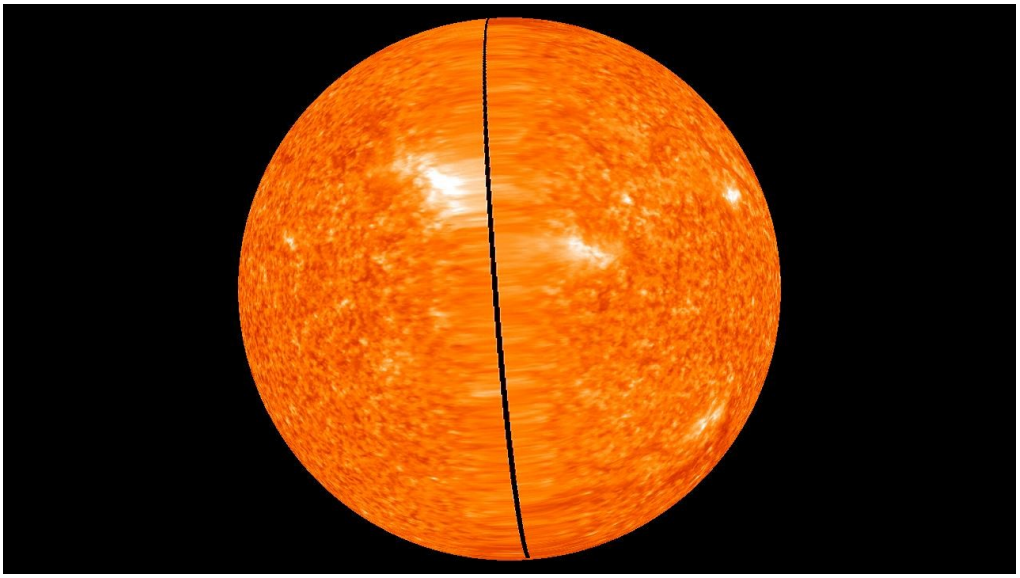

Figure 16. Image of the far side of the Sun based on high resolution STEREO data (EUVI 304 Å), taken on February 2, 2011 at 23:56 UT when there was still a small gap between the STEREO Ahead and Behind data. This gap started to close on February 6, 2011, when the spacecraft achieved 180 degree separation, and completely closed over the next several days (NASA).

We recall that CMEs are the most energetic eruptions on the Sun, are the primary cause of major geomagnetic storms, and are believed to be responsible for the largest solar energetic particle events.

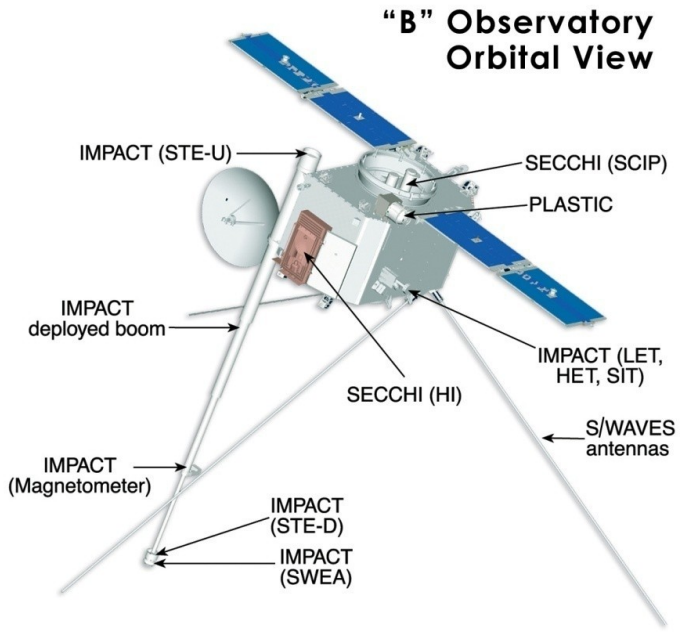

Figure 17. The STEREO suite and packages onboard satellites.

The STEREO suite has three main parts (Figure17): the SCIP (Sun Centered Imaging Package - three telescopes), the HI (Heliospheric Imager - two telescopes) and the SEB (Secchi Electronics box) [Howard et al., 2008].

Each of the spacecraft carries cameras, particle experiments and radio detectors in four instrument packages:

- Sun Earth Connection Coronal and Heliospheric Investigation (SECCHI) has five cameras (Figure 18): an extreme ultraviolet imager (EUVI) and two white-light coronagraphs (COR1 and COR2). These three telescopes are collectively known as the Sun Centered Instrument Package or SCIP, and image the solar disk and the inner and outer corona. Two additional telescopes, heliospheric imagers (called the HI1 and HI2) image the space between Sun and Earth. The purpose of SECCHI is to study the 3-D evolution of Coronal Mass Ejections through their full journey from the Sun's surface through the corona and interplanetary medium to their impact at Earth (Figure 19).
- In-situ Measurements of Particles and CME Transients (IMPACT) can study energetic particles, the three-dimensional distribution of solar wind electrons and interplanetary magnetic field.
- PLAsma and SupraThermal Ion Composition (PLASTIC) can study the plasma characteristics of protons, alpha particles and heavy ions.
- STEREO/WAVES (SWAVES) is a radio burst tracker that can study radio disturbances traveling from the Sun to the orbit of Earth.

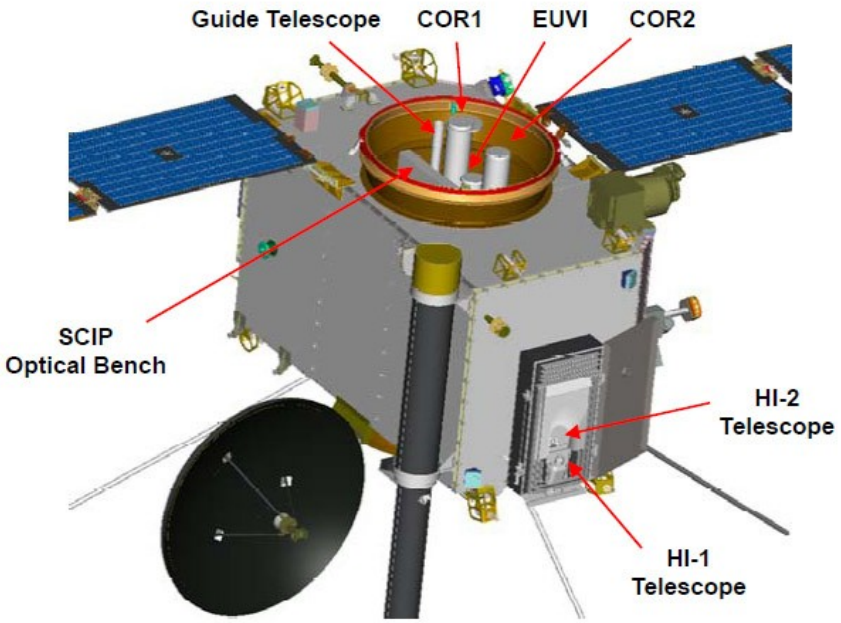

Figure 18. A close-up of the spacecraft body showing the EUVI, COR1-2 and HI telescopes, together with the SECCHI Sun Centered Instrument Package (SCIP). (Adapted from diagrams by the Johns Hopkins University Applied Physics Laboratory).

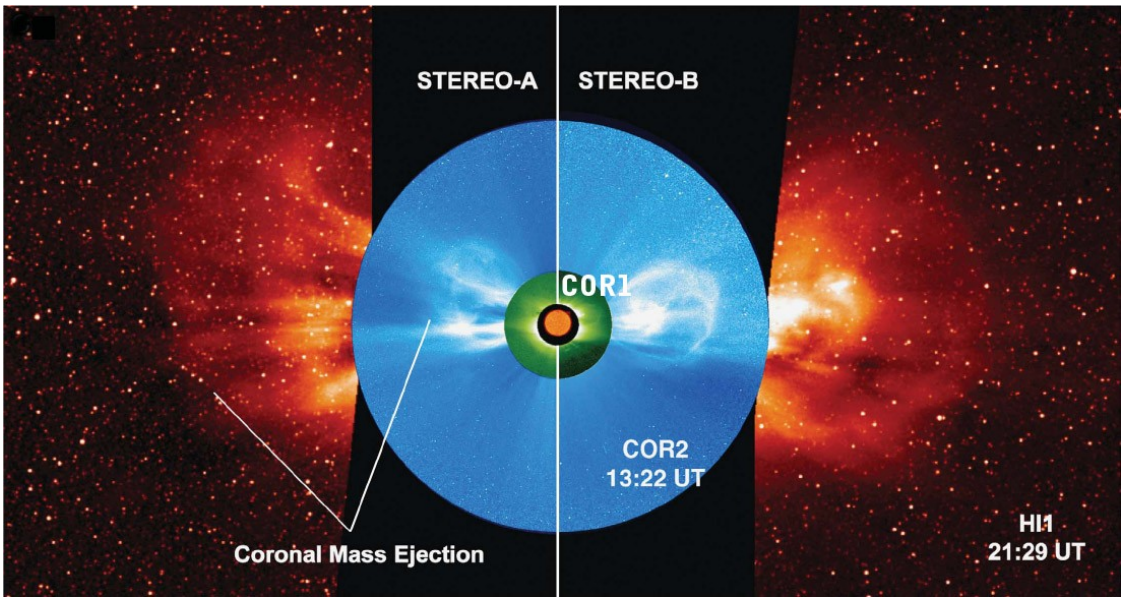

Figure 19. Composite of STEREO-A and B images from the SECCHI instruments of the CME of 12 December 2008. Image shows that the CME is Earth-directed, being observed off the east limb in STEREO-A and off the west limb in STEREO-B (adapted from Byrne et al., 2010).

2.2 SECCHI Instrument

SECCHI is named after one of the italian astronomer: Angelo Pietro Secchi (1818-1878), a Jesuit priest. He was one of the first astrophysicists to use the new medium of photography to record solar eclipses. He photographed the 1860 eclipse, during which a CME is now thought to have occurred (see Figure 20).

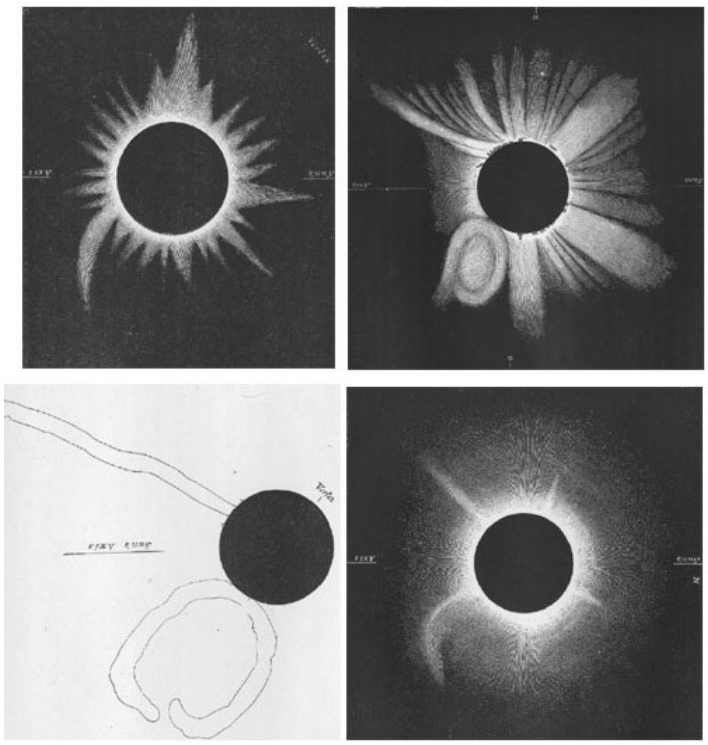

Figure 20. Eclipse drawings showing a possible CME (Angelo Secchi, 1860).

SECCHI is a suite of 5 scientific telescopes that observe the solar corona and inner heliosphere from the surface of the Sun to the orbit of Earth.

The EUVI telescope was developed at LMSAL (Lockheed Martin Solar and Astrophysics Laboratory). The EUVI observes the chromosphere and low corona in four different EUV emission lines between 17.1 and 30.4 nm. It is a small, normal-incidence telescope (Ritchey-Chrétien system) with thin metal filters, multilayer coated mirrors, and a back-thinned CCD detector. The Extreme Ultra-Violet Imager obtains full disk solar images in four EUV wavelengths (17.1, 19.5, 28.4, 30.4 nm)

(Figure 21), producing images with a cadence as fast as 2.5 minutes in the most common wavelengths.

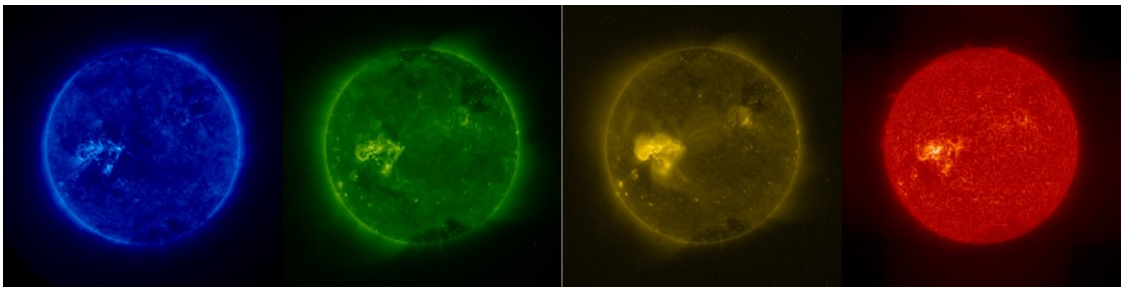

Figure 21. Views of the Sun from STEREO/EUVI in the four wavelengths (17.1, 19.5, 28.4, 30.4 nm, respectively from left to right) (NASA/STEREO).

Heliospheric Imagers (HIs) consists of two small, wide-angle telescope systems mounted on the side of each STEREO spacecraft, which view space, sheltered from the glare of the Sun by a series of linear occulters. The HI instrument concept was derived from the laboratory measurements of Buffington et al. (1996) who determined the scattering rejection as functions of the number of occulters and the angle below the occulting edge. The result of their analysis showed that a simple telescope in a small package could achieve the required levels of rejection by proper occulting and by putting the telescope aperture sufficiently in the shadow of the occulter. The concept is not unlike observing the night sky after the Sun has gone below the horizon.

Each HI instrument comprises two refractive telescopes, known as HI-1 and HI-2 (Figure 22). Using the labels A and B for the Ahead and Behind spacecraft, respectively, we have four telescopes, which we denote HI-1A, HI-2A, HI-1B, and HI-2B. Both HI-1 telescopes are identical and both HI-2 telescopes are identical. HIs view the inner heliosphere starting at an elongation of 4° from the Sun. HI-1 has a field of view (FoV) of 20°, from 4–24° elongation (~12–85 $R_{\odot}$), and HI-2 of 70°, from ~19–89° elongation (~68–216 $R_{\odot}$). There is a 5.3° overlap between the outer HI-1 and inner HI-2 FoVs.

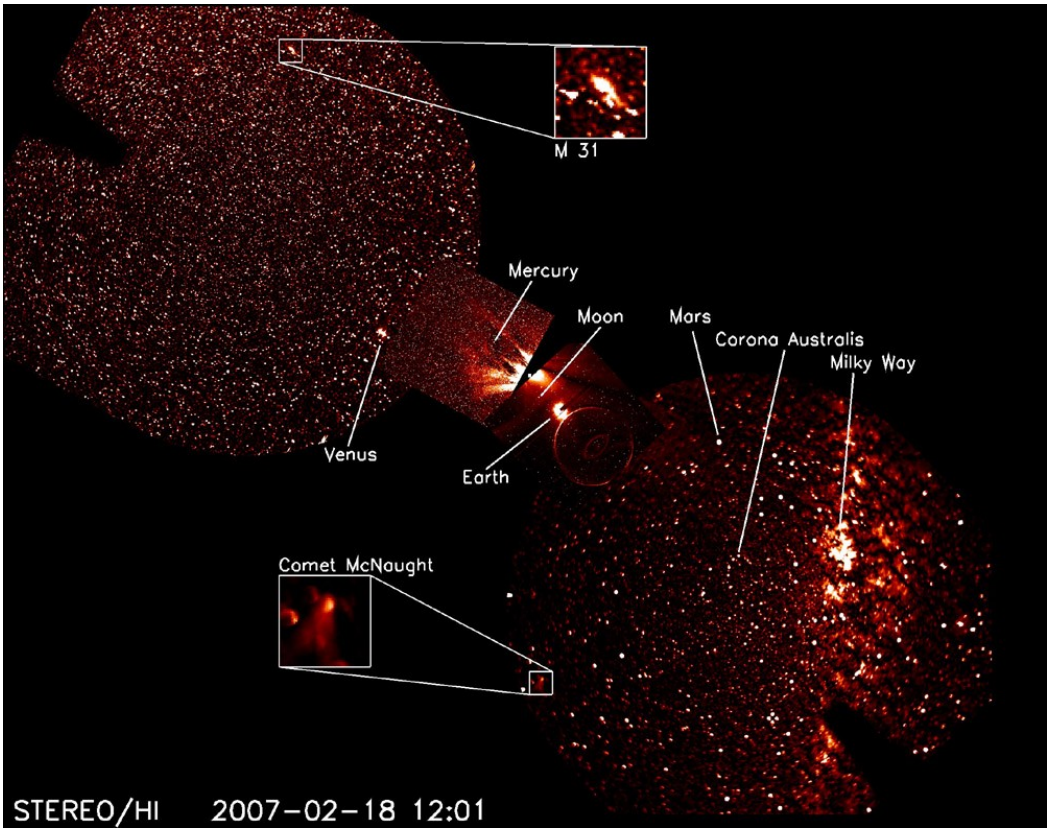

Figure 22. A composite of all HI images taken on 18 February 2007. The Sun is shown approximately to scale, between the HI-1 frames, and a number of planetary and astronomical sources are identified. This composite image necessarily compromises the display of the true image resolutions but does stress the heliospheric coverage (from Harrison et al., 2008).

2.3 COR1 and COR2

In this thesis we use data from the two inner coronographs, COR1 and COR2. The COR1 telescope on STEREO is based on the classic design by Bernard Lyot, adapted for spaceflight by engineers at NASA Goddard Space Flight Center and Swales Aerospace. COR1 is an internally-occulted coronagraph of length ~1.2 m and is one of the STEREO SECCHI suite of remote sensing telescopes.

COR1 has a FoV of 1.4 – 4.0 $R_{\odot}$ and typical cadence of 8 minutes [Thompson et al., 2003]. The coronagraph includes a linear polarizer, which is used to suppress scattered light and to extract the polarized brightness signal from the solar corona. The detector is an EEV model 42-40 CCD, with 2048 × 2048 pixels, 13.5 μm on a side. The nominal spatial resolution is 7.5 arcsec (pixel size of 3.75 arcsec).

Typically, the COR1 images are 2×2 binned onboard before telemetering to the ground (Figure 23). The polarized brightness is extracted from three sequential images taken with polarizations of 0°, 120°, and 240°. The cadence of a sequence is every 5 or 10 minutes. A monthly background is subtracted from each polarization component to remove the scattered light and the F-corona. These background images are available at the STEREO COR1 web site.

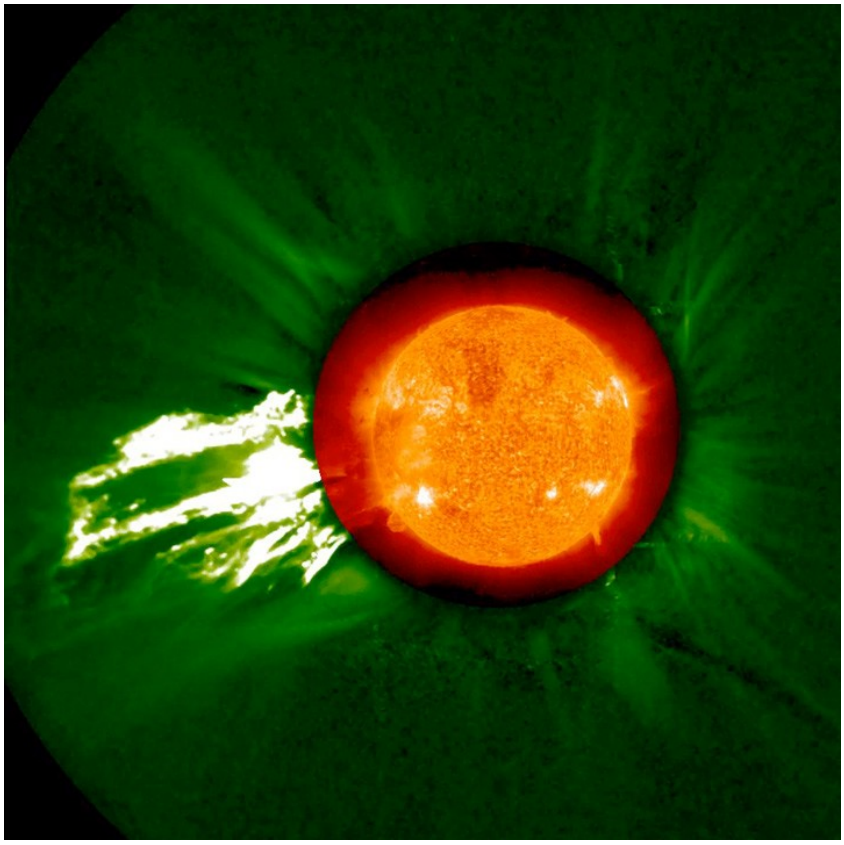

Figure 23. COR1 example image. The Sun unleashed an M2 (medium-sized) solar flare with a substantial coronal mass ejection (June 7, 2011) that is visually spectacular. The large cloud of plasma mushroomed up, and while some parts of this fell back into the Sun, most rushed off into space. When viewed in the STEREO (Ahead) coronagraphs, the event shows a very bright plasma cloud roaring from the Sun. This COR1 image shows the cloud in mid-flight by combining images taken at the same time: the orange is the Sun itself (in extreme UV light) with the green COR1 coronagraph (NASA/STEREO).

The SECCHI outer coronagraph, known as COR2, is an externally occulted Lyot coronagraph. COR2 has a FoV of 2.5 – 15 $R_{\odot}$ and cadence of 15 minutes (Figure 24). COR2 derives its heritage from the highly successful LASCO C2 and C3 coronagraphs

aboard SOHO [Brueckner et al., 1996]. It was designed and built by the Naval Research Laboratory. In comparison to LASCO, several design challenges were associated with COR2. The instrument was to have approximately the same field of view as LASCO C2 and C3 combined[7], a spatial resolution comparable to C2, a much shorter exposure time than either C2 or C3 while accommodating a greater bore sight offset from sun center and fitting into a smaller envelope.

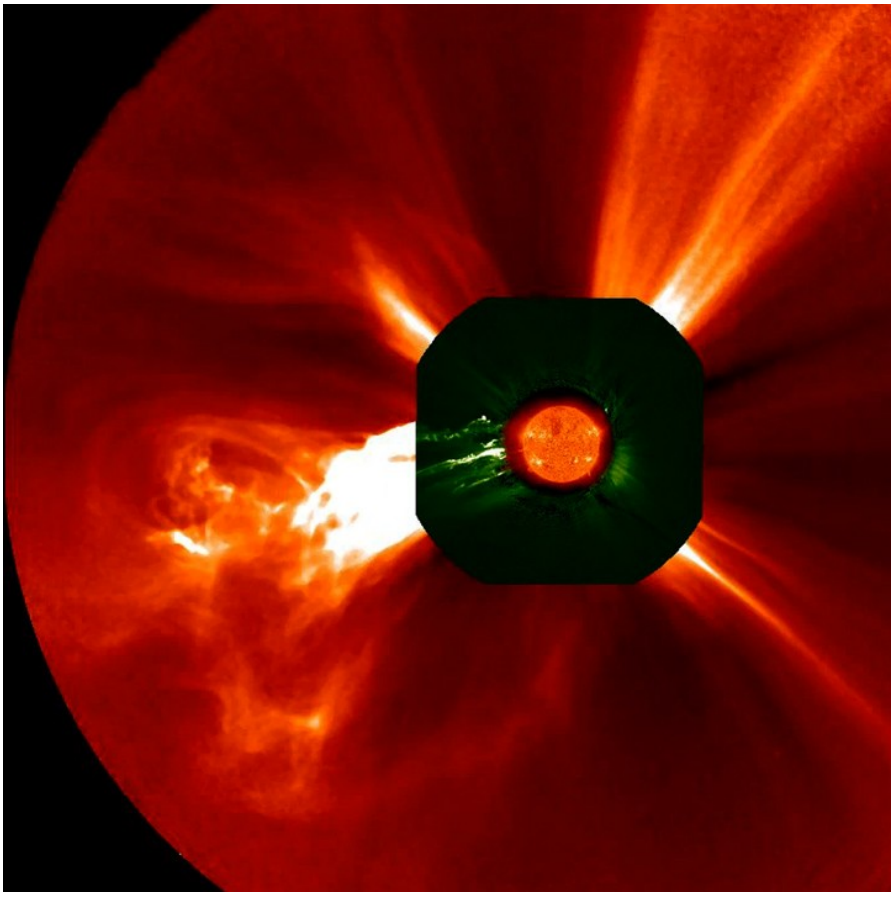

Figure 24. COR2 example image. This COR2 image shows the cloud in mid-flight by combining images taken at the same time: the orange is the Sun itself (in extreme UV light) with the green COR1 and reddish COR2 coronagraph (NASA/STEREO).

SECCHI coronagraphs mask the solar disk, whose brightness is more than 10^5 that of the corona. The coronagraph measures the total brightness or polarization brightness integrated over the line of sight through the optically thin corona.

[7] LASCO C2 has a FoV of 1.5-6 $R_\odot$ and a cadence of 30 min while C3 has a FoV of 3.7-30 $R_\odot$ and a cadence of 50 min.

CHAPTER 3. *STEREO TECHNIQUE*

3.1 Stereoscopy

For my project of research it is very important to know the geometry of the solar coronal features, and to take into account that we introduce some basic stereoscopy principles (see Inhester, 2006).

The determination of the distance of nearby stars by measuring the parallax angle was one of the first applications of stereoscopy in space and astrophysics. The fundamental principles relating to stereoscopic are very simple, in fact once an object is detected and identified in two images from different observative points, the reconstruction is a purely linear geometrical task. It is precisely our case, in fact with STEREO data, images come from two vantage points.

The classical stereoscopy problem is the reconstruction of surfaces from a pair of images and the first step is the identification and matching of the objects to be reconstructed in the stereo images.

If the reconstruction concerns simple geometrical objects composed of piecewise planes connected by straight edges, it can be achieved if the only edges can be identified in the images. Usually the edges are detected as sharp boundaries in brightness, color or texture, so that they are reconstructed first.

As stressed by Inhester [2006], when we have identified an object, the reconstruction task, i.e., the calculation of its depth, depends on the extent or dimension of the object:

• point-like object (Figure 25a): we extract 2×2 image coordinates from the image pair, from which we can determine the 3-space coordinates of the object using a linear relationship;

• curve-like object (Figure 25b): we extract two curves from the image pair, each of which could be considered the “head-on” image of a projection surface extending in each field of view direction. The intersection of the two projection surfaces yields (in the ideal case) a unique 3-dimensional curve;

• surface-like object (Figure 25c): we can extract its visible edges from the image pair, but the respective projection surfaces refer to different locations on the surface to be reconstructed. This problem is underdetermined and without further information (for instance, the assumption of a surface curvature, the knowledge about the location of a light source, the surface reflectivity together with precise intensity measurements) a reconstruction is impossible.

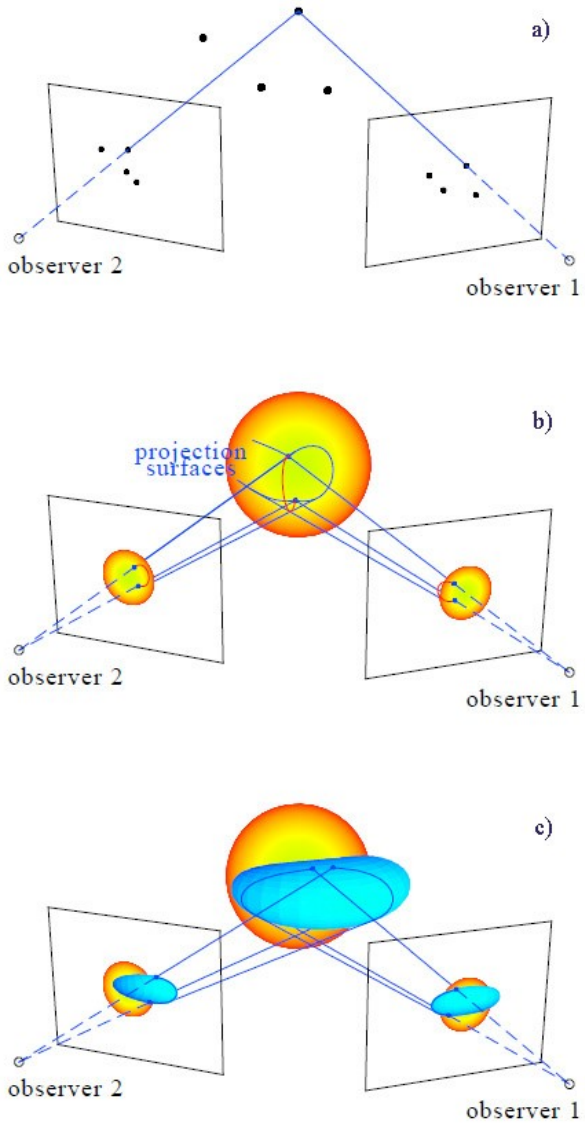

Figure 25. Back projection to reconstruct point-like, curve-like and surface-like objects to illustrate the different conditions of solvability (adapted from Inhester, 2006).

For this reason in classical stereoscopy the edges, being curve-like objects, are reconstructed first.

In the next sections (3.2, 3.3 and 3.4) we describe the geometry relevant to stereoscopic observations (epipolar geometry) and the reconstruction's techniques (TP and LCT).

3.2 Epipolar Geometry

We have to find a suitable coordinate system so that the reconstruction can be reduced from a 3-dimensional to a set of 2-dimensional planar problems. For stereoscopy the geometrical conditions are such that two view points and two view directions are involved.

The line connecting the two view points is called the *stereo base line*, and subtends the stereo base angle between the two main view directions or optical axes of the respective telescopes (note that the two optical axes do not need to intersect). Let us take into account that the two observer positions and any object point to be reconstructed exactly define a plane. For many object points there will be many planes, but each of them will contain the two observer positions and is called *epipolar plane* (see Figure 26).

The projection of epipolar planes on both observer's images are lines (see Figure 26) and since any observer is on any epipolar plane, he sees them "head on". These lines, called *epipolar line*s, generate a coordinate system on the image planes.

Moreover, depending on his field of view observer 1 may see observer 2 (and vice-versa), and since observer 2 is defined to lie on all epipolar planes, all epipolar lines in image 1 must converge in the projection of observer 2, called the *epipole* of the respective projection [Inhester, 2006].

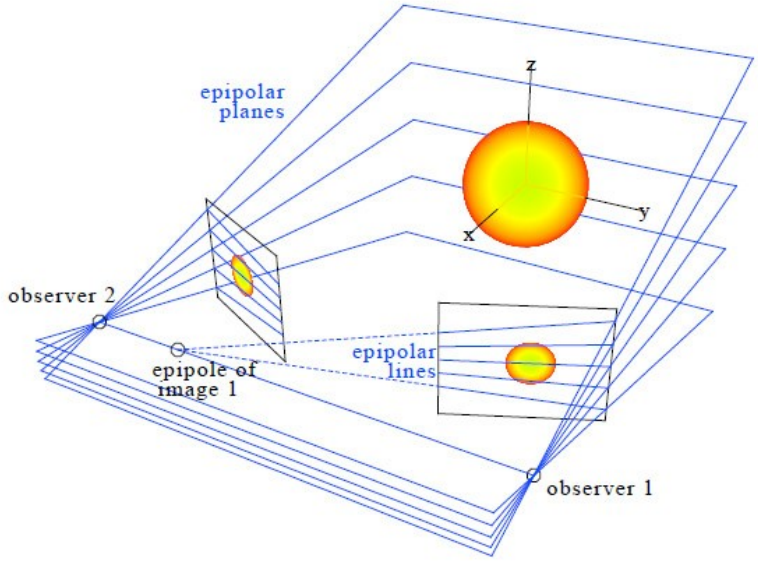

Figure 26. Orientation of epipolar planes in space and the respective epipolar lines in the images for two observers looking at the Sun. The observers telescope screens are derived from a projective geometry camera model (from Inhester, 2006).

Because the epipolar lines in one image depend on the position of both observers, any change in position of observer 2 requires a redetermination of epipolar lines also in image 1. The epipolar lines may be identified by the angle they form with a reference epipolar plane or by the coordinate of the plane's intersection with a suitable axis of a (completely independent) coordinate system, e.g., the z-axis in Figure 26.

In the STEREO context, the axis is the rotation axis of the Sun because, since the spacecraft are more or less close to the ecliptic, the Sun's rotation axis should intersect all relevant epipolar planes. With this choice, an epipolar plane is uniquely defined by the two observer's positions and its intersection point with the rotation axis.

Most space points lie on a unique epipolar plane, with the only exception of the points on the stereo base line. If these points are ruled out, any point which is identified on a certain epipolar line in one image must lie on the same epipolar line in the other image (epipolar constraint).

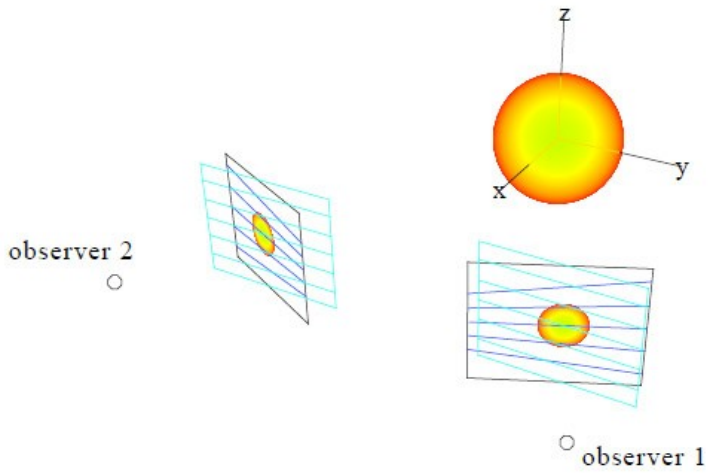

Figure 27. Virtual change of orientation of the observer's main view direction equivalent to rectification. The rectified configuration is indicated by the rotated screens drawn in light blue (from Inhester, 2006).

We can therefore directly overplot the epipolar lines and their labels onto each image and thus determine the epipolar plane of an object from the image. As a consequence, we must only calculate the object's two-dimensional coordinates on the known epipolar plane, achievable from the measure of the positions of the object's projection along the epipolar line in either image.

The depth of an object results to be proportional to the difference of these coordinate values along the epipolar line of the two projections, the *disparity*. From the geometrical construction it results that epipolar lines usually are not parallel.

For an easy reconstruction it would be desirable to have the epipolar lines mapped into horizontal lines, this corresponding to the case when both spacecrafts have their optical axes directed parallel to each other (see Figure 27).

3.3 Tie-Point Reconstruction

As described above, we can reduce the reconstruction problem to a set of 2-dimensional problems. We segment each image densely into a (large) number of epipolar lines and compare the positions of a loop's intersections along the respective epipolar line in each image. In the following we report the main concepts described in

Inhester [2006], showing how we can derive from these positions the intersection of the loop on the respective epipolar planes.

Let on a given epipolar plane the observer's positions be $\mathbf{r}_1$ and $\mathbf{r}_2$. For each epipolar plane we in addition specify a reference point $\mathbf{r}_0$ as the origin of the 2-dimensional coordinate system on this plane. For convenience, we take the intersection of the solar rotation axis with the epipolar plane the intercept of which could at the same time serve as a continuous label for the epipolar plane. For each observer we then introduce orthogonal coordinate axes $\mathbf{v}_i$ and $\mathbf{e}_i$ on the epipolar plane as shown in Figure 28: $\mathbf{v}_i$ is the unit vector from the observer to $\mathbf{r}_0$ and $\mathbf{e}_i$ is $\mathbf{v}_i$ rotated clockwise by 90 degrees. Note that $\mathbf{v}_i$ does not need to agree with the optical axis of the telescope nor must $\mathbf{e}_i$ have the direction of the epipolar line.

We will take as rectified image coordinate along the respective epipolar line in image i the angle s_i between the direction to the object and $\mathbf{v}_i$. For convenience, we assume that the mapping of the observing telescopes can be described by a simple projective geometry camera model.

In this case, an object at an angular distance σ from the optical axis is mapped in the image to a distance $\rho = f \tan \sigma$, where f is the camera's focal length.

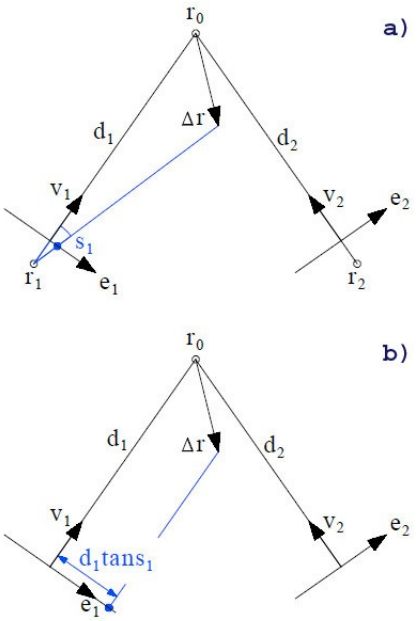

Figure 28. Reconstruction of a point Δr with projective (top) and affine (bottom) geometry (adapted from Inhester, 2006).

In this case, the angle s_i can be derived from the image distances ρ_0 and ρ of the reference and object point's projection from the image centre, respectively, and their azimuth difference γ (see Figure 29) by:

$$\cos s_i = \frac{f^2 + \rho_0 \rho \cos\gamma}{\sqrt{f^2 + \rho_0^2}\sqrt{f^2 + \rho^2}} \tag{1}$$

Here, the sign of s_i depends on whether the object is projected to the right (+) or left (-) of the line from the image centre to $\mathbf{r}_0$'s projection. If there is any image distortion, the distances ρ_0 and ρ read from the image have to be corrected accordingly.

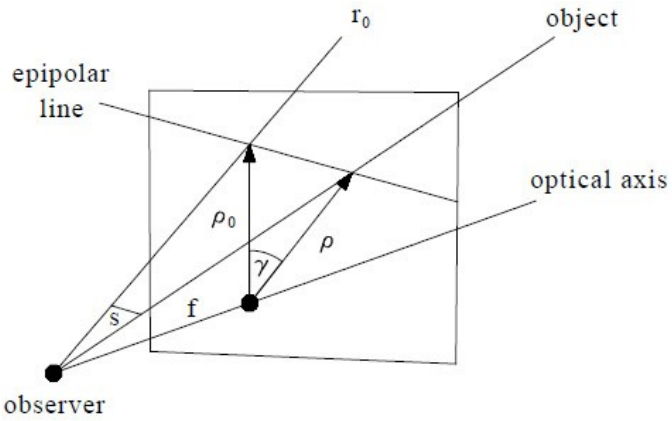

Figure 29. Derivation of the angle s from the image coordinates for a projective geometry camera model (from Inhester, 2006).

Formula (1) is numerically inconvenient for large focal lengths f and small image distances ρ. For ρ/f, $\rho_0/f \rightarrow 0$ relation (1) can be approximated by:

$$s_i^2 = (\frac{\rho_0}{f})^2 + (\frac{\rho}{f})^2 - 2\frac{\rho_0 \rho}{f^2}\cos\gamma + \mathcal{O}((\frac{\rho}{f})^4) \tag{2}$$

which is the law of cosines applied to the triangle in the image plane in Figure 29. Hence, the angle s can in this limit be read directly from the image in units of arcsecs. The necessary camera calibration information is then contained in the position of the

observers $\mathbf{r}_i$ and either the reference point $\mathbf{r}_0$ or the two view directions $\mathbf{v}_i$ to the reference point. In the latter case, $\mathbf{r}_0$ can be determined from (see Figure 28a):

$$r_0 = r_1 + d_1 v_1 = r_2 + d_2 v_2 \tag{3}$$

$$(v_1, v_2) \begin{pmatrix} d_1 \\ -d_2 \end{pmatrix} = r_2 - r_1 \tag{4}$$

Therefore a rectified image point (s_1, s_2) = (0,0) will have to be reconstructed at $\mathbf{r}_0$ and any other (s_1, s_2) pair will be conveniently expressed as a 2-dimensional distance vector $\Delta\mathbf{r}$ from $\mathbf{r}_0$.

For affine geometry, all view directions from an image *i* are approximated to be parallel to $\mathbf{v}_i$. Then (see Figure 28b):

$$\begin{pmatrix} e_1^T \\ e_2^T \end{pmatrix} \Delta r = \begin{pmatrix} d_1 \tan s_1 \\ d_2 \tan s_2 \end{pmatrix} \tag{5}$$

If we subtract the two above lines we obtain the "depth" component of Δr in direction half way between the two view directions. Note, with beta the angle between $\mathbf{v}_1$ and $\mathbf{v}_2$ we have $\mathbf{v}_1 + \mathbf{v}_2 = (\mathbf{e}_2 - \mathbf{e}_1)/\tan(\beta/2)$. Then:

$$\tan\frac{\beta}{2}\,(v_1^T + v_2^T)\Delta r = d_1 \tan s_1 - d_2 \tan s_2 \tag{6}$$

where the difference on the right hand side is the disparity. In the simplest case, the depth of an object is directly proportional to the disparity of its projections along the epipolar lines.

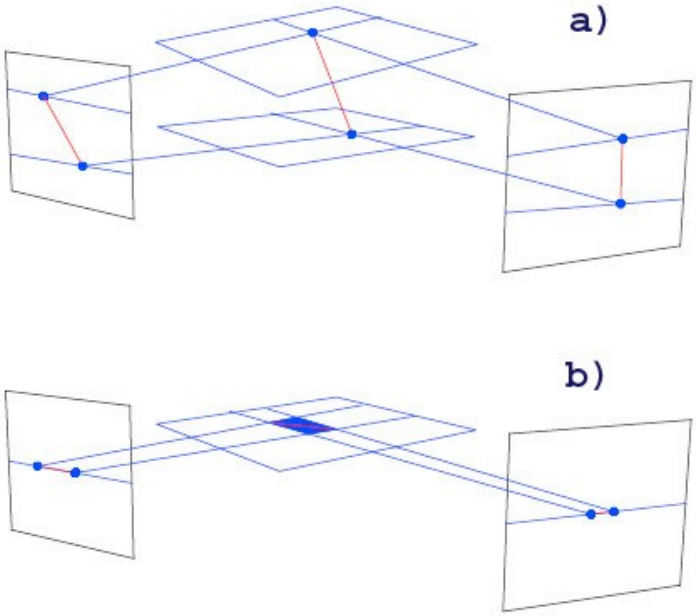

Figure 30. Reconstruction of a curve segment (red) with different inclination with respect to the adjacent epipolar planes (blue). In the top drawing the line segment in inclined to, in the bottom drawing it lies exactly on an epipolar plane (adapted from Inhester, 2006).

For projective geometry we take account of the divergence of the view directions emerging from each observer. The angle s_i between the reference point $\mathbf{r}_0$ and an object in the epipolar plane then is (see Figure 28a):

$$\tan s_i = \frac{e_i^T \Delta r}{d_i + v_i^T \Delta r}$$

or

$$\begin{pmatrix} e_1^T - v_1^T \tan s_1 \\ e_2^T - v_2^T \tan s_2 \end{pmatrix} \Delta r = \begin{pmatrix} d_1 \tan s_1 \\ d_2 \tan s_2 \end{pmatrix} \tag{7}$$

in contrast to (5). To justify the more simple affine geometry formula, s_1 and s_2 must both be small.

For EUVI images, s is of the order of the apparent solar disk radius of about 0.005 radian. For HI images, however, with a much larger field of view, projective geometry is unavoidable. Even if s is small some care is necessary, because in (5), the matrix on the left has to be inverted and small changes in its parameters may alter its minor

eigenvalue considerably. The eigenvalue of a matrix (**a**, **b**) is $O(|\mathbf{a} \times \mathbf{b}|)$ if it is small compared to |**a**| and |**b**|. Hence if the view directions are nearly parallel, the difference between affine and projective geometry may be non-negligible even if *s* is small.

For each epipolar plane we obtain a set of intersection points and all we have to do is to connect the intersection points between neighbouring planes to obtain 3-dimensional curves. This last step involves some uncertainties if different loops come close. To obey the disparity continuity constraint we should keep track of the intersections across the epipolar planes by reconstructing curve segments between epipolar lines rather than only points on single epipolar lines (practically, we just combine the intersection points of a given curve projection with epipolar lines to ordered lists). Hence the method should better be called tie-curve rather than tie-point method.

The curve segments from each image are then projected along their respective geometrical view direction (either affine or projective) which yields a narrow planar strip of the projection surface of the curve (see Figure 30a). The intersection of the strips from both images gives a small line segment of finite length, the end points of which are two points of the three-dimensional loop curve. The intersection is guaranteed since the curve sections in the image were chosen from the same epipolar interval.

This strategy runs into a problem, however, if the curve segment is directed parallel to an epipolar line (see Figure 30b). The geometrical intersection of the two projection ribbons now is not a line segment anymore but a small trapezoid. This object of dimension 2 is difficult to incorporate to our final 3D loop curve of dimension 1. This problem, however, is not a deficit of the method but a fundamental geometrical limitation.

3.4 Local Correlation Tracking (LCT)

Another technique utilized in stereoscopy is the *local correlation tracking* [Mierla et al, 2009].

To find the correspondence between the images, i.e., to identify the same pixels appearing in both images, is one of the key problems of stereoscopic reconstructions. Unfortunately, CMEs often have a rather diffuse density distribution where prominent, well-located points are difficult to identify. Instead of using a feature-based correspondence, we should use a correlation-based approach (see, e.g., Trucco and Verri, 1998). In such a correlation-based method the elements to be matched are small sub-images of fixed size, called "match windows". The criterion which decides whether two such windows in each image are positioned on the same object is their mutual correlation coefficient.

In order to find correlations, we keep the match window in a fixed position on a given epipolar line in one image and move it along the same epipolar line in the other image. If a maximum of the correlation occurs at a certain shift, the center position of the windows is used for tie-pointing the 3D region which has probably produced this high correlation. This procedure is subject to some constraints in order to catch meaningful correlations and discard improbable ones. First we use normalized cross-correlations on the match windows *W*:

$$\sigma_{AB}(x, x', y) = \frac{\int_W I_A(x+\xi, y+\zeta) I_B(x'+\xi, y+\zeta)\, d\xi\, d\zeta}{\left(\int_W I_A^2(x+\xi, y+\zeta)\, d\xi\, d\zeta \int_W I_B^2(x'+\xi, y+\zeta)\, d\xi\, d\zeta\right)^{1/2}} \quad (8)$$

with $\sigma_{AB} \in [-1, 1]$; where $I_A(x, y)$ and $I_B(x, y)$ are the respective intensities after rectification at positions given by the epipolar line coordinate y and the horizontal coordinate x. The integrals are done over the whole pixels in the window *W* (ξ and ζ). This choice is sensitive also to correlations at low intensity levels. In order to discard spurious correlations, we limit the maximum disparity |x – x'|. Since the disparity for a given spacecraft configuration is directly proportional to the reconstructed depth, this limitation is equivalent to restricting the reconstructed CME to a certain depth range. The depth is defined as the distance of a feature from the plane of the sky. The shift limits are set so that a depth range of $\pm 5 R_\odot$ (corresponding to COR1 data) and $\pm 12 R_\odot$ (corresponding to COR2 data) resulted. Finally, only maxima of $\sigma_{AB}(x, x', y) > 0.9$ are considered for the tie-point reconstruction.

For this method we use the total brightness (tB) images because the tB scattering cross section is isotropic within a factor of two. The decrease of the scattering function away from the plane of the sky is essentially due to the $1/r^2$ decrease of the primary solar radiation. Note that the normalization in correlation (8) takes care of a possibly different signal intensity of a given structure in the two images.

3.5 Coordinate System and Display of 3D Features

All our reconstructions of halo CMEs shall be displayed in the same coordinate system for easy comparison. We choose the Heliocentric Earth Equatorial (HEEQ) coordinate system for this purpose [Hapgood 1992]. It has its origin at the Sun's center, the Z is the solar rotation axis, X is in the plane containing the Z-axis and Earth, at the intersection of the solar central meridian and the heliographic equator, and Y completes the right-handed coordinate system.

We also use Stonyhurst heliographic coordinates (Figure 31) which are closely related to HEEQ coordinates [Thompson, 2006].

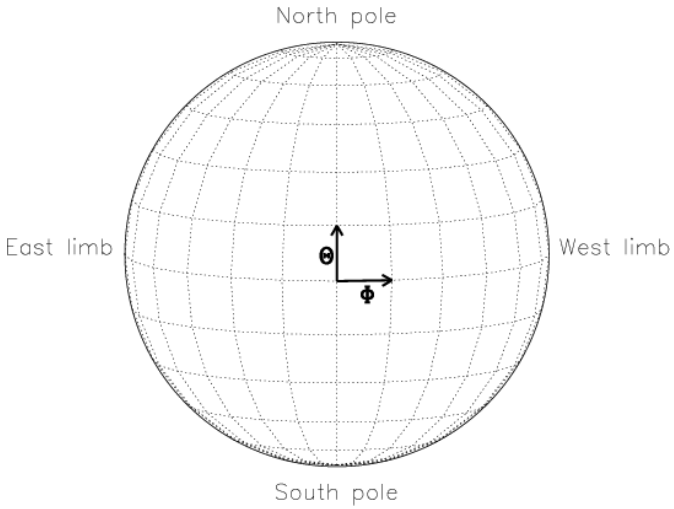

Figure 31. A diagram of the Sun, showing lines of constant Stonyhurst heliographic longitude (Φ) and latitude (Θ) on the solar disk. The origin of the coordinate system is at the intersection of the solar equator and the (terrestrial) observer's central meridian. This representation is also known as a *Stonyhurst grid* (from Thompson, 2006).

The coordinates are represented in the spherical coordinate system as latitude, longitude, and distance from the Sun's center. The value of the longitude ranges between −180° and +180°. This also means that the front side disk longitude ranges between −90° and +90°. The image coordinates are given by the X-axis and the Y-axis.

In order to display the reconstructed points, we use the following procedure. The resulting 3D positions are displayed as isodensity surfaces. In a given geometry, the space around the Sun is divided into a rectangular grid, and the density is calculated for each cell (voxel[8]). The resolution of the reconstruction depends of the cell size (for our data we use a cube of 256×256×256 cells).

In what follows, we apply the mentioned techniques to the SECCHI-COR data, in order to reconstruct the CMEs and/or their directions of propagation. We make use of the local correlation tracking (LCT) to identify the same feature in COR Ahead and COR Behind images. Then, using tie-point (TP) reconstruction method we infer the 3D structure of CMEs. We refer to this as the LCT-TP reconstruction technique. These techniques are applied on three structured CMEs[9] observed by COR1 and COR2 instruments on 3 April 2010, 7 August 2010 and 15 February 2011 (see Section 4).

The objects we deal with here are localized blobs of plasma that we can discriminate in a CME cloud. The selection of the features to be tracked is based on the fact that they were easily and unambiguously identifiable by naked eye in both A and B images. Because these features are part of the global CMEs, their selection will not affect our results regarding the determination of the direction of propagation of the CME. The blobs are often still diffuse and cannot be localized to high precision compared to, for example, loops in EUV images. For this reason, we argue that it is justified to relax the reconstruction constraints slightly.

For this study we assume that a) the two spacecrafts are in the ecliptic plane (i.e., the STEREO mission plane and the ecliptic are approximately the same) and b) we can

[8] A voxel (*volumetric pixel* or *Volumetric Picture Element*) is a volume element, representing a value on a regular grid in three dimensional space. This is analogous to a pixel, which represents 2D image data in a bitmap.

[9] By *structured CME* we mean the classical 'three-part' CMEs, consisting of a bright, circular front, followed by a dark cavity and a bright compact core.

use affine geometry[10] for the reconstruction instead of projective geometry. As a consequence, we can treat epipolar planes in each image as being parallel to the ecliptic.

The geometric localization tool consists of IDL (Interactive Data Language) programs that can process SECCHI COR images. Based on the time period of interest provided by the user, the programs retrieves, processes, and displays a pair of concurrent coronagraph images taken by SECCHI-A and SECCHI-B.

The images of the CMEs events are stored on the computer in the fits (Flexible Image Transport System) file format. Then manually we selected the CME'edge from each image. User intervention is necessary at this point because of the difficulty in automatically identifying the faint boundary of the CME as a whole, instead of the sharper edges associated with bright coronal features, such as, for example, streamer belts or structures internal to the CME.

Once that we have identified the region of interest from each of the two images, the geometric localization tool automatically applies several coordinate transformations. These transformations include corrections for projection effects applied to the raw pixel positions within the region of interest, using some IDL SolarSoft routine.

[10] The use of *affine geometry* is justified since the objects that are to be reconstructed are typically 200 $R_{\odot}$ away from the observer. This distance is much greater than the typical size of the objects/features and their distance from the Sun. Affine geometry assumes the observer is located at an infinite distance, such that different viewing angles can be considered parallel, and objects near the Sun appear the same size independent of their distance from the plane of the sky.

CHAPTER 4. *DATA ANALYSIS*

In this Chapter we describe the analysis of a sample of selected halo CMEs. To this end, we used the magnetograms from MDI/SOHO for the analysis of the magnetic configuration of the active regions and GOES satellite data for the information on flares. Moreover we used STEREO/EUVI images to have information on the explosive events occurring in the corona, STEREO/COR1 data to perform the 3D reconstruction of the CMEs and STEREO/COR2 and LASCO/SOHO images to study the structure of CMEs in heliosphere. The goal is to have a general view of the system *flare-CME*, starting from the active region (photosphere) to the CMEs in the corona with a 3D reconstruction.

4.1 Selection of the halo CMEs

Using CDAW Data center from LASCO and CME Catalogue from STEREO, we have analyzed the years 2010 and 2011 to choose a sample of halo CMEs. In Table 3 we report the main information on halo CMEs: time (the initial time at which the CMEs are observed from COR1 onboard STEREO satellites), active region number and coordinates, and the associated flare[11]. From this list we selected three events (highlighted in green texture).

The choice of these events was made on the basis of two considerations. The first is related to the characteristics of the associated flare, as we selected the CMEs related to the most energetic flares, the second is linked to the position of the active region, because the analysis of the relevant magnetograms is reliable only for those active regions located between ±40° of longitude on the solar disk. Moreover, in these cases, the CMEs are best observed from STEREO, since they are seen at limb from each satellite (remember that the two satellites are traveling in orbits around the Sun, while, e.g., SOHO is in a halo orbit around the Sun-Earth L1 point).

[11] Solar flares are classified as A, B, C, M or X according to the peak flux (in watts per square meter, W/m^2) X-rays near Earth, as measured on the GOES spacecraft. Each class has a peak flux ten times greater than the preceding one, with X class flares having a peak flux of order 10^{-4} W/m^2. Within a class there is a linear scale from 1 to 9, so an X2 flare is twice as powerful as an X1 flare, and is four times more powerful than an M5 flare. The more powerful M and X class flares are often associated with a variety of effects on the near-Earth space environment.

Year	Month/Day	Time (UT)	Active Region (AR)	Coord. AR	Flare associated
2010	February 7	02:45	11045	N24E01	**M6.4** (02:20)
	April 3	09:05	11059	S23W03	**B7.4** (09:04)
	May 23	16:05	11072	S16W06	**B1.4** (N19W12 16:45)
	May 24	13:05	11072	S15W23	**B1.1** (N19W20 13:05)
	August 7	18:25	11093	N12E31	**M1.0** (17:55)
	August 14	10:06	11093	N12W56	**C4.4** (09:38)
	December 14	15:25	11133	N14W62	**C2.3** (14:45)
2011	**February 15**	02:05	11158	S21W18	**X4.8** (01:56)
	March 7	20:10	11164	N24W58	**C2.3** (19:32)
	March 26	05:25	?	-	-
	April 27	02:25	?	-	-
	May 9	21:05	?	-	-

Table 3. List of halo CMEs observed by STEREO during the period February 2010-May 2011.

4.2 Analysis of the halo CMEs

We describe the analysis of the three events separately in the next paragraphs.

4.2.1 CME occurred on April 3, 2010

The CME initially observed by COR1 on April 3, 2010 at 09:05 UT is associated with a flare occurred in NOAA 11059 (S25W03) (Figure 32). The GOES 14 satellite [Stern et al., 2004] recorded in fact a B7.4 flare, beginning at 09:04 UT, with peak at 09:54 UT and ending at 10:58 UT (Figure 33), occurring in this active region. The CME occurred on 2010 April 3 produced the largest, fastest interplanetary CME (ICME) at 1 AU since the 2006 December 13 event, indicative of awakening of the Sun from a long minimum.

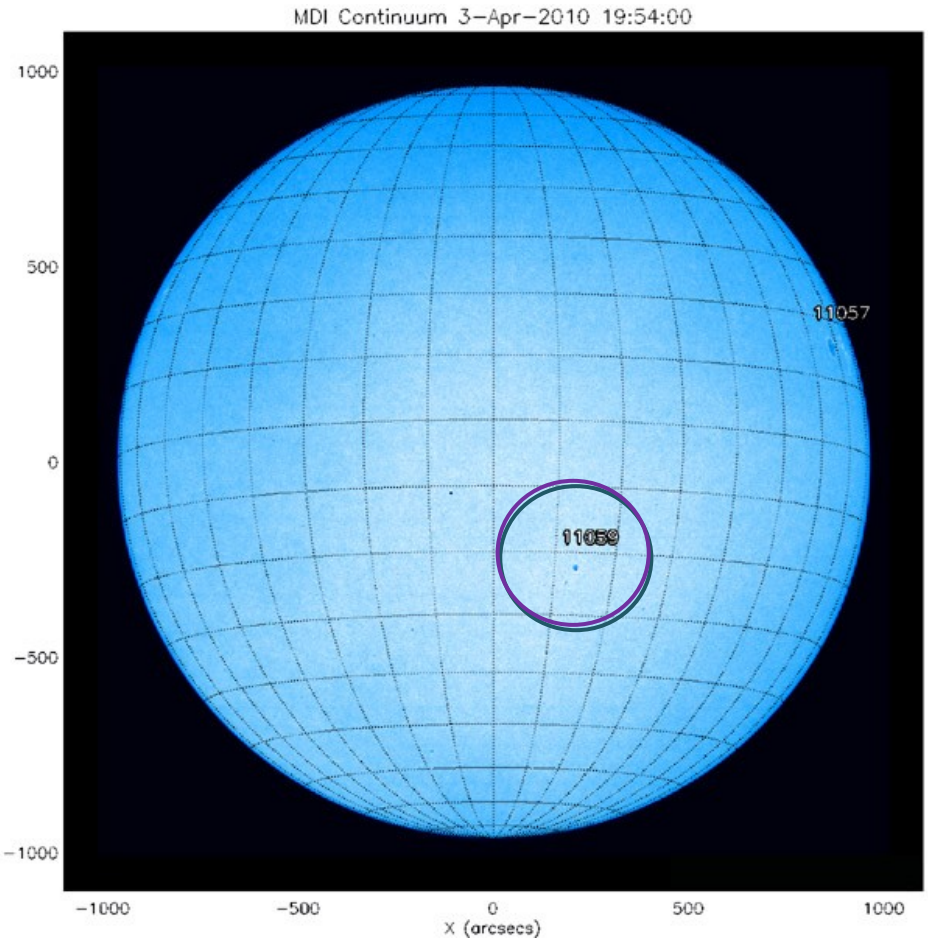

Figure 32. Image of the photosphere provided by the instrument MDI (Michelson Doppler Imager) on board SOHO, showing two groups of sunspots on April 3, 2010. In this and in the following images North is at the top, West at the right.

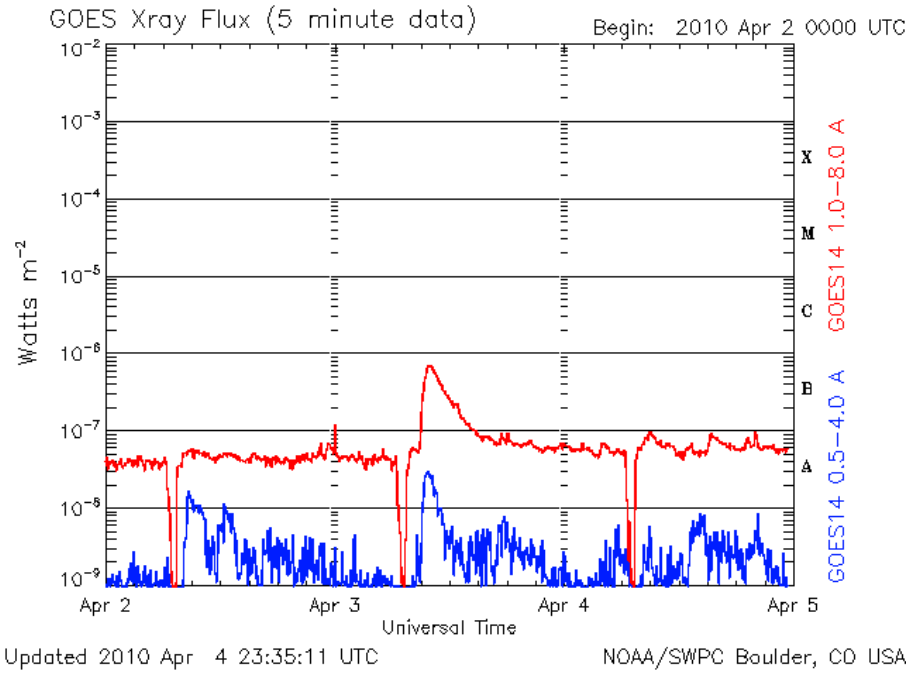

Figure 33. GOES X-ray Flux data between April 2 and 5, 2010 (NOAA).

The CME event is associated also with significant EUV dimming and waves, radio bursts, a prominent shock wave, solar energetic particle (SEP) events, and a prolonged geomagnetic storm.

- *Active region morphology*

Photospheric magnetic configuration and morphology of the active region at different atmospheric levels is shown in Figure 34.

In the magnetogram (Figure 34, top left), the active region shows a rather compact leading positive polarity and a more diffuse following negative polarity. In the photosphere (Figure 34, top right), the image shows a main sunspot, corresponding to the area of positive polarity, another smaller sunspot and several pores characterized by negative polarity.

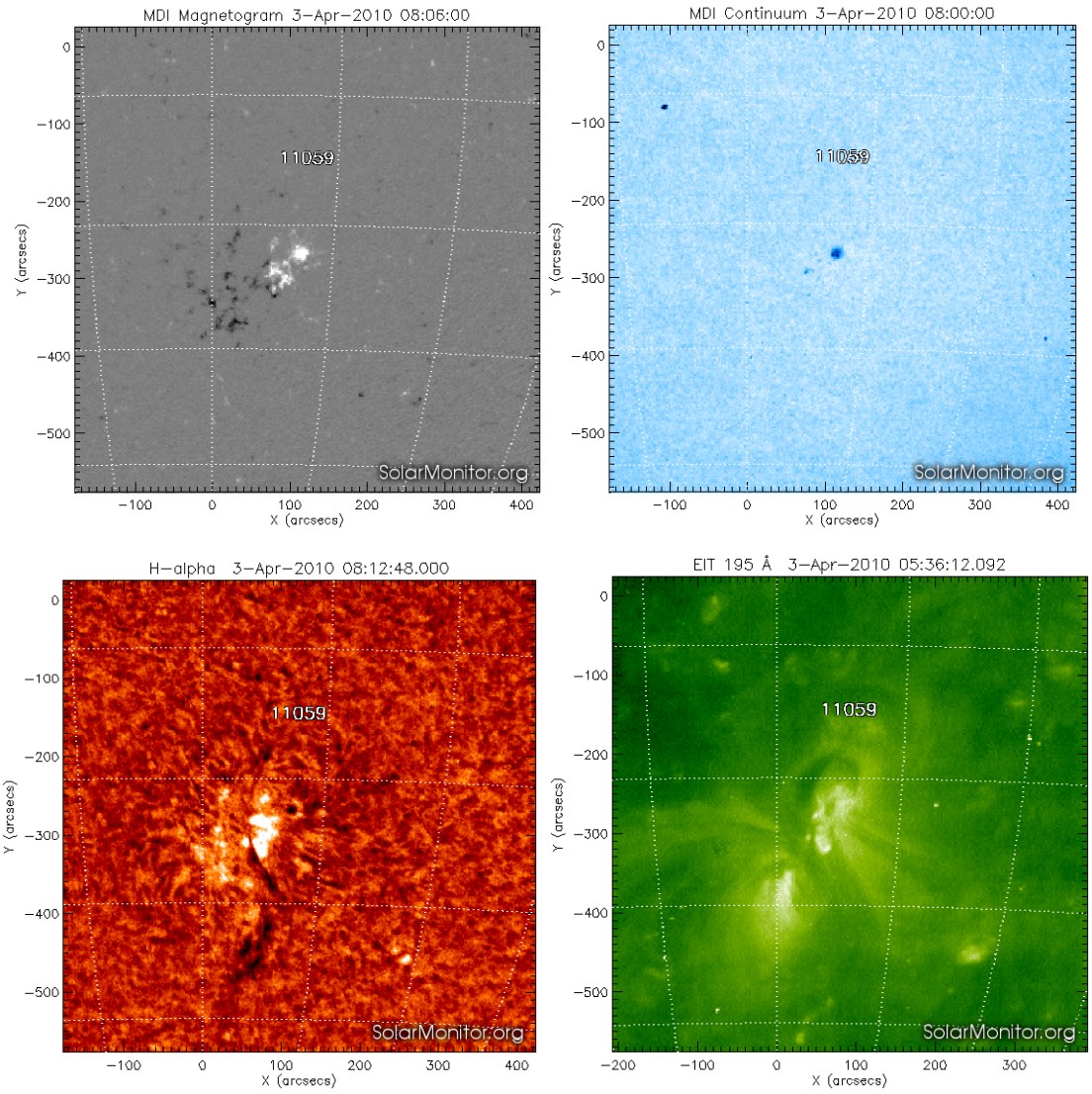

Figure 34. From left to right: MDI magnetogram; MDI WL photospheric image; Hα chromospheric image; EIT 195 Å coronal image.

In the chromosphere (Figure 34, bottom left), a very bright facular region and some filaments in the most southern part, oriented along the magnetic neutral line, are present. In the corona (Figure 34, bottom right), we can see several loops and the EUV filament channel underlying the region hosting the filaments.

- Magnetic configuration

To analyze the magnetic configuration of NOAA 11059 we used MDI/SOHO line of- sight magnetograms acquired between 00:00 UT on April 1 to 04:00 UT on April 5 2010.

We found that during these four days the magnetic flux has values within 4.2-6.0 × 10^{21} Mx (in absolute value), and is characterized by an initial decreasing trend, followed by a modest increase in the hours preceding the CME (whose timing is indicated by a dotted vertical line in the plot shown in Figure 35). After the CME, the magnetic flux shows an abrupt decrease and later on it remains almost constant (Figure 35).

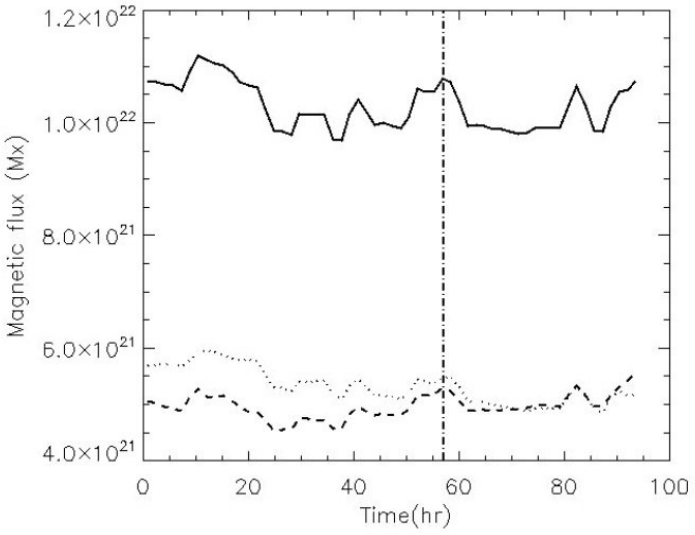

Figure 35. Magnetic flux evolution in NOAA 11059: the dotted (dashed) line indicates the positive (negative) magnetic flux, while the continuous line indicates the total unsigned magnetic flux. In the plot, t = 0 corresponds to 00:00 UT on 1 April 2010 and the dotted vertical line indicates the time of the CME occurrence (from Orlando et al., 2010).

In order to study the magnetic configuration of the active region hosting the flare associated to the CME event, we also performed a force-free field extrapolation on the MDI magnetogram acquired at 07:59 UT using the method introduced by Alissandrakis [1981] and the value for the force-free field parameter $\alpha = 0.02$.

The results show several systems or bundles of field lines (Figure 36). The yellow lines reach a height of 138 Mm; the red lines reach a height of 27 Mm; the green lines arrive at a height of 2 Mm. We note that Figure 36(a), having the same orientation as the magnetogram shown in Figure 34 (top left), the yellow bundle of field lines has the same shape of the loops observed by EIT at 195 Å (compare with Figure 34, bottom right), confirming therefore the reliability of the force-free field extrapolation.

The yellow, red and part of the green field lines outline the magnetic arcades supporting and confining the filaments seen in the Hα image shown in Figure 34 (bottom left). These field lines most probably correspond to the post-flare loop system observed in STEREO A images (compare Figure 36(a)–(c) with Figure 39).

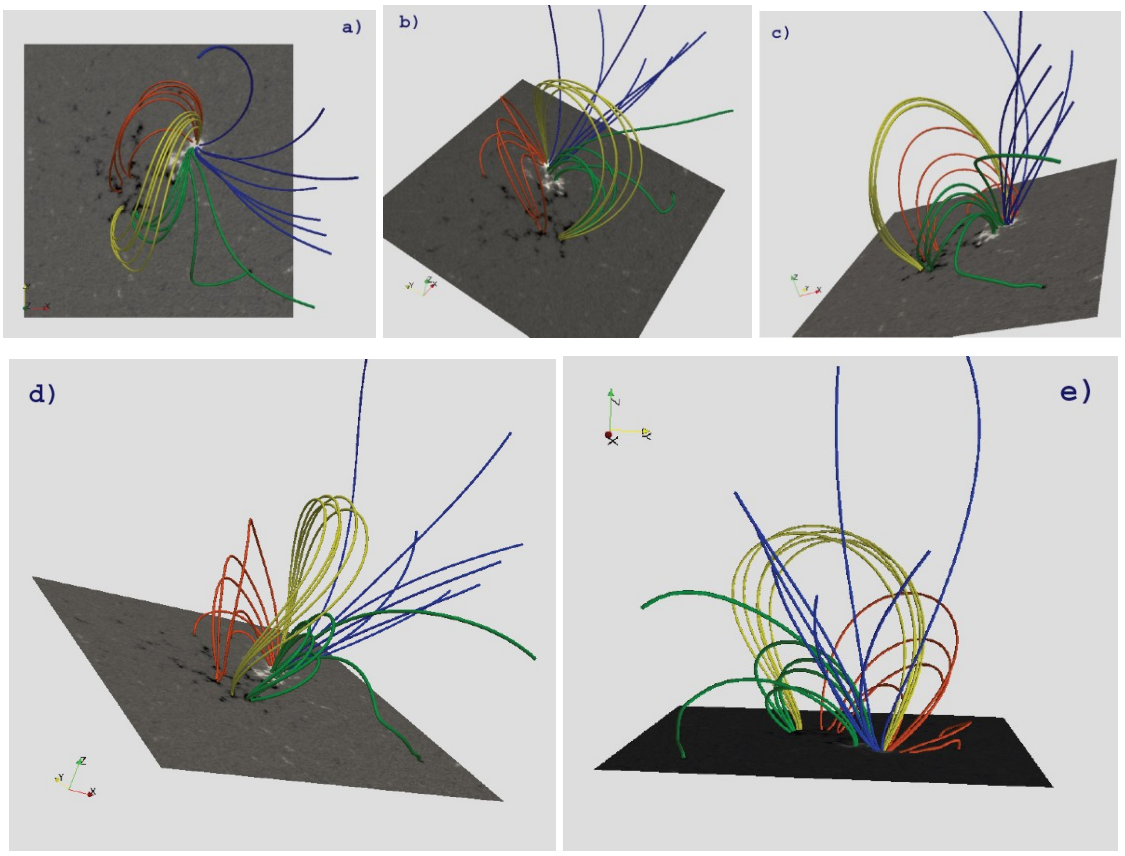

Figure 36. Force-free field extrapolation performed using the MDI magnetogram acquired at 07:59 UT. The different figures show the active region magnetic configuration from the photosphere to the corona from different view angles, in order to evidence the region hosting the filament seen in the chromosphere and the field lines connectivity (adapted from Orlando et al., 2010).

To study the magnetic helicity trend in the active region, we determined the horizontal motions of the field line footpoints using the differential affine velocity estimator (DAVE) method [Schuck, 2005], with a window size of 20 arcsec and a time interval between two successive frames of 96 min. Subsequently, we estimated the magnetic helicity rate and helicity accumulation using the method described by Pariat et al., [2005]. The results indicate that the rate of magnetic helicity is extremely variable, with an initial predominance of negative values, followed by positive values after about one day from the initial time (00:00 UT on April 1 2010). Concerning the accumulated magnetic helicity, the maximum negative value is reached at about 00:00 UT on April 2, and later the helicity increases almost continuously (Figure 37).

However, immediately after the CME occurrence, there is an abrupt decrease in the accumulated magnetic helicity.

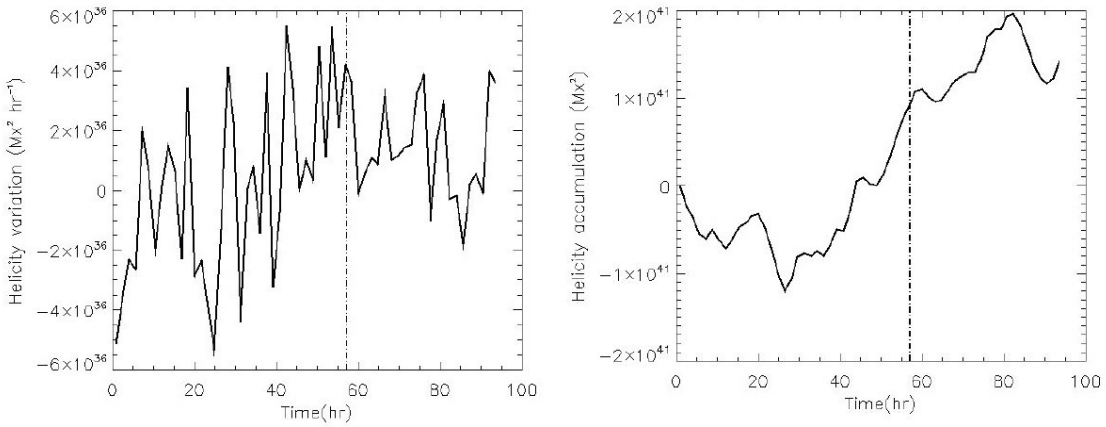

Figure 37. (left) Rate of magnetic helicity as a function of time; (right) accumulated magnetic helicity during the time interval analyzed. In the plots $t = 0$ corresponds to 00:00 UT on 1 April 2010 and the dotted vertical line indicates the time of the CME occurrence (adapted from Orlando et al., 2010).

- *The CME evolution*

On April 3, 2010 the separation angle between STEREO A and B satellites was 138.6 degrees (Figure 38).

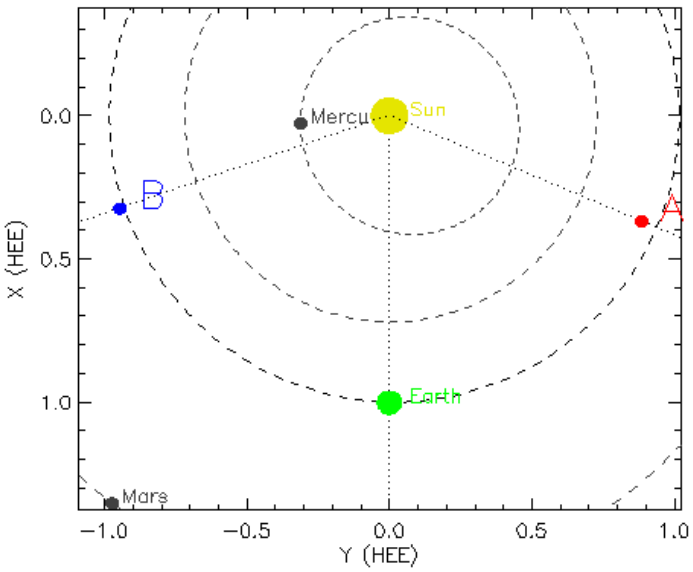

Figure 38. Graphic with the position of the twin STEREO satellites respect to the Sun and Earth on April 3, 2010 (NASA).

Figure 39 shows the AR NOAA 11059 observed by EUVI A and B, while Figure 40 shows the CME observed by COR1 A and B, respectively. The EUVI images show the evolution of the flare in the corona at 1.5 MK. In the images acquired at 09:30 UT we can see only an increase of brightness at the active region location. In the following hours a system of post-flare loops become visible.

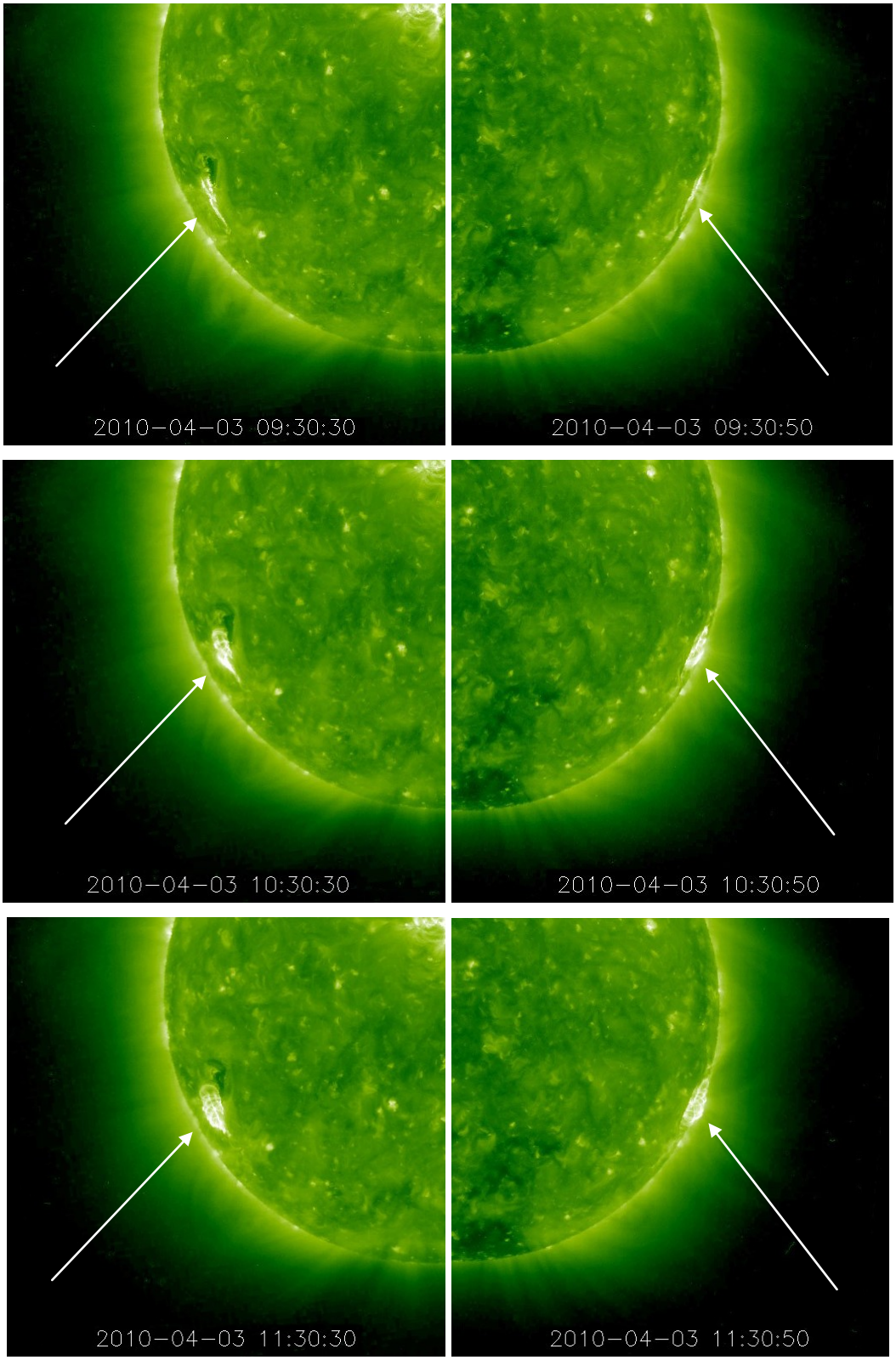

Figure 39. STEREO-EUVI A (left column) and B (right column) 195 Å zoomed images of NOAA 11059 acquired at three different times. A system of post-flare loops is visible at the flaring site (last couple images). The AR location is indicated by an arrow in each image.

In Figure 40 we can see the CME evolution at four different times (steps of fifteen minutes starting from 09:15 UT). The CME is seen at the east limb of the Sun from STEREO A and at the west limb from STEREO B. The CME seems to start from a pre-existing loop, better seen from STEREO B. The loop began to rise around 08:40 UT or earlier on April 3, which is at least 10 minutes before the flare impulsive phase.

The CME rises as a typical three-part structure in COR1, in fact we can see a bright loop, superimposed on a coronal cavity with no emission, which in turn contains high plasma density from an eruptive prominence. The CME loop quickly expands with two ends still connected to the Sun. Associated with this intense expansion is a remote deflection of coronal structures, best visible at the south of the CME loop, which indicates a pressure wave running ahead of the CME.

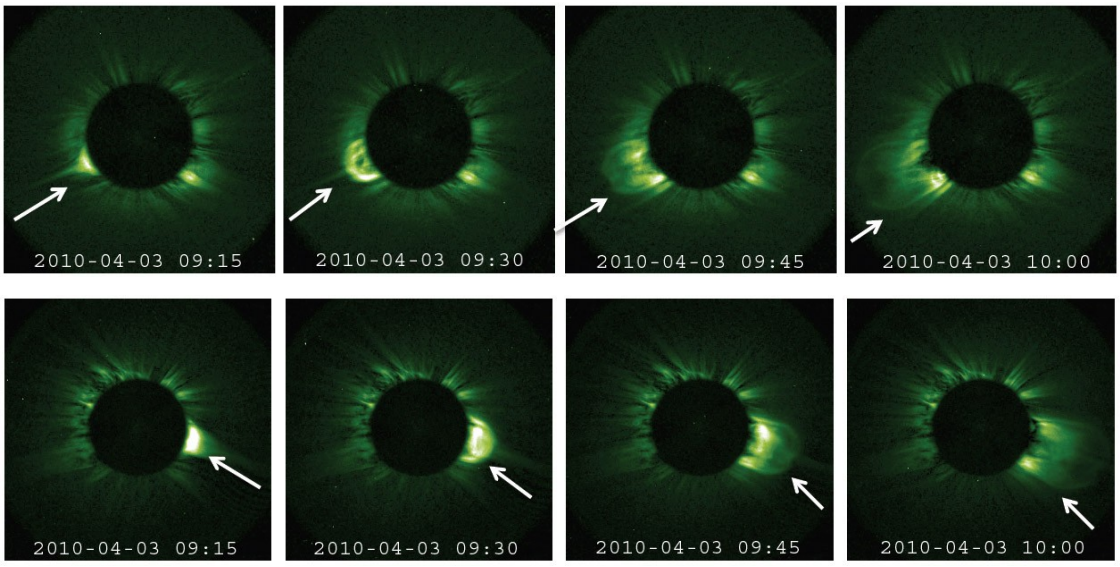

Figure 40. STEREO-COR1A (up) and COR1B (down) images showing the CME evolution at four different times. The CME location is indicated by an arrow in each image (adapted from Orlando et al., 2010).

Figure 41 shows the CME as observed by COR2. As we can see from the panels, COR2 shows very well the evolution of the ejection from 10:24 UT until 11:39 UT. The CME rises as a typical three-part structure also in COR2, but the CME is much brighter in COR2A images.

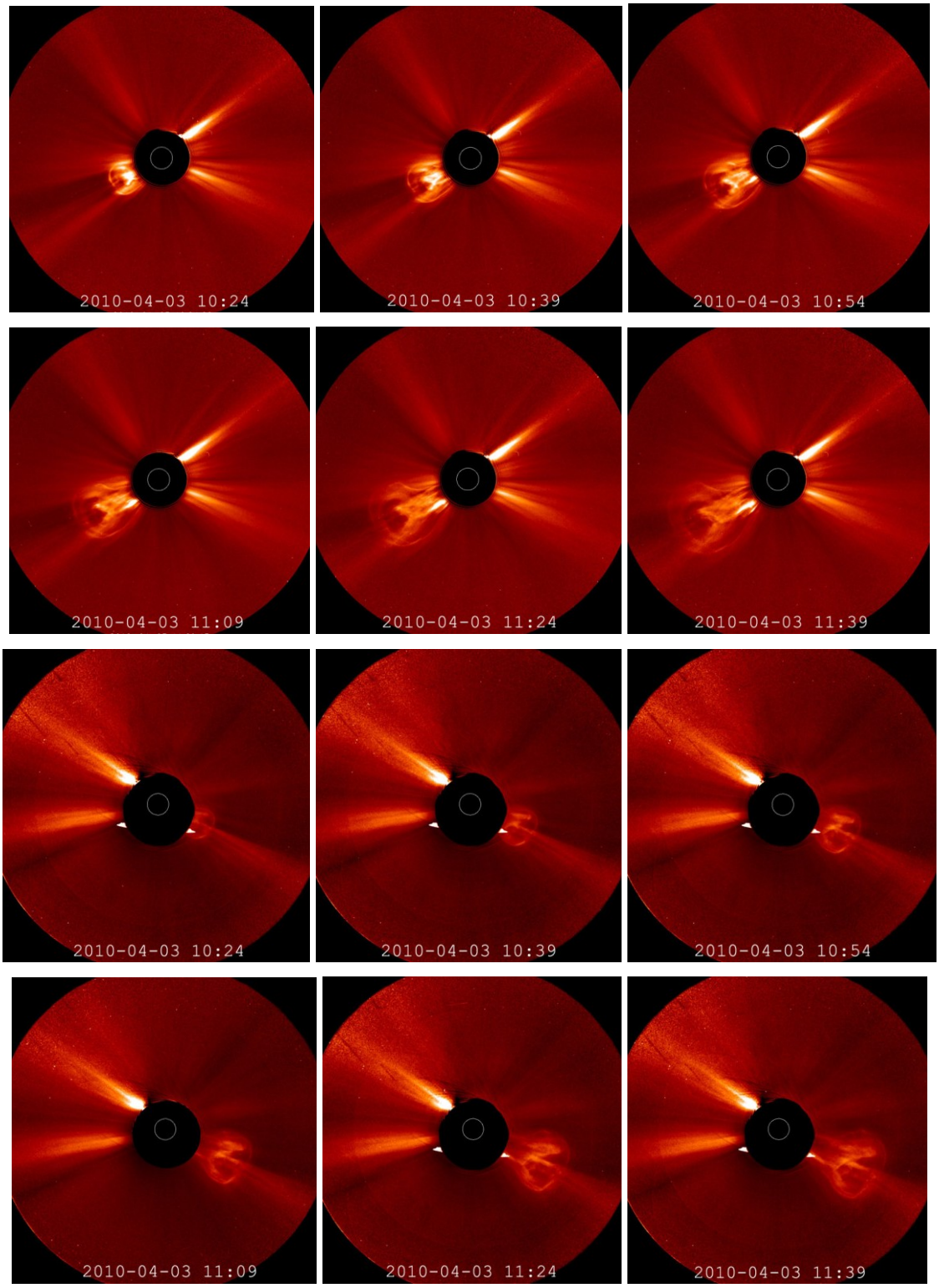

Figure 41. STEREO-COR2A (six panel up) and COR2B (six panel down) images showing the CME evolution at six different times.

To have a comparison with other spacecraft data we show, in the Figures 42 and 43, images of the CME observed on February 15, 2011 from LASCO C2 and C3 onboard SOHO satellite. As we can see the halo CME is very faint, but is observed during its expansion by both coronographs.

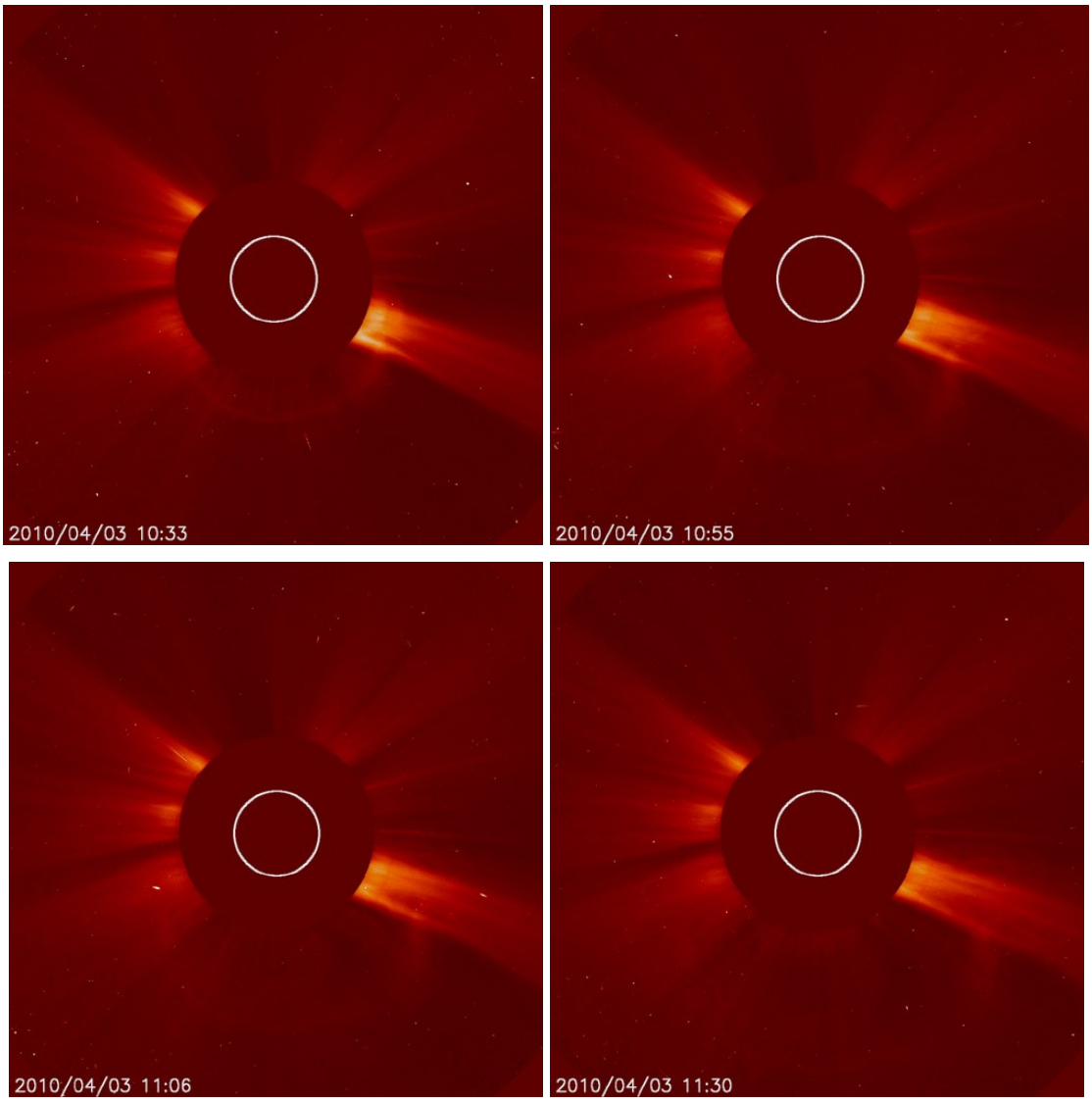

Figure 42. SOHO-LASCO C2 images showing the CME evolution at four different times.

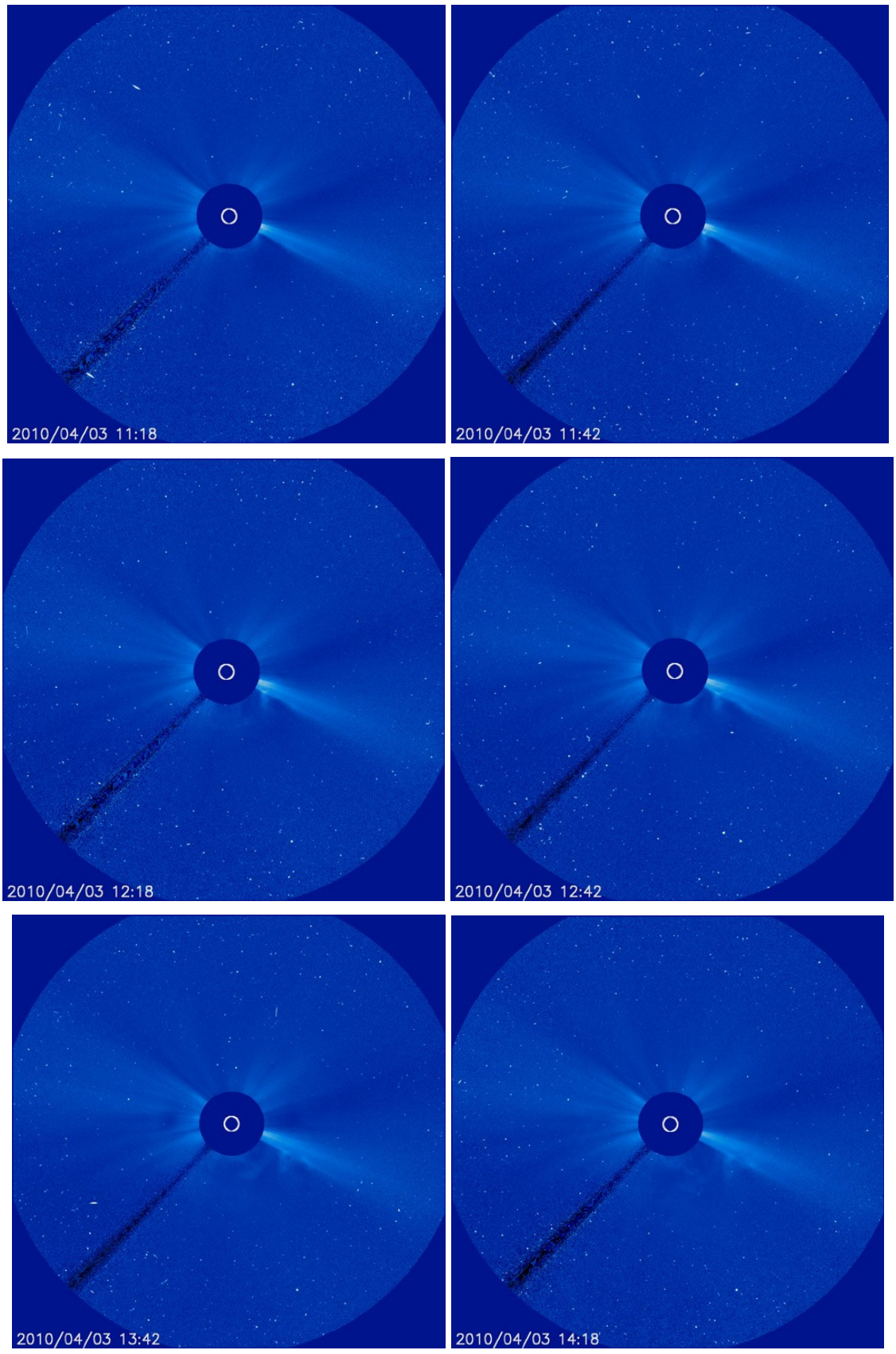

Figure 43. SOHO-LASCO C3 images showing the CME evolution at six different times.

In order to determine the global configuration of the solar magnetic field, we used a procedure that allows us to perform a non-linear force free field extrapolation, using the full-disk MDI line of sight magnetogram. The procedure, called PFSS, provides the magnetic field configuration from different view points, allowing therefore to determine how the global magnetic field is from an Earth point of view and also from the point of view of both STEREO A and B. In Figure 44 we show the initial MDI magnetogram and in Figure 45 the results of the extrapolation. These extrapolations show that the bright leading edge of the CME observed in STEREO A and B images correspond to the system of magnetic field lines inferred by the force-free extrapolation and allows us to conclude that the front edge of the CME was initially confined by this systems of loops, which on the other hand re-form and reconnect after the explosive event.

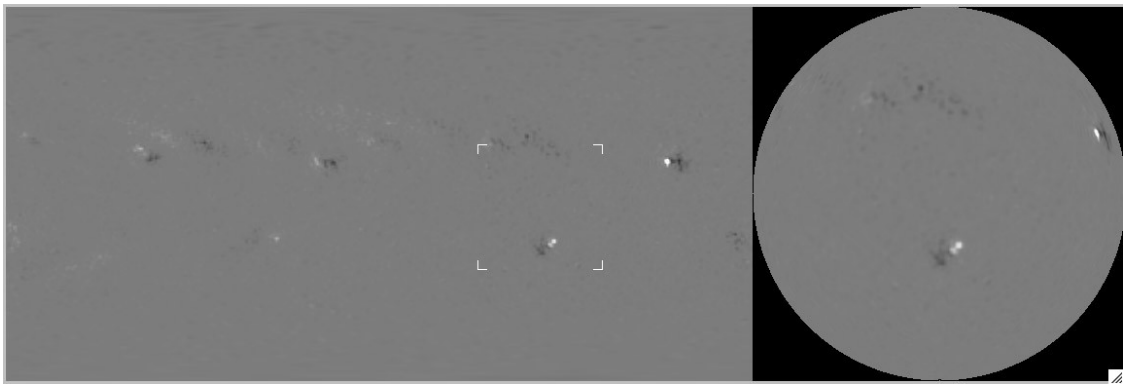

Figure 44. Left: MDI image of the radial component of the photospheric magnetic field in a rectangular latitude-longitude (Carrington) projection. The corners indicate the field of view including the active region of interest. Right: MDI full disk magnetogram acquired on 3 April 2010.

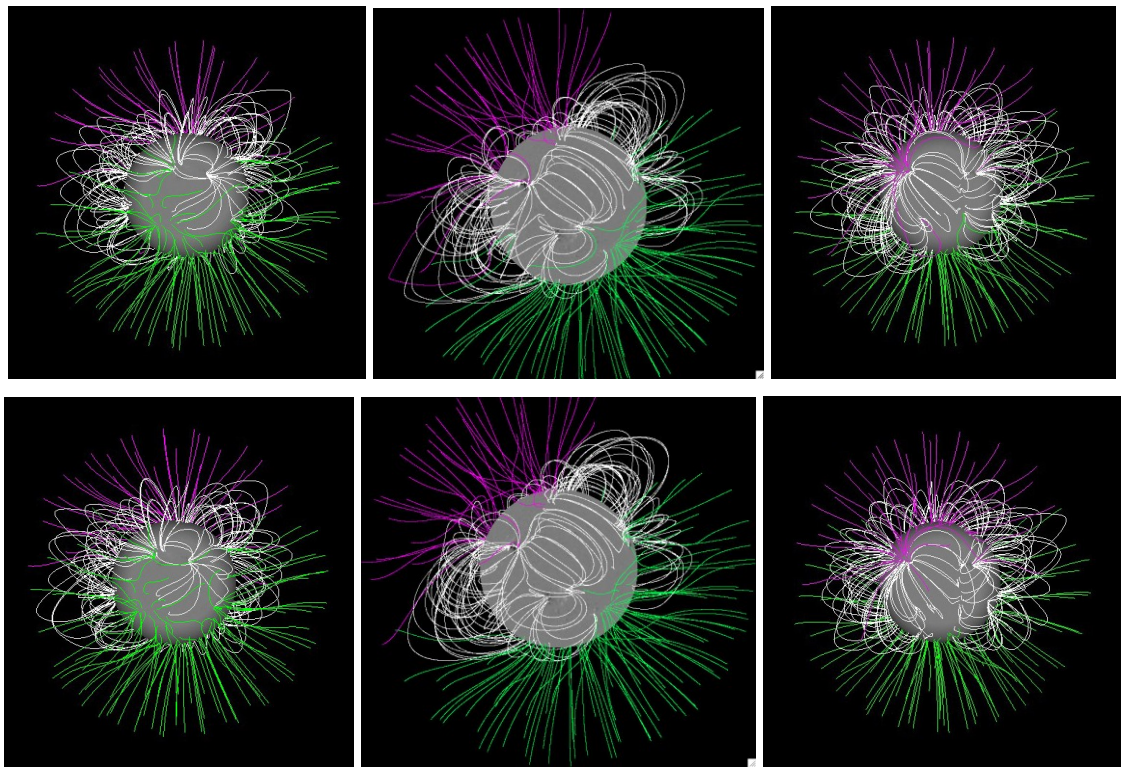

Figure 45. Results obtained from the PFSS, showing the global magnetic field configuration of the full Sun. Top panel: results obtained from the magnetogram acquired at 06:04 UT on 3 April (before the event) from a STEREO A view (left), Earth view (center) and STEREO B view (right). The active region of interest is at the center of the solar disk. Bottom panel: extrapolations relevant to the magnetogram acquired at 12:04 UT on 3 April (after the event).

Figure 46 shows the LCT-TP reconstruction from three different points of view. The coordinate system is HEEQ, with the origin in the Sun center, X pointing towards Earth and Z towards the solar north. The colors indicate the distance from the Sun center: yellow-red closest to the Sun and blue closest to the Earth.

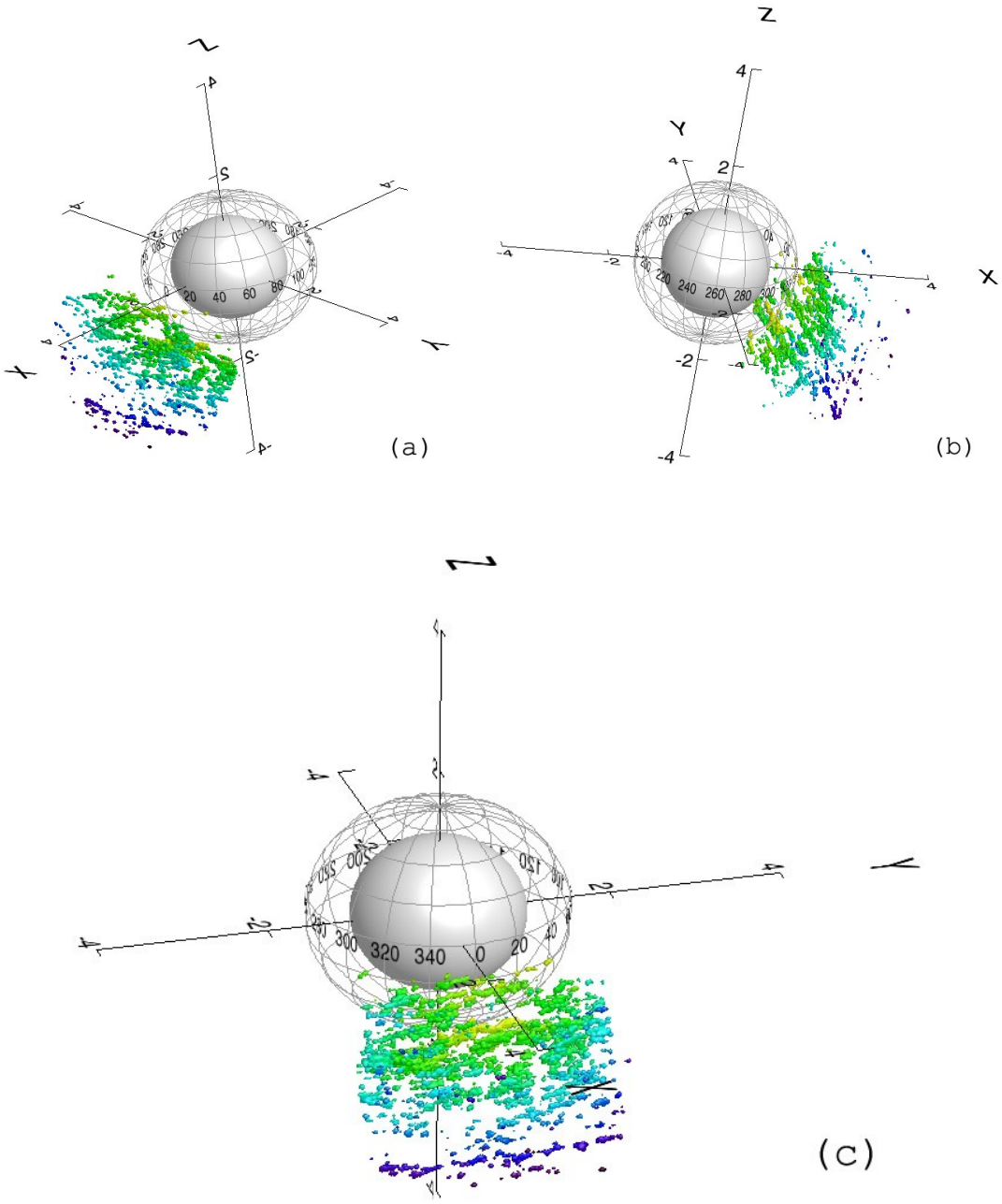

Figure 46. (a) CME 3D reconstruction from STEREO A view point at 09:45 UT, as seen edge-on; (b) CME 3D reconstruction as seen by STEREO B; (c) CME 3D reconstruction as seen by the Earth (adapted from Orlando et al., 2010).

Figure 46(a) shows the 3D reconstruction from A view point at 09:45 UT, as seen edge-on (compare with Figure 42, showing the image acquired by COR1A at 09:30 UT); Figure 46(b) reports the reconstruction edge-on at the same time by STEREO B

(compare with Figure 42, relevant to the acquisition of COR1B at 09:30 UT); Figure 46(c) reports the CME 3D reconstruction as seen by the Earth.

The CME kinematics in the ecliptic plane are displayed in Figure 47. In the upper panel we can see the trend of the propagation direction ,which is converted to an angle with respect to the Sun–Earth line. If the angle is positive (negative), the CME feature would be propagating west (east) of the Sun–Earth line in the ecliptic plane. The plot indicates that the CME leading edge shows an indication of transition from eastward to westward at the early stage. After the westward transition the propagation direction stays around 10° west of the Sun–Earth line, although a slight tendency of moving eastward is observed at large distances [Liu et al, 2011]. The CME leading edge can be tracked out to 165 solar radii or 0.75 AU (without projection), a far more extensive region of the heliosphere than previously possible with coronagraph observations.

The central panel shows the increase of the radial distance of the CME edge as a function of time. The plot clearly shows that the distance increases linearly with time.

The speed first rises to 1000–1100 km/s and then decreases to about 800 km/s, which is likely the value measured in situ at 1 AU, presumably owing to interactions with the background heliosphere [Liu et al., 2011]. The CME is still accelerating even after the flare maximum, as indicated by the timing with the GOES X-ray curve.

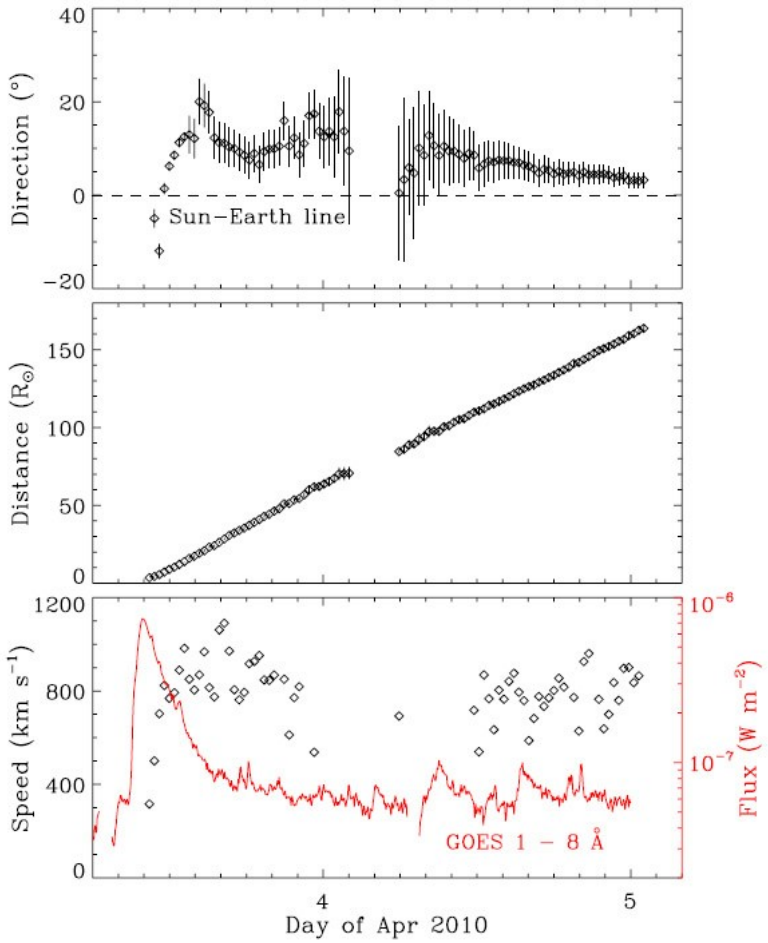

Figure 47. Propagation direction, radial distance, and speed of the CME leading edge derived from geometric triangulation. In the top panel the dashed line indicates the Sun–Earth line. Error bars represent uncertainties mathematically derived from the measurements of elongation angles. In the central panel it is shown the radial distance out to 165 $R_{\odot}$. The data gap in the propagation angle and distance is due to singularities in the calculation scheme caused by the large spacecraft separation. In the bottom panel the speeds are calculated from adjacent distances using a numerical differentiation with three-point Lagrangian interpolation. Overlaid on the speeds is the GOES X-ray flux (scaled by the red axis) (from Liu et al., 2011).

4.2.2 CME occurred on August 7, 2010

The second event analyzed is a halo CME initially observed by COR1 on August 7, 2010 at 18:25 UT. The GOES 14 satellite recorded an M1.0 flare (Figure 48), beginning at 17:55 UT, with peak at 18:24 UT and ending at ~24:00 UT, occurring in NOAA 11093 (N12E31) (Figure 49).

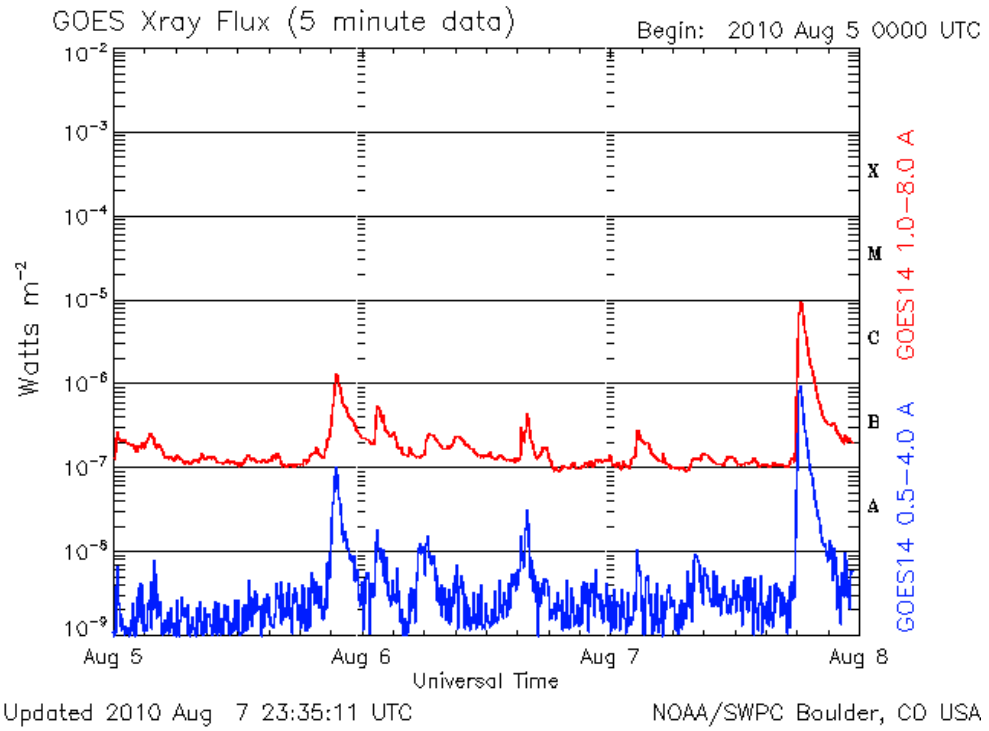

Figure 48. GOES X-ray Flux data between August 5 and 8, 2010 (NOAA).

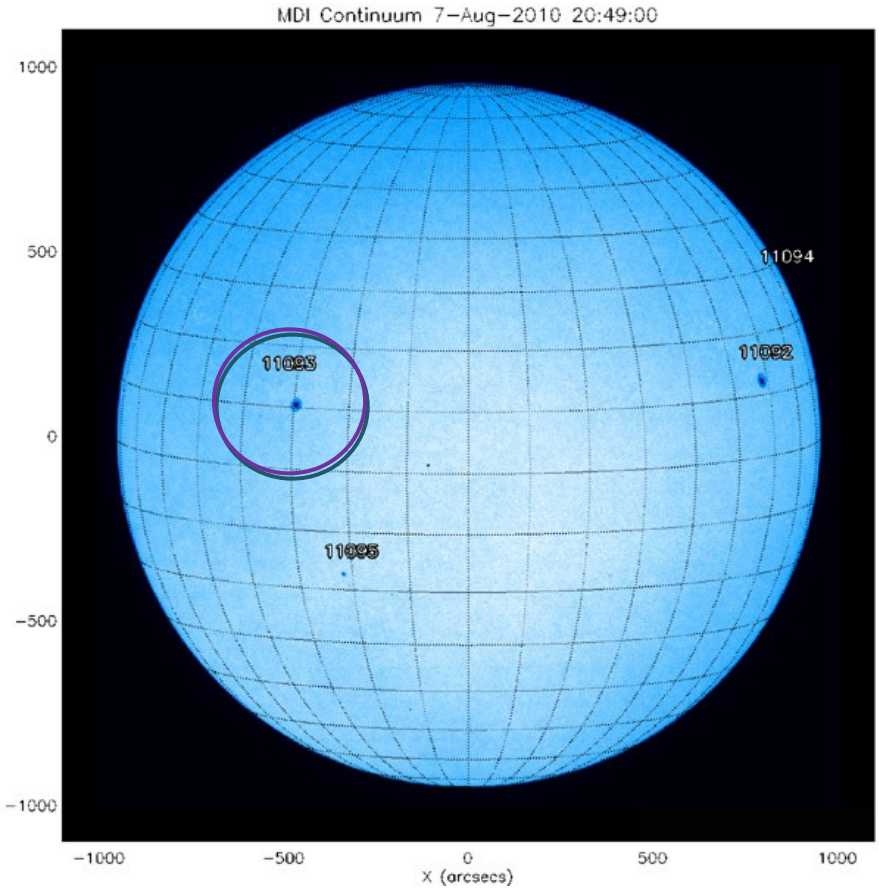

Figure 49. Image of the photosphere provided by the instrument MDI (Michelson Doppler Imager) on board SOHO, showing several groups of sunspots and the active region of interest (circled in purple) on August 7, 2010.

- *Active region morphology*

Photospheric magnetic configuration and morphology of the active region at different atmospheric levels is shown in Figure 50. In the magnetogram (Figure 50, top left), the active region shows a strong negative magnetic field concentration in the most western side and in the surroundings diffuse negative and positive polarity. In the photosphere (Figure 50, top right), the image shows a main sunspot, corresponding to the area of negative polarity, and some small pores. In the chromosphere (Figure 50, center left), a very bright facular region and several filaments in the northern part, oriented along the magnetic neutral line, are present.

In the corona (Figure 50, center right and bottom), we can see several loops, as well as the EUV filament channels underlying the region hosting the filaments.

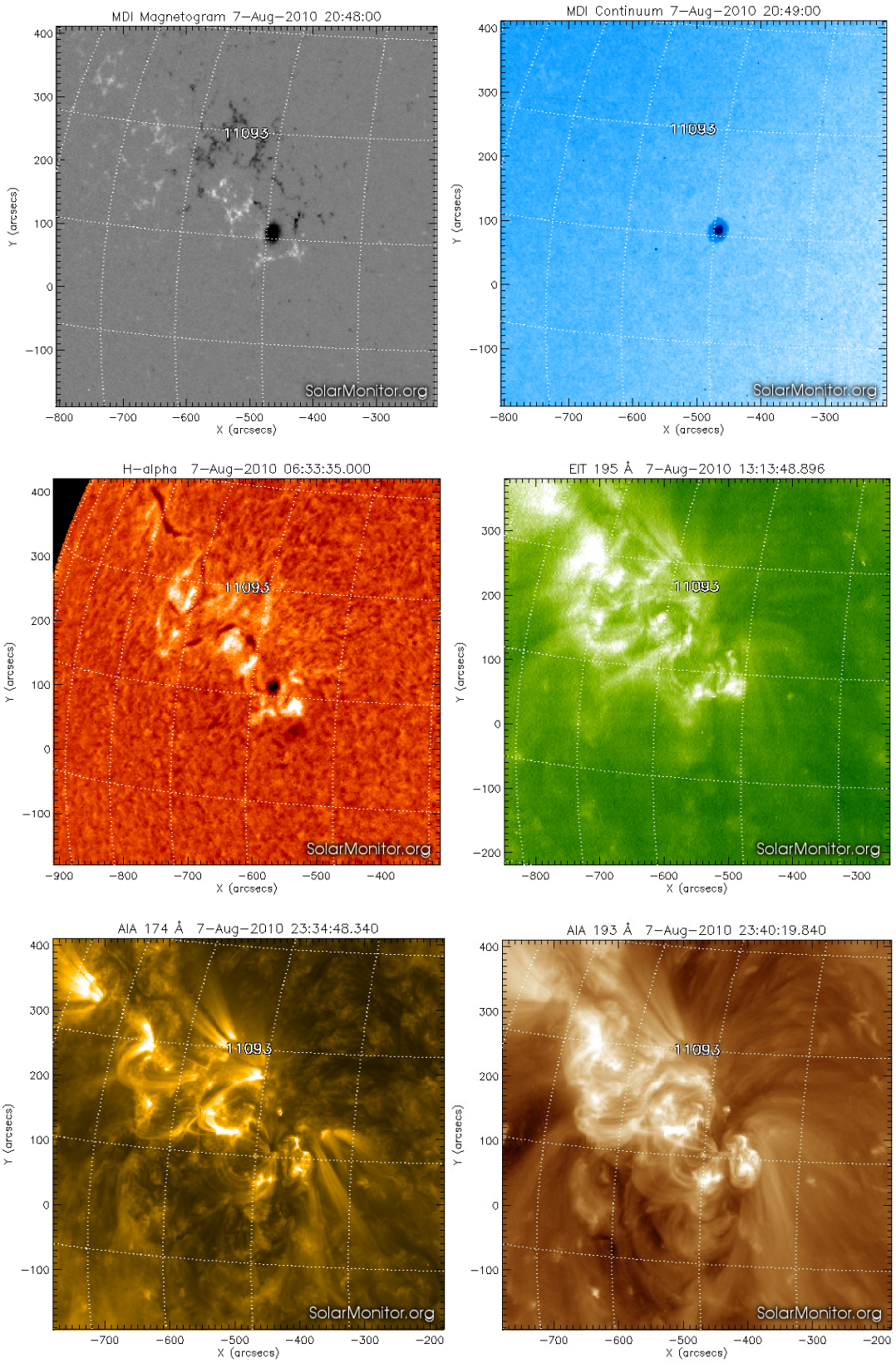

Figure 50. From left to right: MDI magnetogram; MDI WL photospheric image; Hα chromospheric image; EIT 195 Å coronal image; AIA 174 Å coronal image; AIA 193 Å coronal image.

- Magnetic configuration

To analyze the magnetic configuration of NOAA 11093 we used MDI/SOHO line of-sight magnetograms acquired between 06:27 UT and 22:24 UT on 7 August 2010.

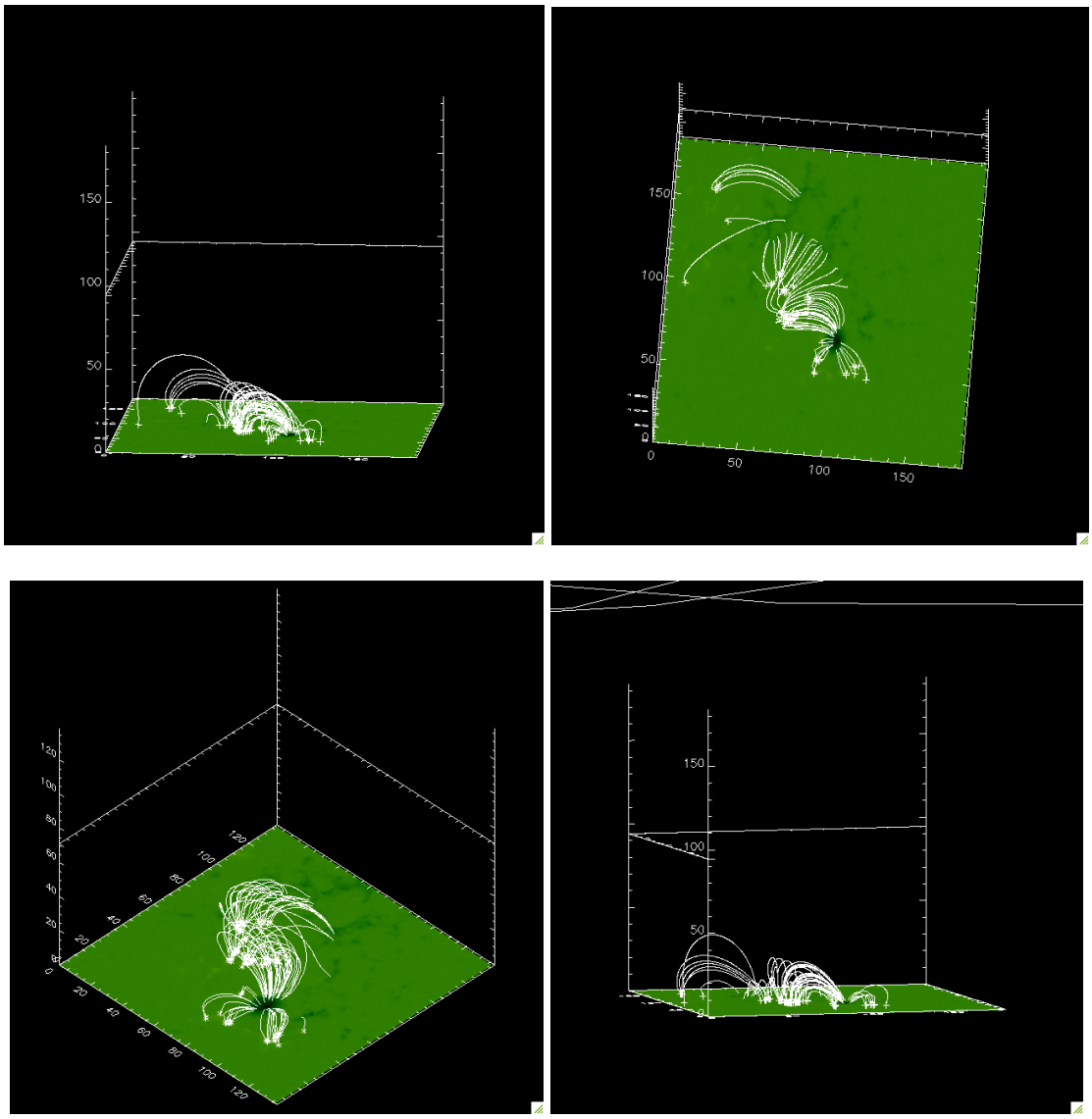

Figure 51. Force-free field extrapolation performed using the MDI magnetogram acquired on 7 August 2010 at 17:39 UT for AR NOAA 11093. Each figure shows the active region magnetic configuration from the photosphere to the corona from different view angles, in order to evidence the different magnetic loop systems and the different field lines connectivity.

Figure 51 shows the results obtained from the force-free field extrapolation performed on the magnetogram acquired at 17:39 UT (some tens of minutes before the flare occurrence), using the value 0.02 for the α force free parameter. The analysis of these extrapolations clearly shows the great complexity of the active region from where the CME originated. The images in the top panel show the field connectivity betweeen the main negative spot and the smaller positive spots and pores.

Moreover, the different orientations of the figures (both in the top and in the bottom panel) show the presence of different bundles of magnetic field lines, characterized by different magnetic connectivity: a complex configuration which can easily become unstable and give rise to the destabilization of the filaments in the active region and to magnetic reconnection. It is also worthwhile to mention that the field line configuration is quite similar to the loop systems observed in the AIA 174 and 193 Å images (compare with Figure 50).

- *The CME evolution*

On 7 August 2010 the separation angle between STEREO A and B satellites was 150.5 degrees (Figure 52).

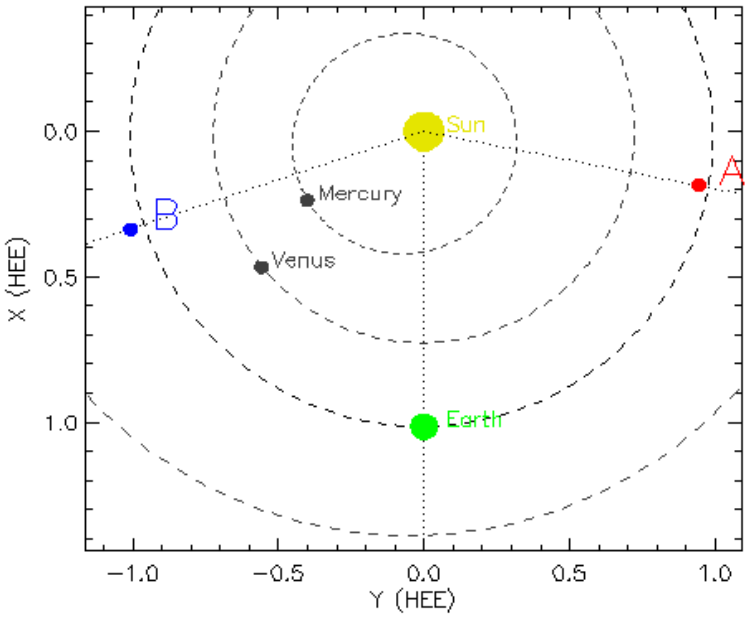

Figure 52. Graphic with the position of the twin STEREO satellites respect to the Sun and Earth on August 7, 2010 (NASA).

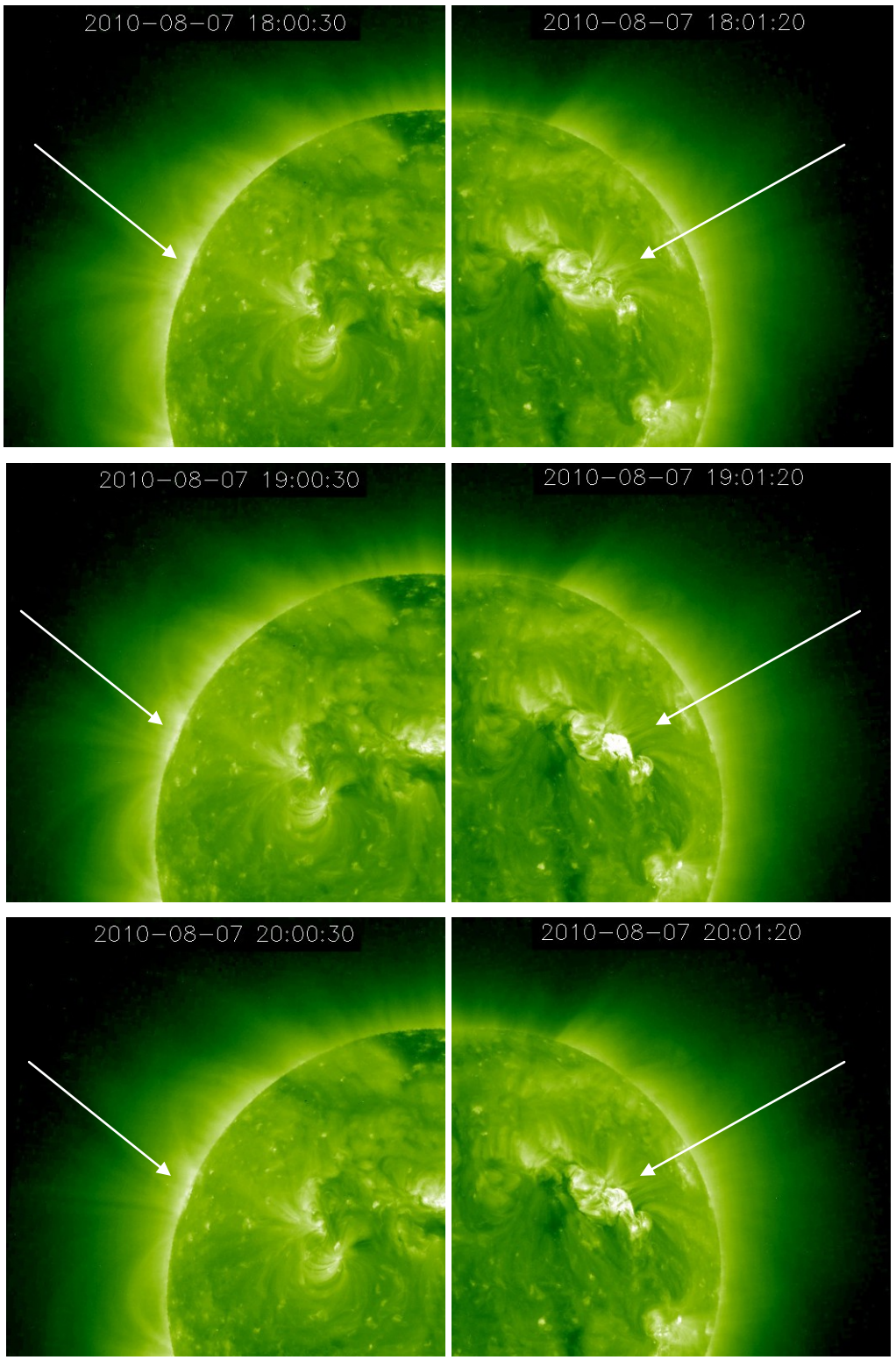

Figure 53. STEREO-EUVI A (left column) and B (right column) 195 Å zoomed images of NOAA 11093 acquired at three different times. The AR location is indicated by an arrow in each image.

Figure 53 shows the AR NOAA 11093 observed by EUVI A and B: we can see that the AR is hardly visible by STEREO A, being behind the east limb, while the flare evolution can be followed in the STEREO B images. We note a strong increase of brightness in the central part of the active region, with the formation, also in this case, of post-flare loops.

Figure 54 shows the CME as observed by COR1 A and B, respectively; we can see the CME evolution at four different times (steps of 10 minutes starting from 18:20 UT). The CME is seen at the east limb of the Sun from STEREO A and in the western hemisphere from STEREO B.

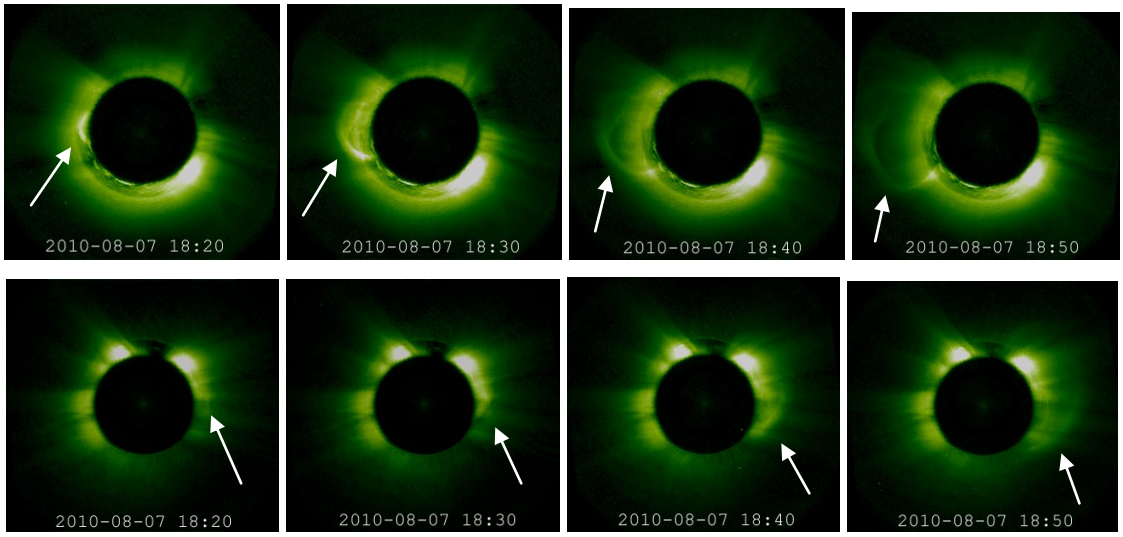

Figure 54. STEREO-COR1A (up) and COR1B (down) images showing the CME evolution at four different times. The CME location is indicated by an arrow in each image. The CME is more visible in COR1A images.

Also in this case the CME rises as a typical three-part structure, showing a bright loop, superimposed on a dark cavity enclosing bright plasma. However, in this event (see also Figure 55), the most external bright loop seems to be initially connected in both northern and southern hemisphere. The CME bright edge quickly expands with these two ends still connected to the Sun.

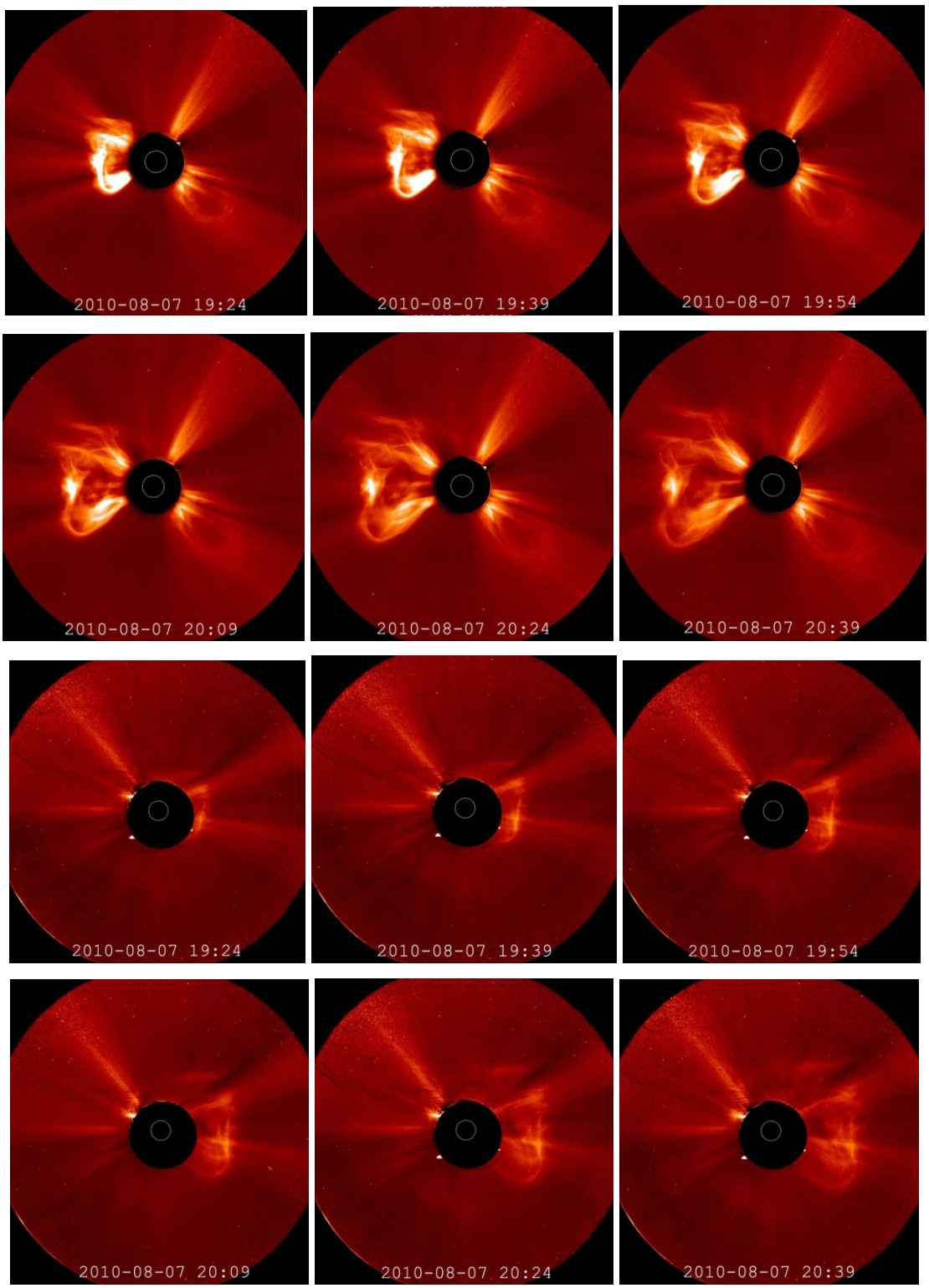

Figure 55. STEREO-COR2A (six panel up) and COR2B (six panel down) images showing the CME evolution at six different times.

Figure 55 shows the CME as observed by COR2. As we can see from the panels, COR2 shows very well the evolution of the CME from 19:24 UT until 20:39 UT, especially STEREO-COR2A (six panel up), while in the COR2B images (six panel down) the ejection is rather faint.

For this event we have no data from other spacecraft, like SOHO, so we could not compare the images with the other satellite.

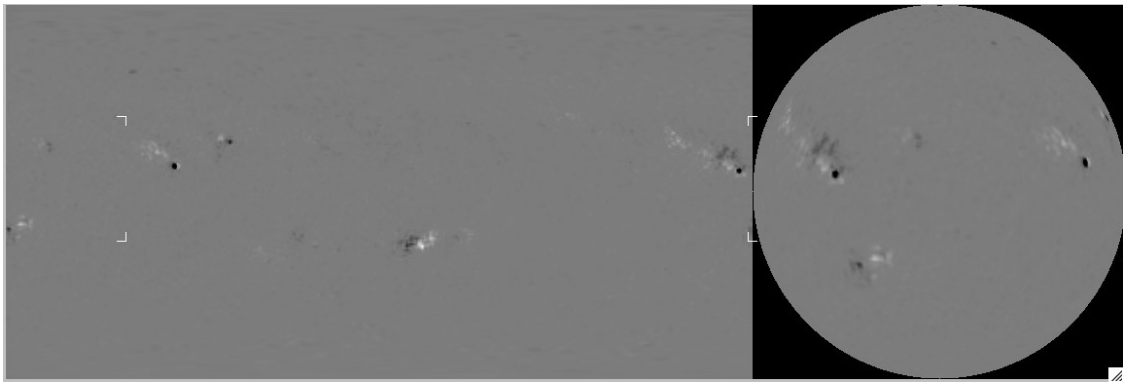

Figure 56. Left: MDI image of the radial component of the photospheric magnetic field in a rectangular latitude-longitude (Carrington) projection. Right: MDI full disk magnetogram acquired on 7 August 2010.

Also in this case, in order to determine the global configuration of the solar magnetic field, we used the PFSS procedure, to infer how the global magnetic field appears from the three different points of views (Earth, STEREO A and STEREO B).

In Figure 56 we show the initial MDI magnetogram and in Figure 57 the results of the extrapolation. The extrapolation shows that the bright leading edge of the CME observed in STEREO A and B images does not clearly corresponds to the systems of magnetic field lines inferred by the force-free field extrapolation (as stressed before, in this CME the leading edge seems to be initially connected to both hemispheres).

However, it is possible that this inconsistency is due to a limitation of the PFSS procedure, which probably is not able to trace the field lines when these are anchored in both hemispheres.

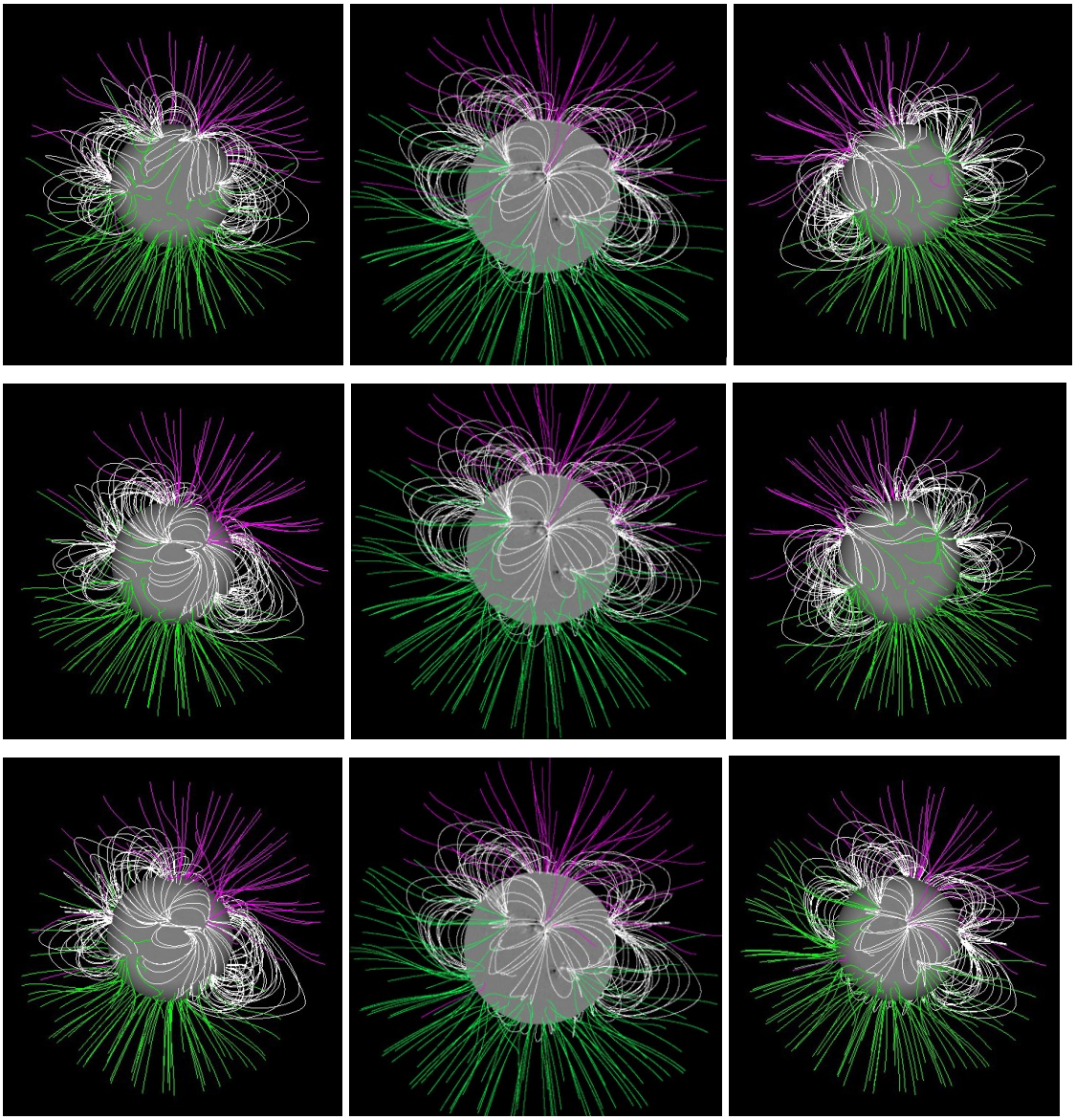

Figure 57. Results obtained from the PFSS, showing the global magnetic field configuration of the full Sun. Top panel: results obtained from the magnetogram acquired at 12:04 UT on 7 August (before the event) from a STEREO A view (left), Earth view (center) and STEREO B view (right). The active region of interest is at the center of the solar disk. Central panel: extrapolations relevant to the magnetogram acquired at 18:04 UT on 7 August (at the time of the CME first observation). Bottom panel: extrapolations relevant to the magnetogram acquired at 00:04 UT of 8 August (after the event).

Figure 58(a) shows the 3D reconstruction from A view point at 18:45 UT, as seen edge-on (compare with Figure 54 acquired by COR1A at 18:30 UT); Figure 58(b) reports the reconstruction edge-on at the same time by STEREO B (compare with

Figure 54 COR1B at 18:30 UT); Figure 58(c) reports the CME 3D reconstruction as seen by the Earth.

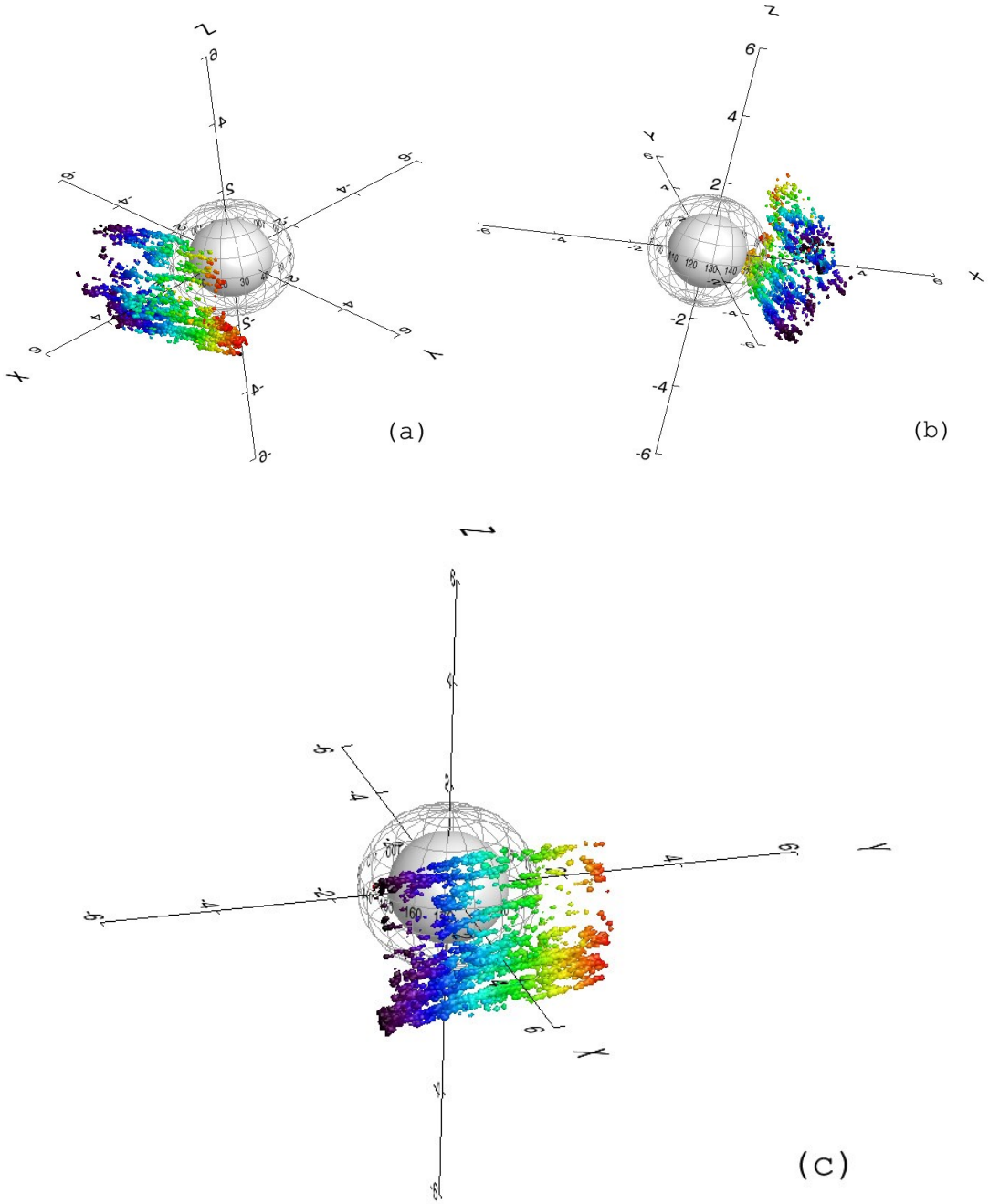

Figure 58. (a) CME 3D reconstruction from STEREO A view point at 18:45 UT, as seen edge-on; (b) CME 3D reconstruction as seen by STEREO B; (c) CME 3D reconstruction as seen by the Earth.

These reconstructions are able to show the wide latitudinal extension of this CME, and in particular the fact that the plasma seems to be ejected from both the northern and the southern hemisphere. This result is quite interesting, especially if referred to the break-out model [Antiochos et al., 1999].

Information on the CME kinematics in the ecliptic plane are displayed in Figure 59, where we can see from the plot on the right a linear increase of the height of the bright edge above the solar surface, and that the linear speed is about 870 km/s, while in the second order fit the speed is initially about 1000 km/s and then decreases to about 800 km/s.

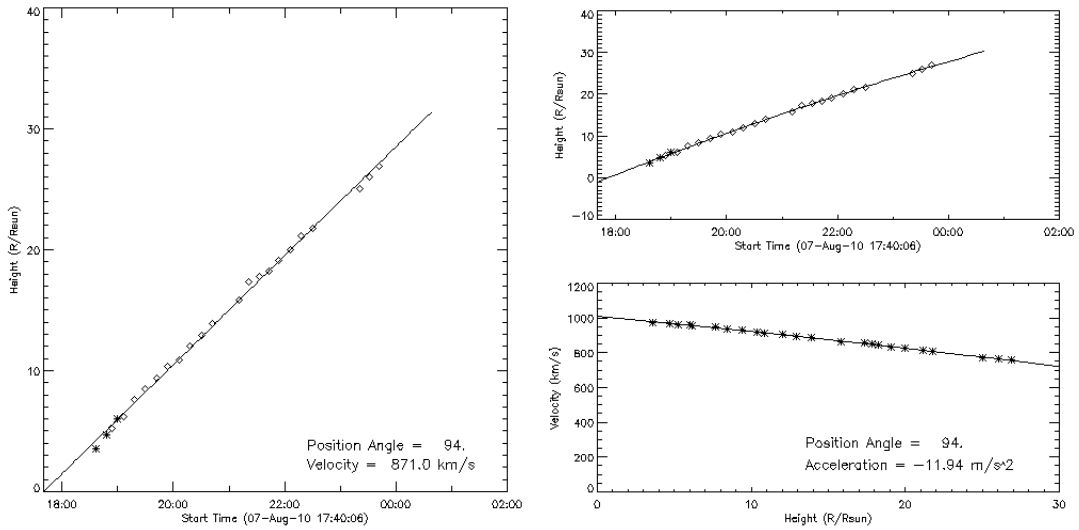

Figure 59. Linear fit (left) and 2nd order fit (right) plots. Radial distance and speed of the CME leading edge derived from the LASCO catalogue (CDAW/NASA).

4.2.3 CME occurred on February 15, 2011

The third event analyzed is a halo CME occurred on February 15, 2011 at 02:05 UT. The GOES 14 satellite recorded an X4.8 flare (Figure 60), beginning at 01:44 UT, with peak at 01:45 UT and ending at ~06:00 UT, occurring in NOAA 11158 (S21W18) (Figure 61).

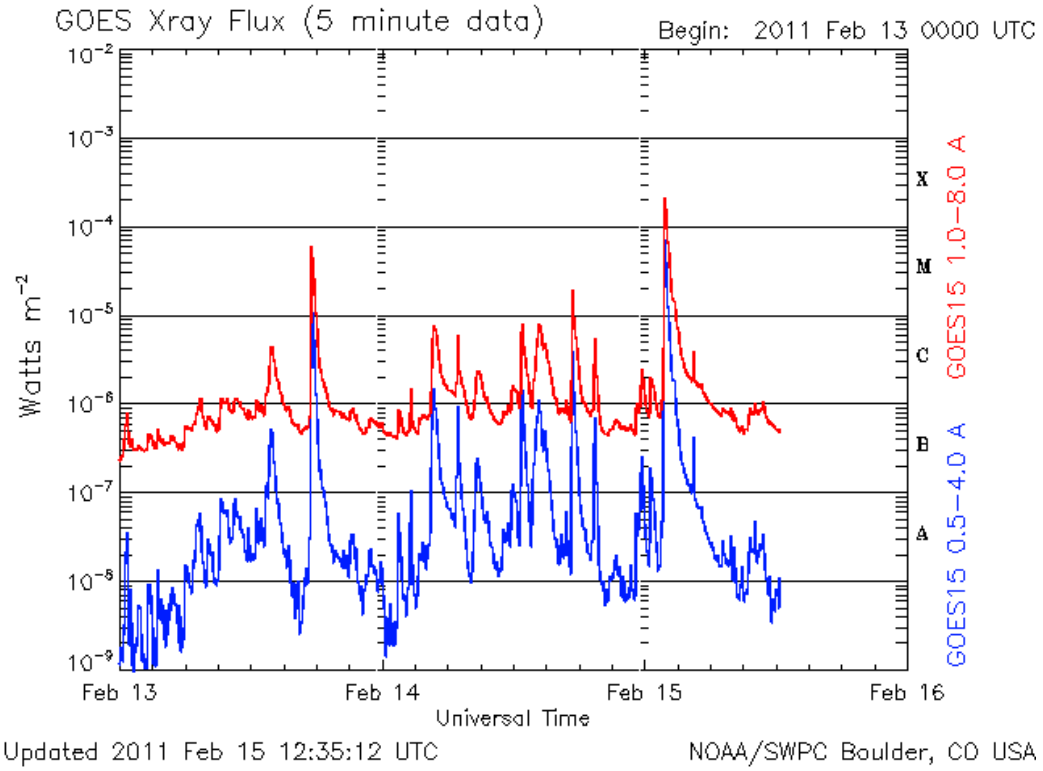

Figure 60. GOES X-ray Flux data between February 13 and 16, 2011 (NOAA).

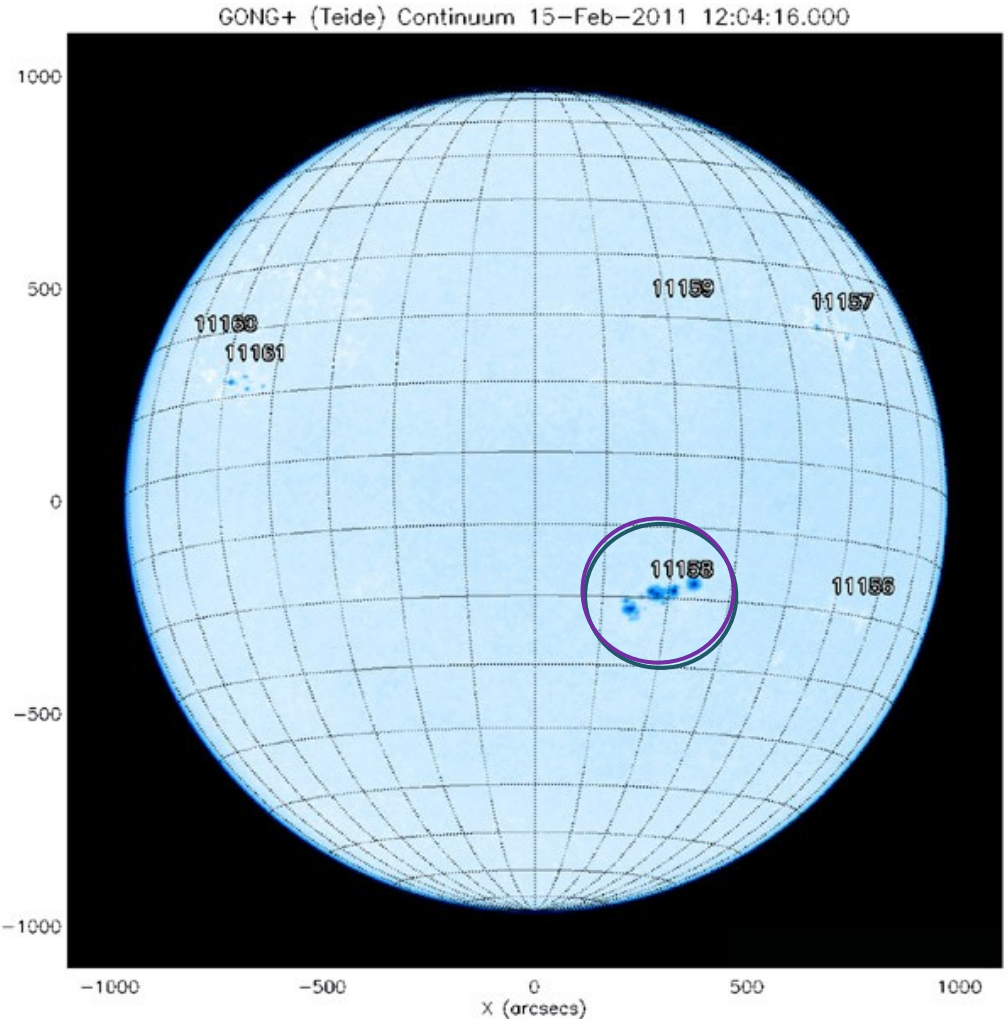

Figure 61. Image of the photosphere provided by the GONG weather station on Teide's Observatory, showing several groups of sunspots and the active region of interest (circled in purple) on February 15, 2011.

- *Active region morphology*

The photospheric magnetic configuration and morphology of the active region at different atmospheric levels is shown in Figure 62. In the magnetogram (Figure 62, top left), the active region shows rather compact negative and positive polarities. In the photosphere (Figure 62, top right), the image shows several sunspots. In the chromosphere (Figure 62, center left), a very bright facular region and some filaments are present. In the corona (Figure 62, center right and bottom), we can see several systems of bright loops.

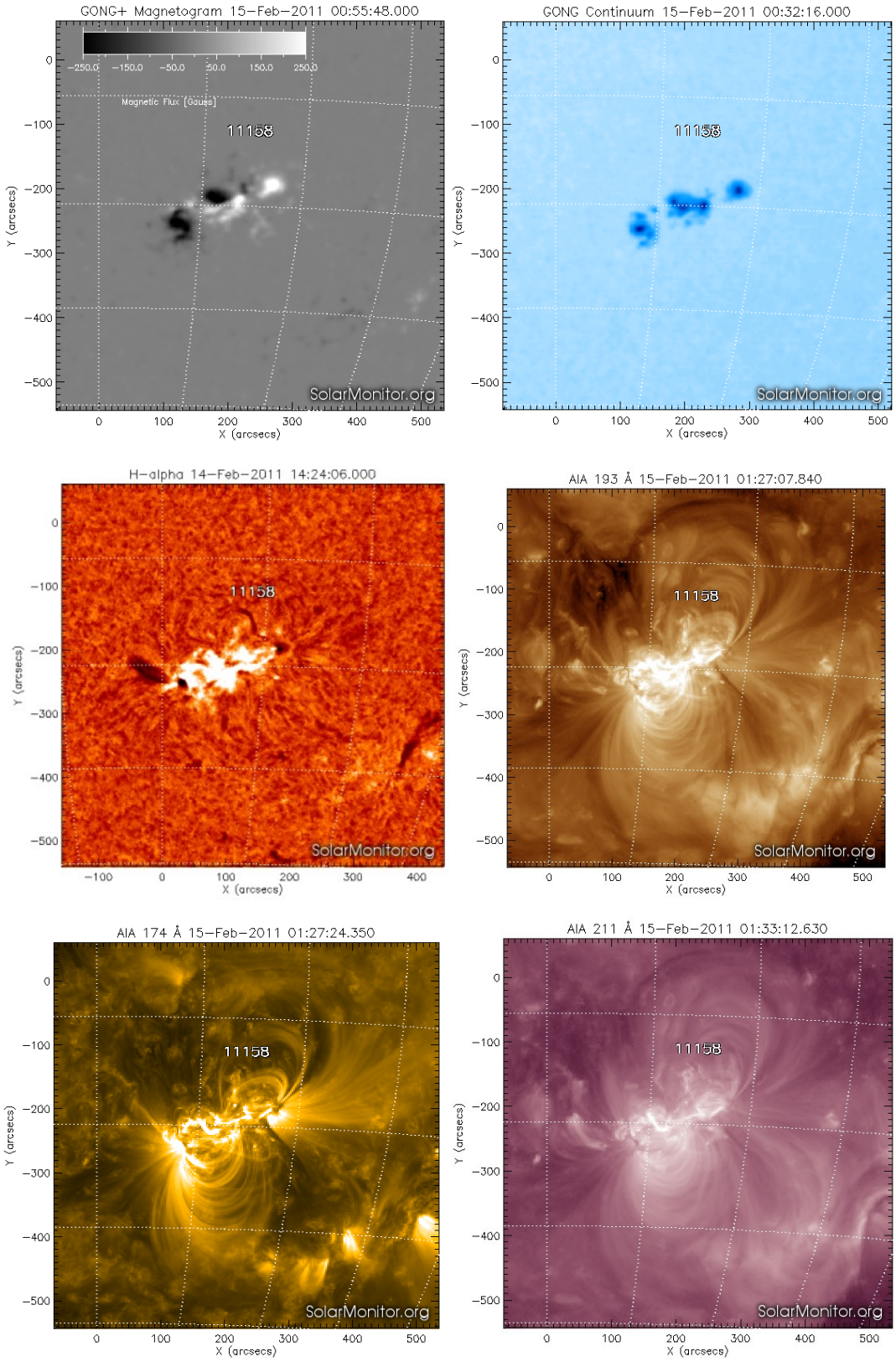

Figure 62. From left to right: MDI magnetogram; MDI WL photospheric image; Hα chromospheric image; AIA 193 Å coronal image, AIA 174 Å coronal image; AIA 211 Å coronal image;

- Magnetic Configuration

To analyze the magnetic configuration of NOAA 11158 we used MDI/SOHO line of-sight magnetograms acquired between 00:03 UT to 22:23 UT on 15 February 2011.

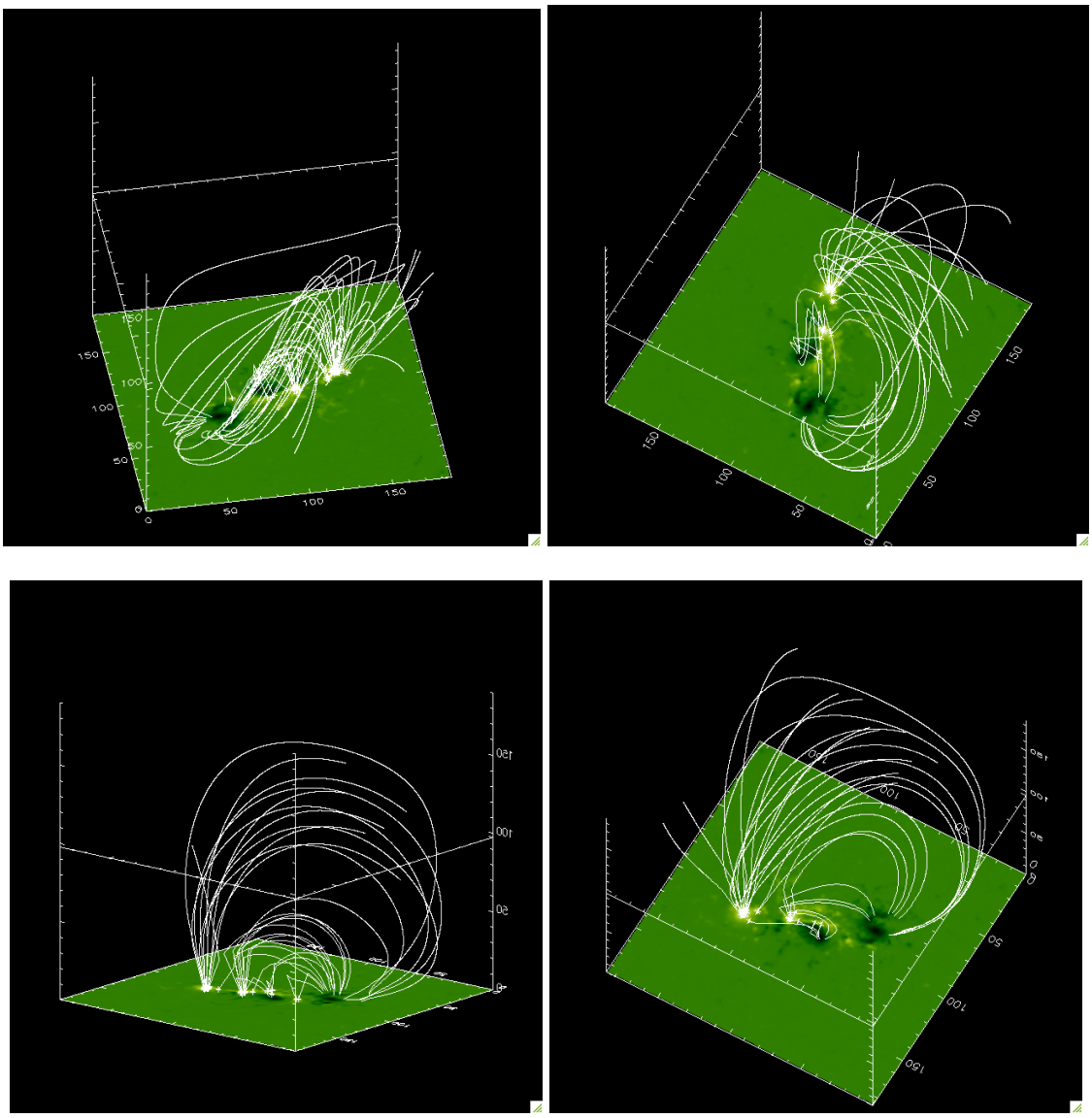

Figure 63. Force-free field extrapolation performed using the MDI magnetogram acquired on 15 February 2011 at 01:36 UT for AR NOAA 11158. Each figure shows the active region magnetic configuration from the photosphere to the corona from different view angles, in order to evidence the different field lines connectivity.

Figure 63 shows the results obtained from the force-free field extrapolation performed on the MDI magnetogram acquired at 01:36 UT (before the flare occurrence), using the value 0.02 for the α force free parameter. In this case the extrapolations shows a lower degree of complexity of the active region, as compared with the previous AR analyzed.

However, even if the magnetic configuration appears to be less complex, the presence of several sunspots in the active region, each characterized by high values of the magnetic field, and the high degree of shearing indicated by the inclined field lines, are indicative of a magnetic configuration where a considerable amount of magnetic energy has been stored. This situation can easily end-up in an unstable situation leading to explosive events. Also in this case the field line configuration is quite similar to the loop systems observed in the AIA 174 and 193 Å images (compare the left top figure with Figure 62).

- *The CME evolution*

On 15 February 2011 the separation angle between STEREO A and B satellites was 179.1 degrees (Figure 64).

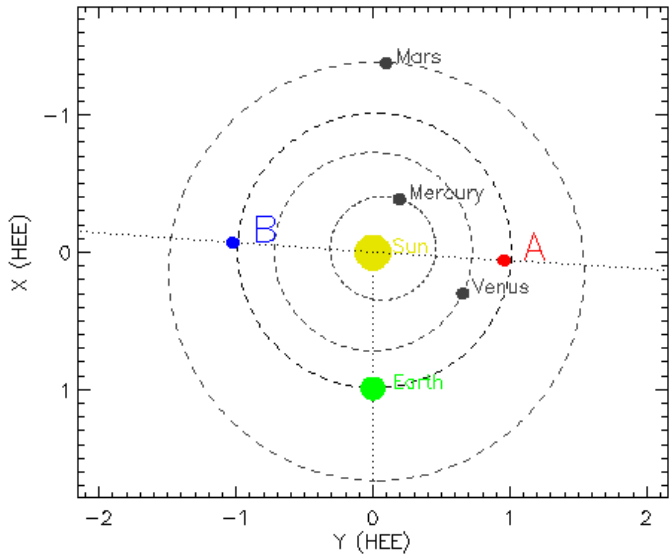

Figure 64. Graphic with the position of the twin STEREO satellites respect to the Sun and Earth on February 15, 2011 (NASA).

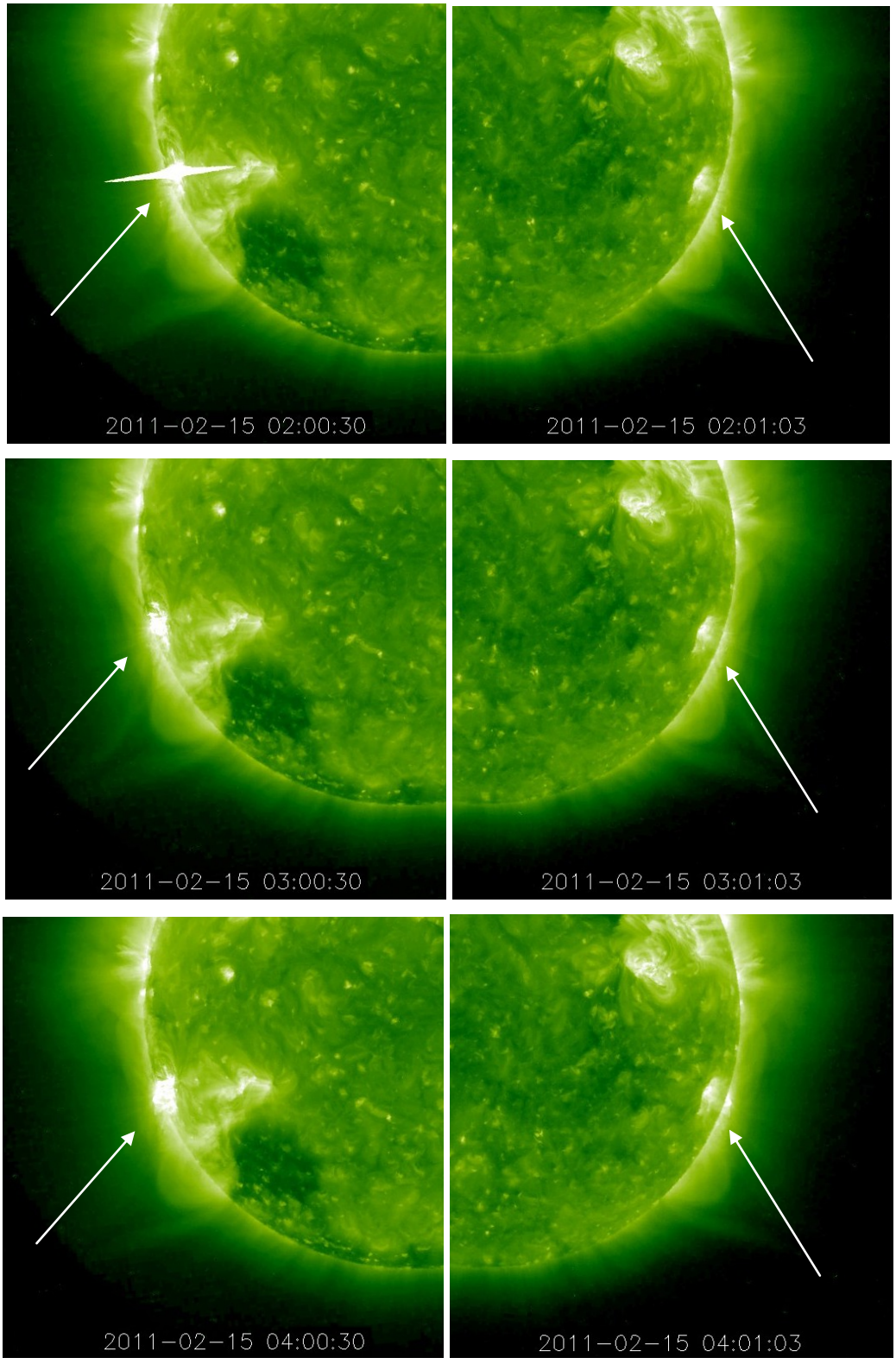

Figure 65. STEREO-EUVI A (left column) and B (right column) 195 Å zoomed images of NOAA 11158 acquired at three different times. Images showing the evolution of the eruptive event in the corona at 1.5 MK. The AR location is indicated by an arrow in each image.

Figure 65 shows the evolution of the flare occurred in AR NOAA 11158, as observed by EUVI A and B. In the images acquired by EUVI-A we can see the formation and brightness increase of the post-flare loops. These features however are not clearly visible in the EUVI-B images.

Figure 66 shows the CME evolution at four different times (steps of 10 minutes starting from 02:20 UT), as observed by COR1 A and B, respectively. The CME is seen at the east limb of the Sun from STEREO A and at the west limb from STEREO B. The front-edge began to rise around 02:00 UT or earlier on February 7.

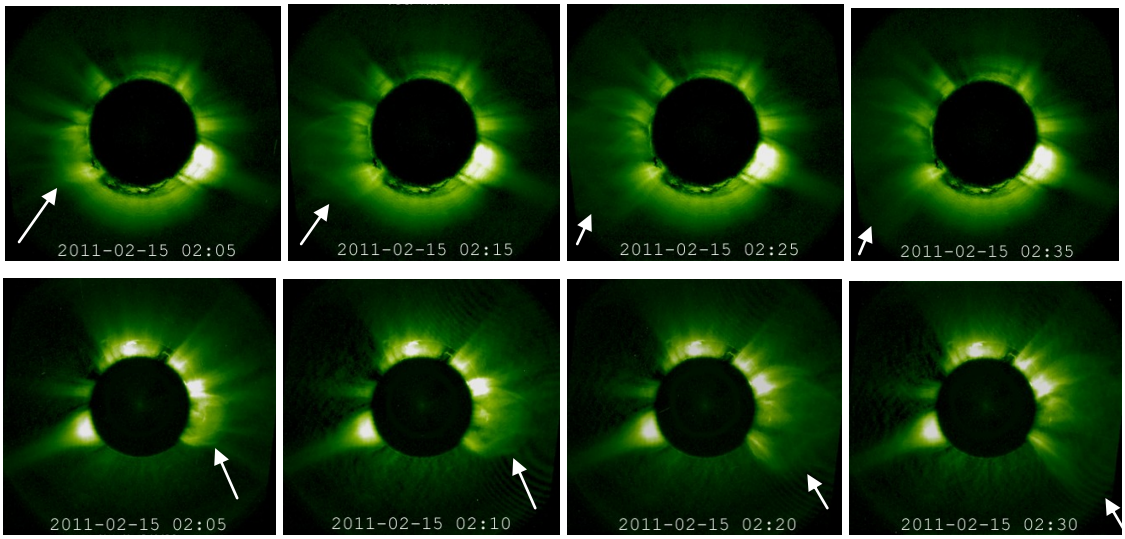

Figure 66. STEREO-COR1A (up) and COR1B (down) images showing the CME evolution at four different times. The CME location is indicated by an arrow in each image.

Also in this third event the CME rises as a typical three-part structure. In fact we can see a very bright loop, superimposed on a dark cavity enclosing plasma. Moreover, also in this case, the most external bright loop seems to be anchored in both northern and southern hemisphere. The CME bright edge quickly expands with these two ends still connected to the Sun (see also Figure 67).

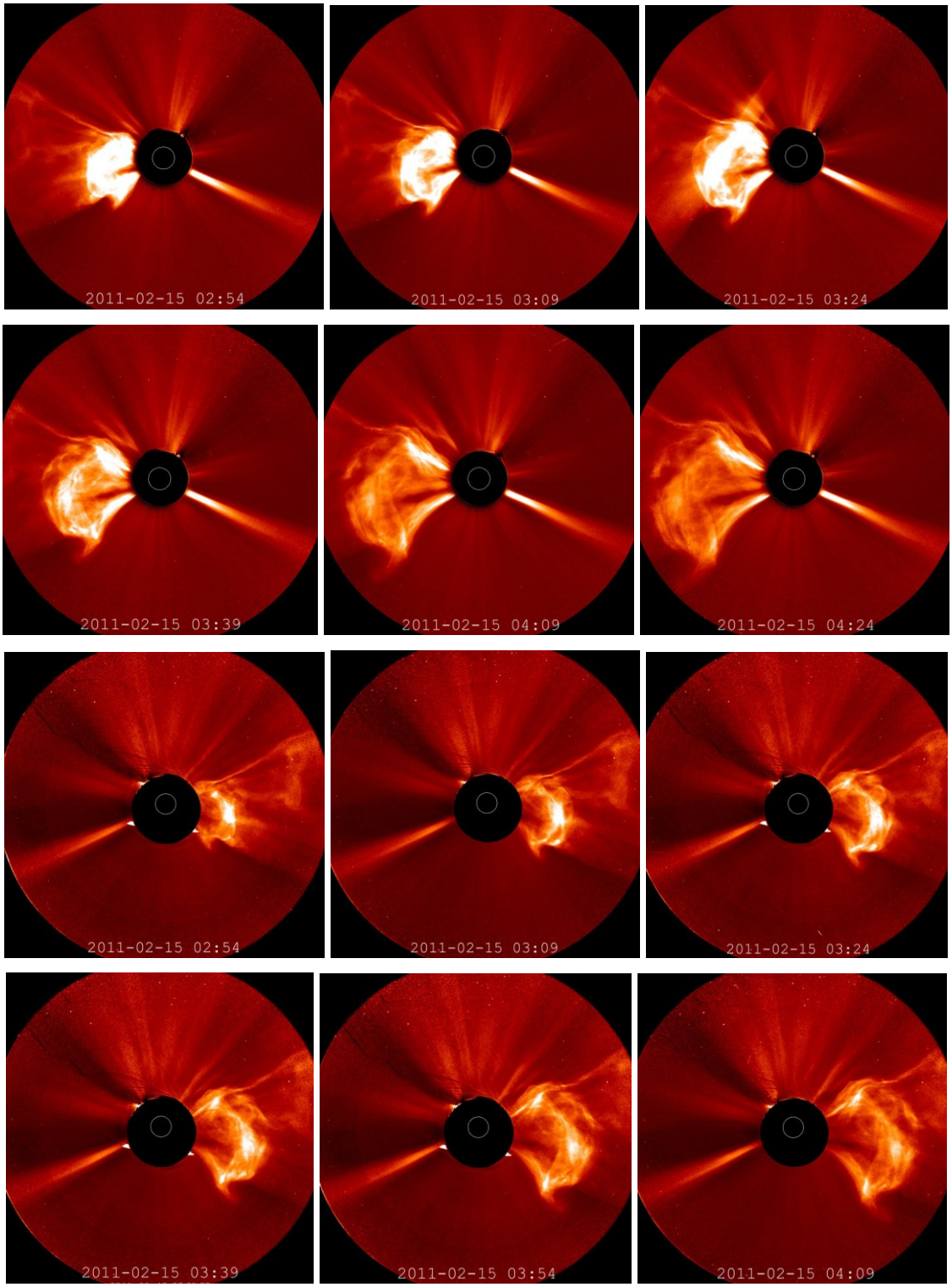

Figure 67. STEREO-COR2A (six panel up) and COR2B (six panel down) images showing the CME evolution at six different times.

Figure 67 shows the CME as observed by COR2 from 02:54 UT until 04:09 UT. The CME rises as a typical three-part structure also in COR2, and it is very bright in both coronograph. Moreover, as in the previous CME, the ejected plasma extends on a wide latitudinal range, both in the northern and southern hemispheres.

To have a comparison with other spacecraft data we show in the Figures 68 and 69 images of the CME observed on February 15, 2011 from LASCO C2 and C3 onboard SOHO satellite. As we can see the halo CME is observed during its expansion.

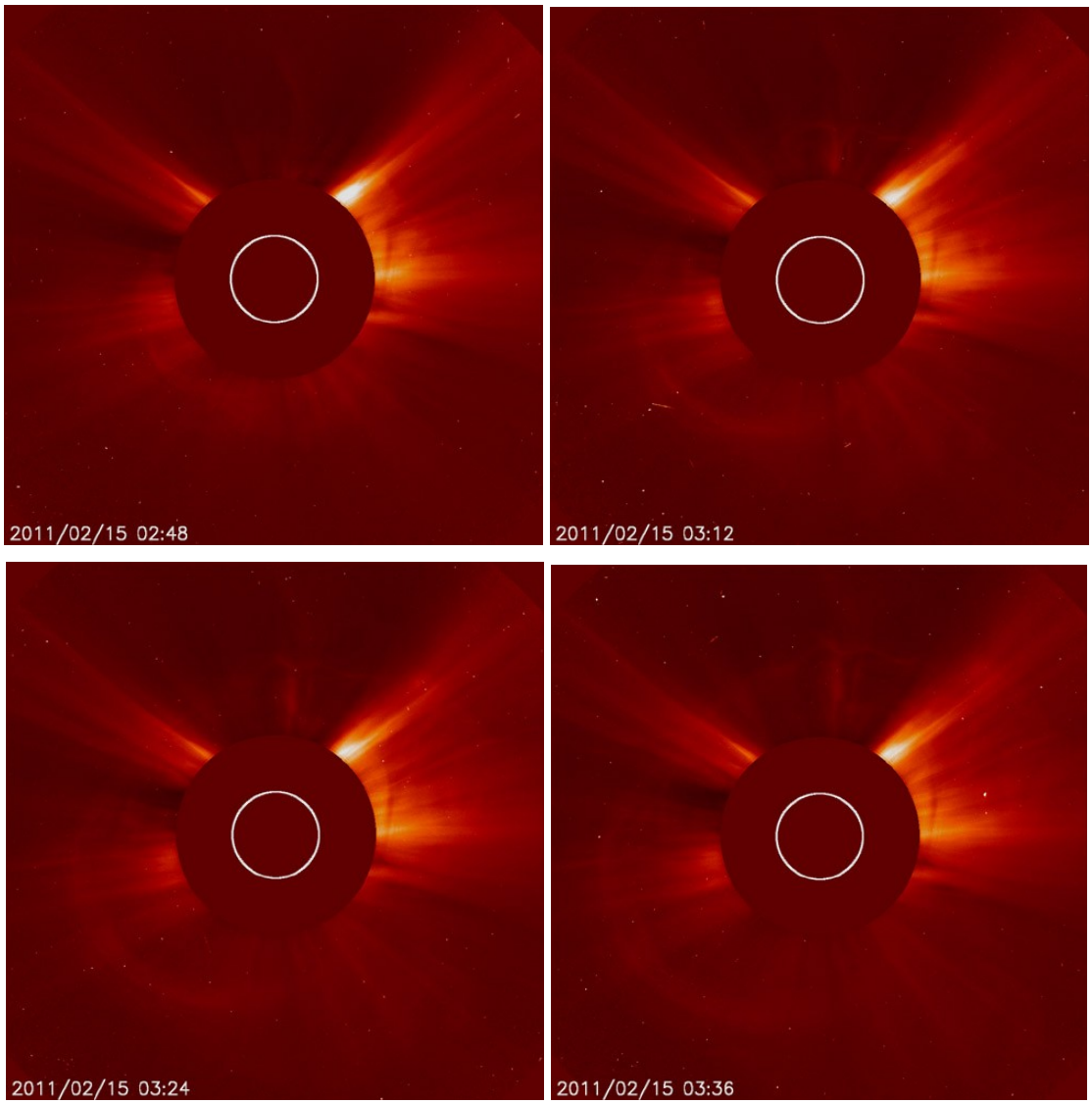

Figure 68. SOHO-LASCO C2 images showing the CME evolution at four different times.

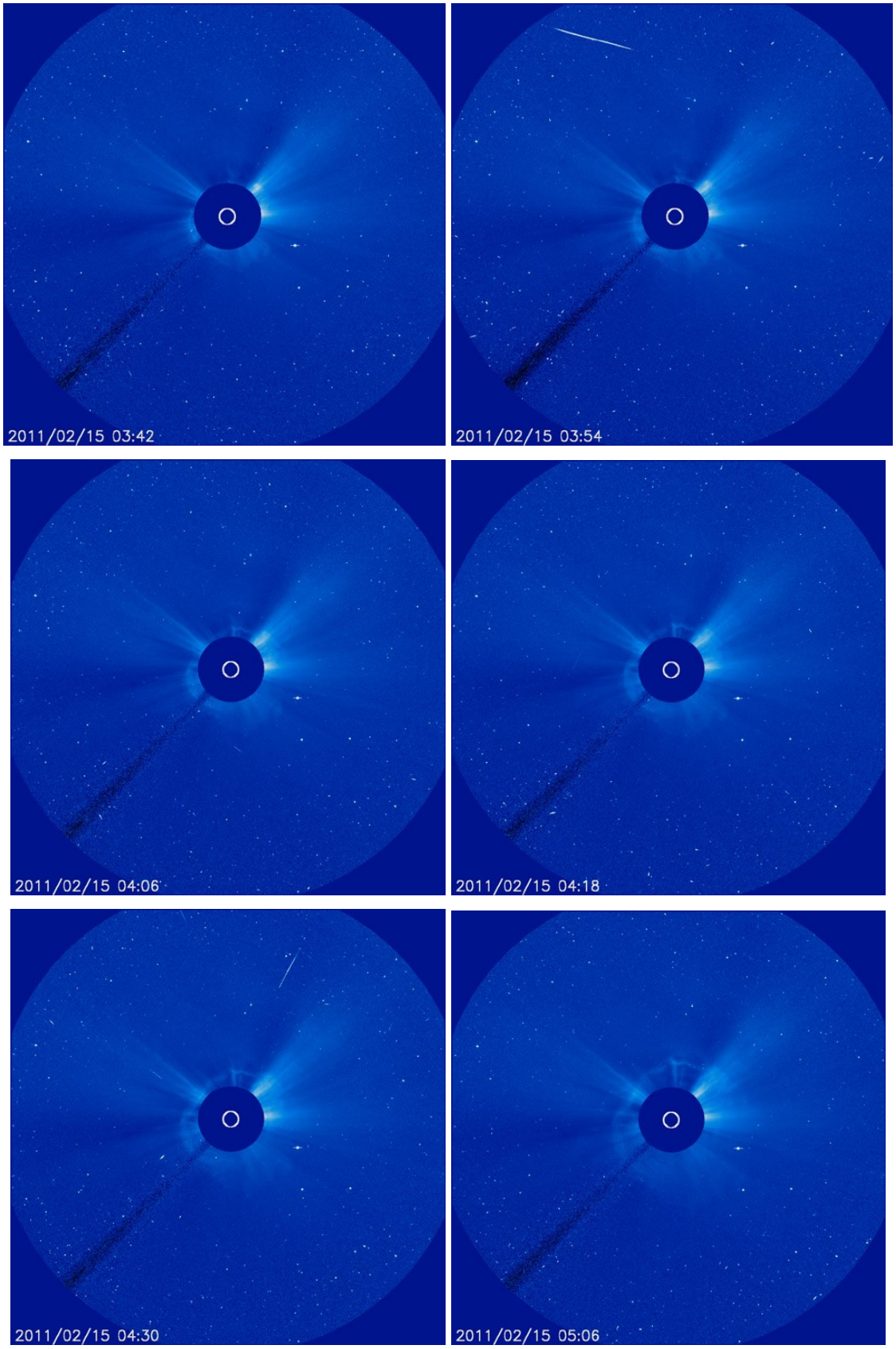

Figure 69. SOHO-LASCO C3 images showing the CME evolution at six different times.

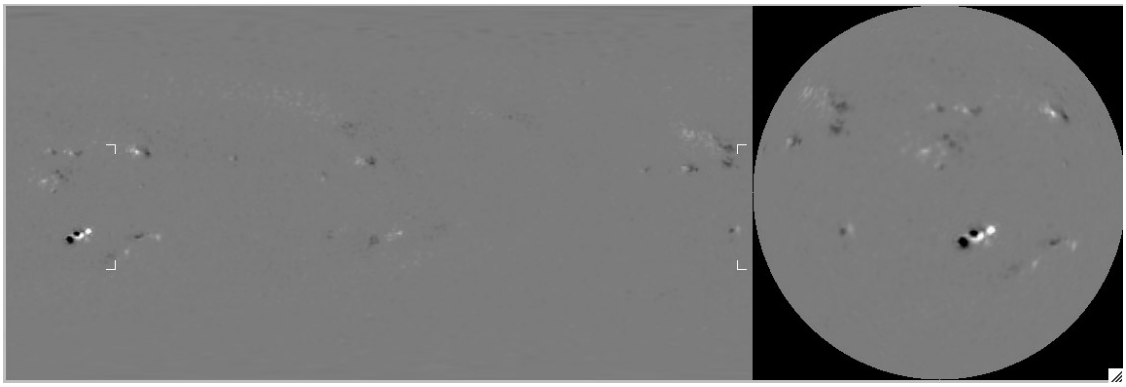

Figure 70. Left: MDI image of the radial component of the photospheric magnetic field in a rectangular latitude-longitude (Carrington) projection. The corners indicate the field of view including the active region of interest. Right: MDI full disk magnetogram acquired on 15 February 2011.

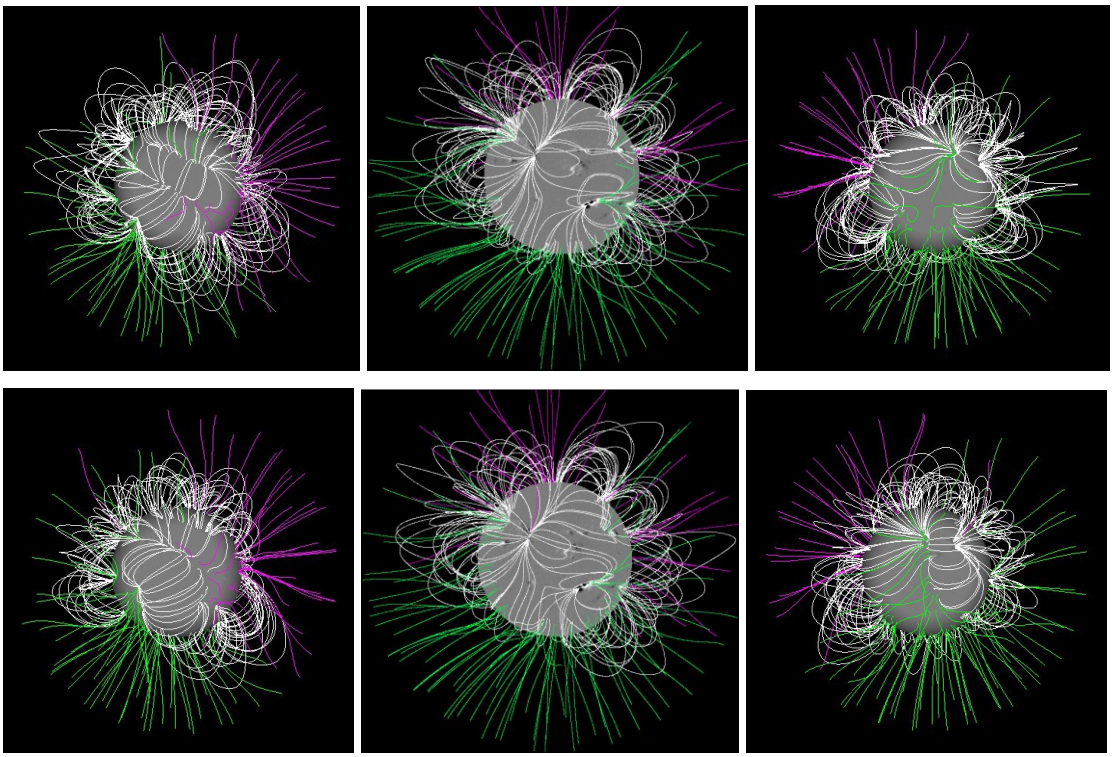

Figure 71. Results obtained from the PFSS, showing the global magnetic field configuration of the full Sun. Top panel: results obtained from the magnetogram acquired at 00:04 UT on 15 February (before the event) from a STEREO A view (left), Earth view (center) and STEREO B view (right). The active region of interest is at the center of the solar disk. Bottom panel: extrapolations relevant to the magnetogram acquired at 06:04 UT on 15 February (after the event).

In Figure 70 we show the initial MDI magnetogram while, from the PFSS procedure, used to infer how the global magnetic field appears from the three different

point of views (Earth, STEREO A and STEREO B), we can see (Figure 71) that also in this case the bright leading edge of the CME observed in STEREO A and B images does not clearly correspond to the systems of magnetic field lines inferred by the force-free field extrapolation (in the STEREO data the leading edge seems to be initially connected to both hemispheres).

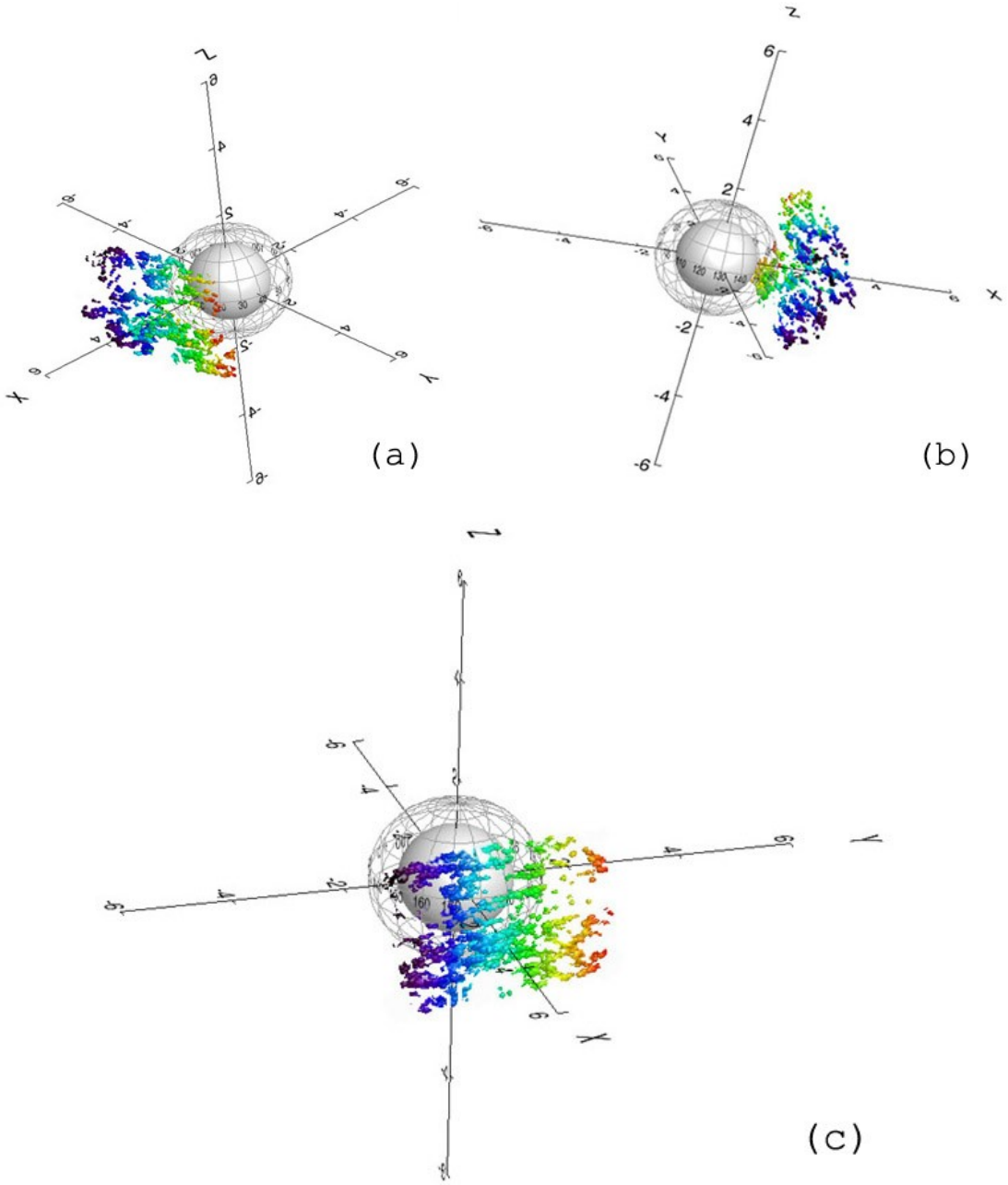

Figure 72. (a) CME 3D reconstruction from STEREO A view point at 02:20 UT, as seen edge-on; (b) CME 3D reconstruction as seen by STEREO B; (c) CME 3D reconstruction as seen by the Earth.

Figure 72(a) shows the 3D reconstruction from A view point at 02:20 UT, as seen edge-on (compare with Figure 66, relevant to COR1A at 02:00 UT); Figure 72(b) reports the reconstruction edge-on at the same time by STEREO B (compare with Figure 66 acquired by COR1B at 02:00 UT); Figure 72(c) reports the CME 3D reconstruction as seen by the Earth.

The Figure 73 shows in the left plot the increase of the leading edge of the CME; we can see that it is almost linear. The linear speed inferred from this data is about 670 km/s, while from the second order fit the speed is initially about 800 km/s and then decreases to about 570 km/s; the CME acceleration inferred from this data is ~ -18.26 m/s^2.

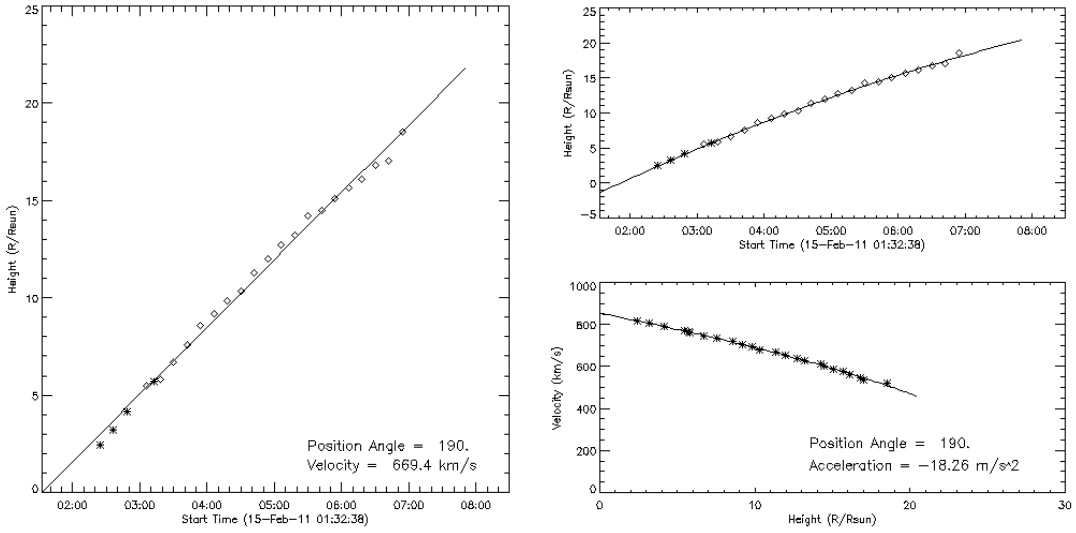

Figure 73. Linear fit (left) and 2nd order fit (right) plots. Radial distance and speed of the CME leading edge derived from the LASCO catalogue (CDAW/NASA).

CHAPTER 5. *COSMIC RAYS AND SPACE WEATHER*

5.1 Cosmic Rays

Cosmic Rays are energetic charged subatomic particles, originating from outer space. About 89% of cosmic rays are simple protons or hydrogen nuclei, 10% are helium nuclei or alpha particles, and 1% are the nuclei of heavier elements. The variety of particle energies reflects the wide variety of sources (Figure 74). The origins of these particles range from processes on the Sun (and presumably other stars as well), to as yet unknown physical mechanisms in the farthest reaches of the observable universe.

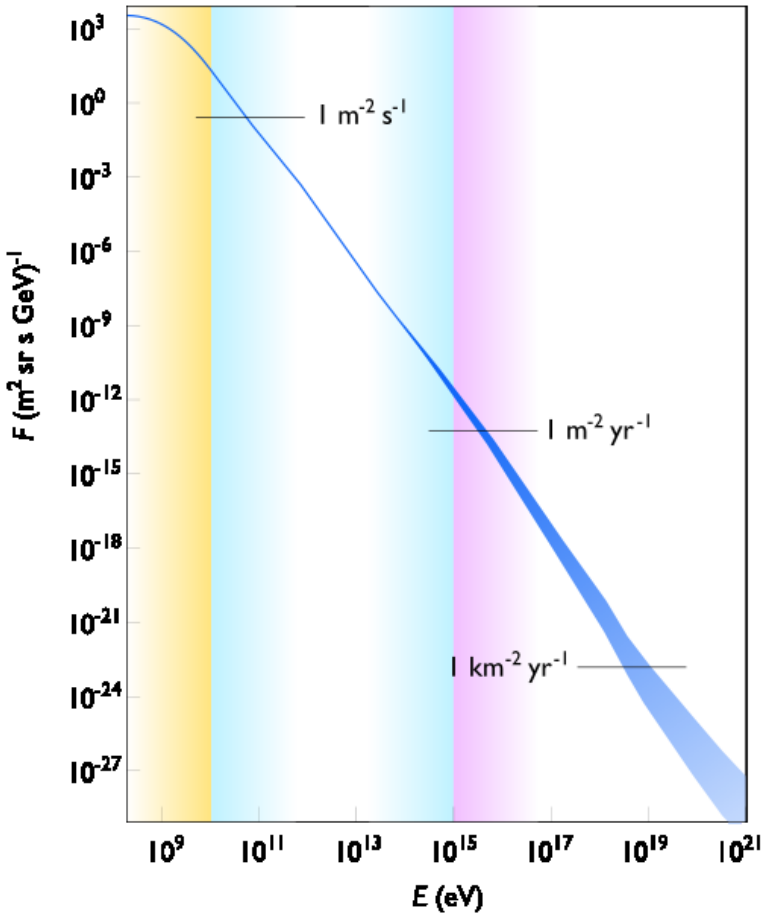

Figure 74. The energy spectrum of Cosmic Rays (CR).

When cosmic rays enter the Earth's atmosphere they collide with molecules, mainly oxygen and nitrogen, to produce a cascade of billions of lighter particles, a so-called

air shower (Figure 75). An air shower is an extensive (many km wide) cascade of ionized particles and electromagnetic radiation produced in the atmosphere when a primary cosmic ray (i.e. one of extraterrestrial origin) enters the atmosphere. The term *cascade* means that the incident particle, which could be a proton, a nucleus, an electron, a photon, or (rarely) a positron, strikes a molecule in the air so as to produce many high energy ions (secondaries), which in turn create more, and so on.

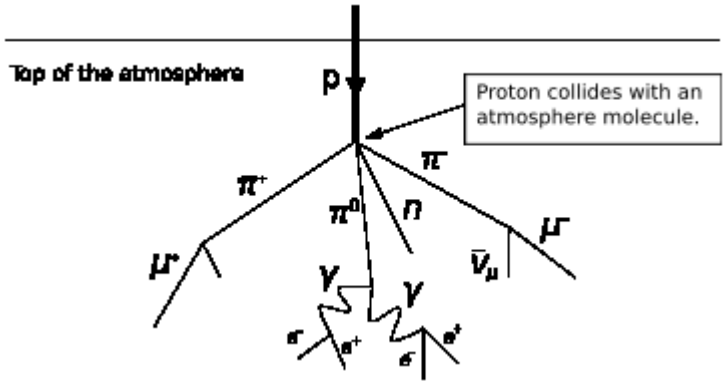

Figure 75. A sketch showing the air shower, a cascade with charged particles as pions and kaons.

All of the produced particles stay within about one degree of the primary particle's path. Typical particles produced in such collisions are charged mesons e.g. positive and negative pions and kaons. These subsequently decay into muons that are easily detected by many types of particle detectors.

Cosmic-rays (CR) effects are related to Space Weather in two ways: (a) intensity increases caused by the acceleration of particles in solar flares and/or in the interplanetary space lead to direct changes in materials exposed to the particle radiation both in space and on the surface of the Earth, and (b) CRs detected by the network of neutron monitors (NMs) reveal the anisotropies relevant for Space Weather research.

CRs detected by NMs (kinetic energies of protons above 500 MeV) have sufficiently large Larmor radii[12] in the interplanetary magnetic field (IMF, units of nT) such that they are affected by large scale IMF inhomogeneities originated at the Sun well before the disturbances reach the Earth's orbit (geo-effective event) and geomagnetic disturbances occur. Thus, intuitively, CR anisotropies may serve as a tool for remote sensing of the magnetic field changes in the heliosphere. CR activity indices seem to be useful parameters for short-term alert systems prior to major geomagnetic storms. Most of the important Space Weather effects are related to geomagnetic storms.

A *storm period* is defined as a time interval during which a sufficiently intense and long-lasting interplanetary convection electric field leads, through a substantial energization in the magnetosphere-ionosphere system, to an intensified ring current, strong enough to exceed some key threshold of the quantifying storm time Dst index[13] [Gonzalez et al., 1994, 1999; Russell and McPherron, 1973].

The heliospheric modulation of Galactic Cosmic Rays (GCRs) observed near Earth is controlled by the solar activity. In particular, it is influenced by the variability of solar wind (SW) conditions, due to the solar cycle modulation and to transient eruptions of solar ejecta (i.e., CMEs). The observed modulation of cosmic rays (CRs) intensity provides information about the transport of particles in the inner and outer heliosphere, and also about particles coming into the solar system from the Local Interstellar medium. GCRs intensity observed near Earth have shown a long-term modulation (associated with the solar cycle) and short-term variations, such as *Forbush decreases*.

5.2 Forbush Decrease

A Forbush decrease (Fd) [Forbush, 1937] is a rapid decrease in the observed galactic cosmic ray intensity observed at Earth, following a coronal mass ejection. It occurs

[12] The gyroradius (also known as radius of gyration, Larmor radius or cyclotron radius) is the radius of the circular orbit of a charged particle in the presence of a uniform magnetic field.
[13] The *disturbance storm time* (Dst) index is a measure, in the context of space weather, which gives information about the strength of the ring current around Earth caused by solar protons and electrons.

due to the magnetic field of the plasma solar wind (or CME) sweeping some of the galactic cosmic rays away from Earth.

As observed in neutron monitors (NMs) and muon detectors, the structure of Forbush decreases is asymmetrical, starting suddenly and recovering smoothly with typical recovery times of the order of several days.

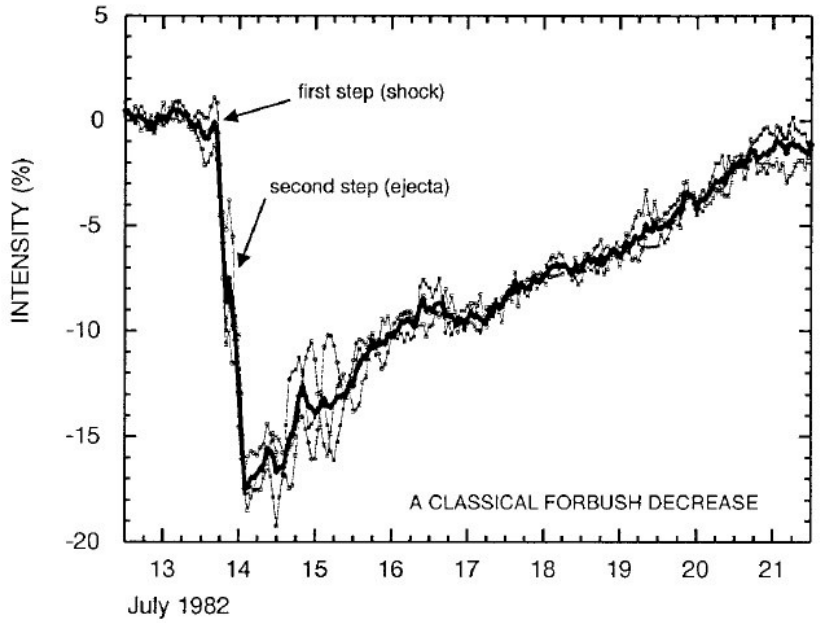

Figure 76. Percentage decrease for three neutron monitor stations spaced about equally in longitude (Deep River, Mt.Wellington, Kerguelen) (from Cane, 2000).

Figure 76 shows an example of a Forbush decrease. In this figure a measure of the isotropic intensity (shown by the thick line) is obtained by averaging the count rate measured by three neutron monitors (Deep River, Kerguelen and Mt. Wellington) with similar responses and spaced approximately equally in longitude. The rates from the individual monitors are shown (using thin lines) in order to illustrate the variability which occurs between stations. The presence of two steps is indicated. The first decrease occurs in the turbulent field region that is generated behind the shock which this fast ejecta creates in the medium ahead of it. A reduction in the cosmic ray density also occurs inside the ejecta because of its closed field line geometry.

Figure 77 illustrates the large scale structure of an ejecta and associated shock and how the cosmic ray response is related to the path through the ensemble.

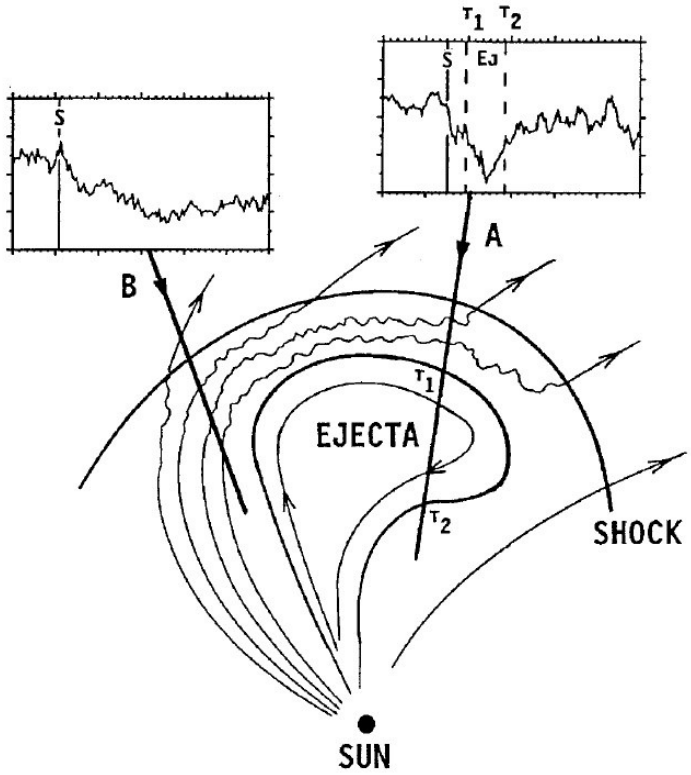

Figure 77. The large-scale structure of a fast ejecta and associated shock. The upstream solar wind is draped around the ejecta and heated and compressed at the front of the ejecta. Two paths through the ensemble are indicated with differing resultant cosmic ray profiles. The time of shock passage is indicated by a vertical line marked S and the start and end times of ejecta passage are marked T1 and T2. Only if the ejecta is intercepted is a two-step decrease be observed (from Cane, 2000).

If an observer is passed by a shock and its associated ejecta, two-steps are seen as shown for path *A*. A less energetic ejecta which does not create a shock causes only a short-duration one component/step decrease as the ejecta passes by. Such events are often too small to produce a significant decrease in the records of a single neutron monitor. Since shocks have a greater longitudinal extent than ejecta, it is possible to intercept the shock but not the ejecta as shown by path *B*. In this case, only the effect due to the shock is evident. Note that the ejecta pushes aside the upstream solar wind, compressing and heating it and that the field lines get draped around the ejecta. This leads to an asymmetrical structure which is responsible for the long established asymmetry in the sizes and presence of Fds as a function of longitude of the associated solar event [Haurwitz et al., 1965].

Only very energetic CMEs create shocks which are strong enough on their flanks to cause significant cosmic ray decreases for observers who detect the shocks beyond the azimuthal extent of the 'driver' CMEs. In such cases the shocks also generate major solar energetic particle increases with profiles characteristic of events originating far from central meridian [Cane et al., 1988]. The energetic particles allow one to be sure that the cosmic ray decrease was caused by a CME-driven shock intercepted on its flank and not by a co-rotating stream.

5.3 Auger Observatory

Dedicated neutron monitors are being used since several decades ago as ground observatories to measure variations of CRs intensities. More recently, many ground based CR detectors aiming at CR physics at higher energies are also being used for these studies. It is the case of Pierre Auger Observatory.

The Pierre Auger Observatory was designed to study the physics of cosmic rays at the highest energies. Detection of cosmic rays of energies above 10^{18} eV requires the instrumentation of a huge detection area, due to the extremely low flux of particles at these extreme energies. The Auger Observatory combines two detection techniques in a hybrid design: the observation of the fluorescence light produced by the secondary particles as they propagate through the atmosphere, and the direct measurement of particles reaching ground level.

In Figure 78 we show the layout of the Pierre Auger Observatory located in Malargüe, Argentina, at 1400 m a.s.l.. The position of the four Fluorescence Detector (FD) buildings surrounding the Surface Detector (SD) array are indicated by the black squares, with gray lines indicating the field of view of the six telescopes at each building. Orange dots mark the position of each of the 1600 water-Cherenkov detectors[14], with a 1.5 km spacing between nearest neighbours.

[14] Each water-Cherenkov detector consists of a polyethylene tank (10m^2 area) containing 12 tonnes of high-purity water in a highly-reflective Tyvek® liner bag, providing a total of about 16000 m^2 of collection area for the full SD array.

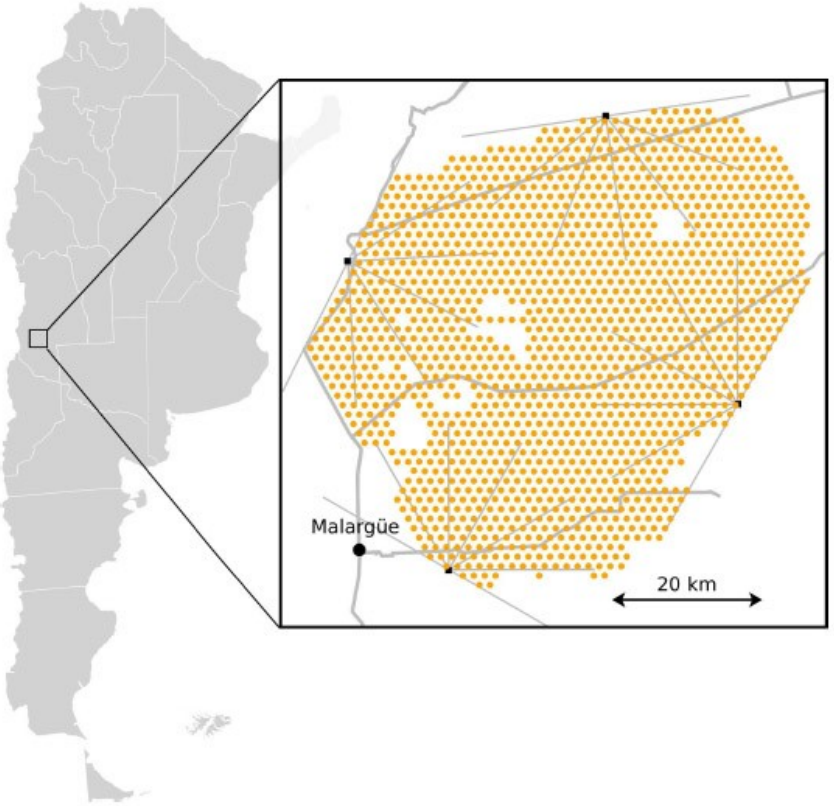

Figure 78. Layout of the Pierre Auger Observatory at Malargüe, Argentina.

The interaction of a high-energy particle with the atmosphere produces a cascade with a huge number of secondary particles called an Extensive Atmospheric Shower (EAS). The longitudinal development of the EAS is followed by the FD consisting of 24 telescopes grouped in units of six telescopes at four different locations (Los Leones, Coihueco, Loma Amarilla and Los Morados). FD operates only in moonless and clear-weather nights, with an operational average duty cycle of 13% of the total time. It overlooks the atmosphere above a 3000 km^2 area, where the SD is deployed.

The SD is an array of more than 1600 water-Cherenkov detectors placed in a triangular grid with a spacing of 1500 m. The lateral (transverse) distribution of secondary particles of EAS at ground level is sampled by using the SD array [Pierre Auger collaboration, 2011].

5.4 CMEs and Forbush Decrease

We want to investigate the link between the analyzed coronal mass ejections and cosmic rays. The flow of coronal material ejected into interplanetary space takes about 2 to 4 days to reach Earth, and it is known that its impact with the magnetosphere can cause major geomagnetic disturbances and auroras at low latitudes. A good tracer to identify a CME at Earth is given by the decreases in the cosmic ray flux (Forbush decreases).

We have considered the three CMEs analyzed in the previous chapter and the cosmic ray flux. The data on cosmic rays were provided by the neutron monitor stations (McMurdo, Athens, Rome, Moscow and Oulu) and Pierre Auger Observatory.

In Figure 79 we show the Forbush decrease linked to the CME event of April 3, 2010. More precisely, the plot to the left shows the cosmic ray flux for 500 days, starting from 01/01/2010, while in the plot to the right the flux is reported only for 50 days, centered on 03/04/2010. In this plot the gray vertical line indicates the time at which the CME occurred, while the red arrow points to the Forbush decrease. The rate of cosmic rays observed from neutron monitor station in McMurdo (green) and from Auger Observatory (red) are shown. The plots show the flux renormalized to compare the 2 stations in a simple way, so we have arbitrary units in Y-axis as a function of time (in Julian Days from January 1, 2010).

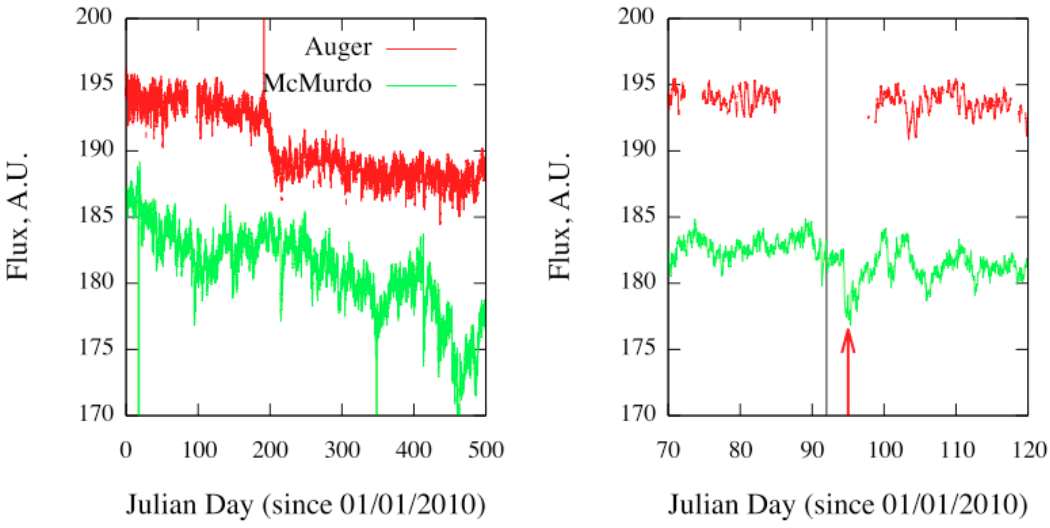

Figure 79. Forbush decrease linked to the CME of April 3, 2010 (courtesy of M. De Domenico/INFN).

We can see, in the plot to the right that the Fd is observed from the neutron monitor station in McMurdo but not by Auger Observatory. In the plot it is evident that the Forbush decrease occurs 3 days after the date of the CME event (92 ° day in Julian Days, gray vertical line).

In Figure 80 we show the Forbush decrease for the CME events of August 2010 (upper panel) and February 2011 (bottom panel) respectively. In the plots of Figure 80 the yellow vertical lines indicate the time of CME occurrence. The curves represent the rate of cosmic rays observed from stations in Athens, Moscow, Oulu and Rome. We have also added the rate measured by Auger Observatory.

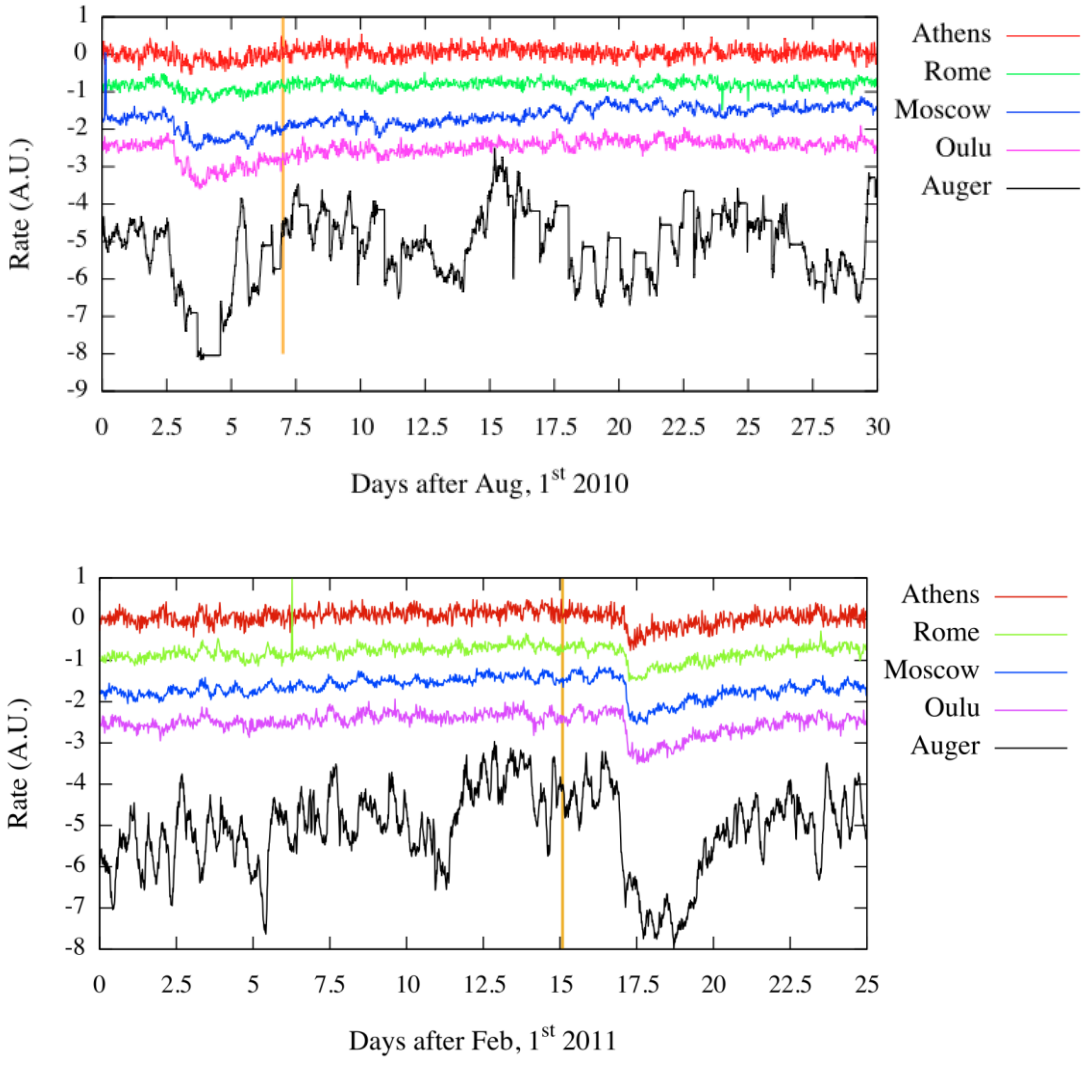

Figure 80. Forbush decrease linked to CMEs event studied. The resolution of Auger used in these plots is 15 minutes, while other stations use 30 min (courtesy of M. De Domenico/INFN).

In all cases the rate is adjusted for pressure and temperature, so it is the real rate. In the case of Auger, numbers represent a rate per m^2.

Furthermore, in order to compare all the data, we have first renormalized due to zero mean and variance 1 (in this way become all overlapping) and then shifted to a certain factor along the vertical, so not all of them are overlapping. This is necessary because the rate depends on altitude and atmospheric conditions, so an observatory in the mountains will see more or less than a stream of particles at the north pole, and so on.

In Figure 80, upper panel relevant to the CME occurred on 7 August, the Fd is not clearly observed, either from the neutron monitor station or from Auger Observatory, while it is evident another Fd, linked to the CME halo occurred at the beginning of August. In the bottom panel, relevant to the CME occurred on 15 February, there is an evident decrease in cosmic ray flux, due to the arrival of interplanetary disturbances. In this case, the Fd is observed by Auger Observatory also.

Moreover, while the April 2010 CME takes about 3 days before reaching Earth, the CME of February 2011 takes only 2.5 days. This might be due to the fact that the CME of February 2011 is linked to an X-class flare, while the CME of April 2010 is linked to a B-class flare.

5.5 CME and Space Weather

To investigate the Sun-Earth connection during and after the analyzed events, we have taken into account the WIND satellite data, and in particular the interplanetary magnetic field (IMF) parameters (see Figures 81, 82 and 83). In these plots the orange vertical line indicates the time at which the CME occurred, while the red lines delimit the time interval in which we observe changes in IMF parameters.

In two cases we can see a sudden change in the solar wind parameters (B_x, B_y, B_z, **B**). In the plots of Figure 83, linked to CME of February 15 2011, we notice a sudden and sharp increase of the three components of the IMF, and this highlight the arrival of interplanetary disturbances.

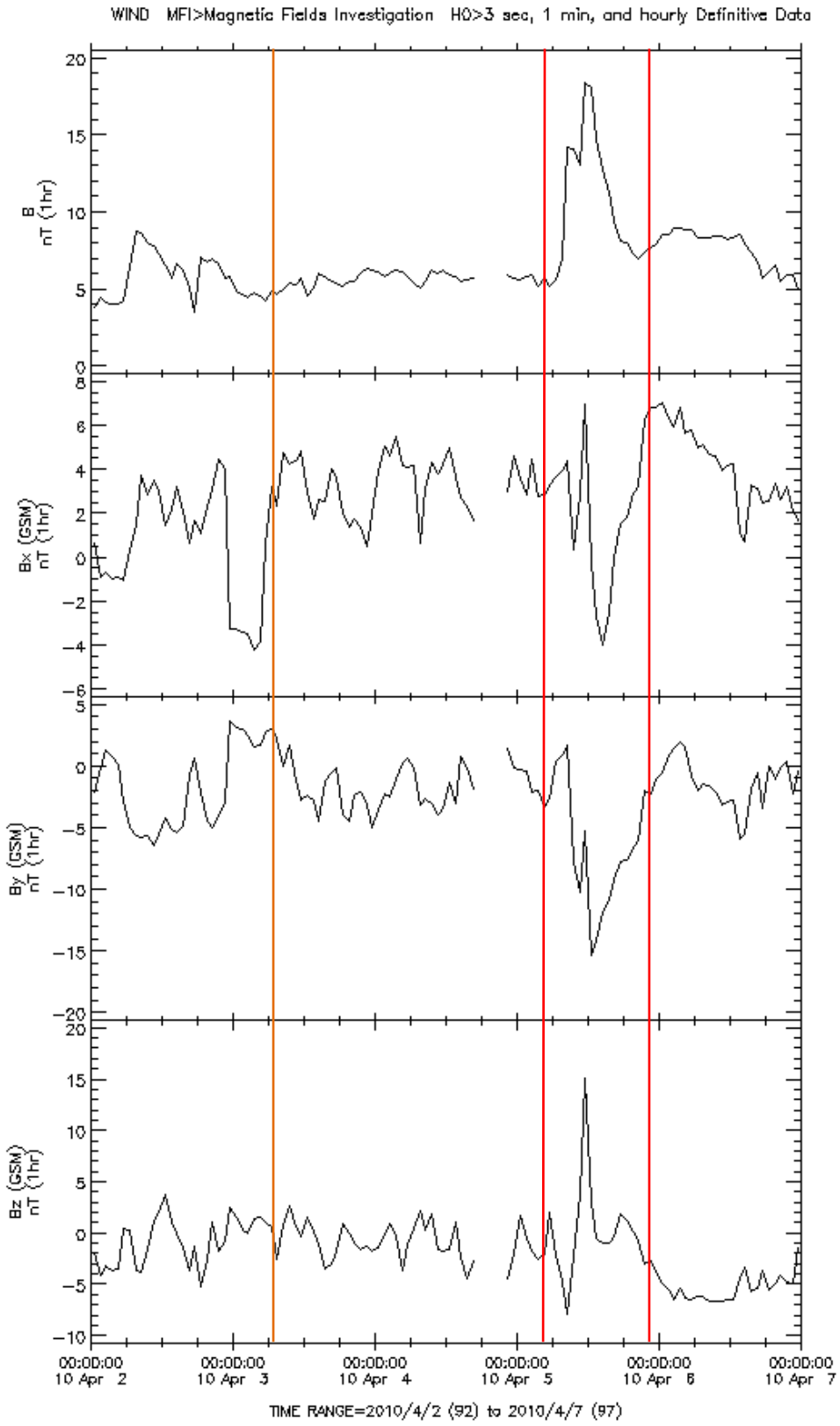

Figure 81. Interplanetary magnetic field (IMF) components of solar wind during the CME event of April 2010 (WIND data, NASA/GSFC).

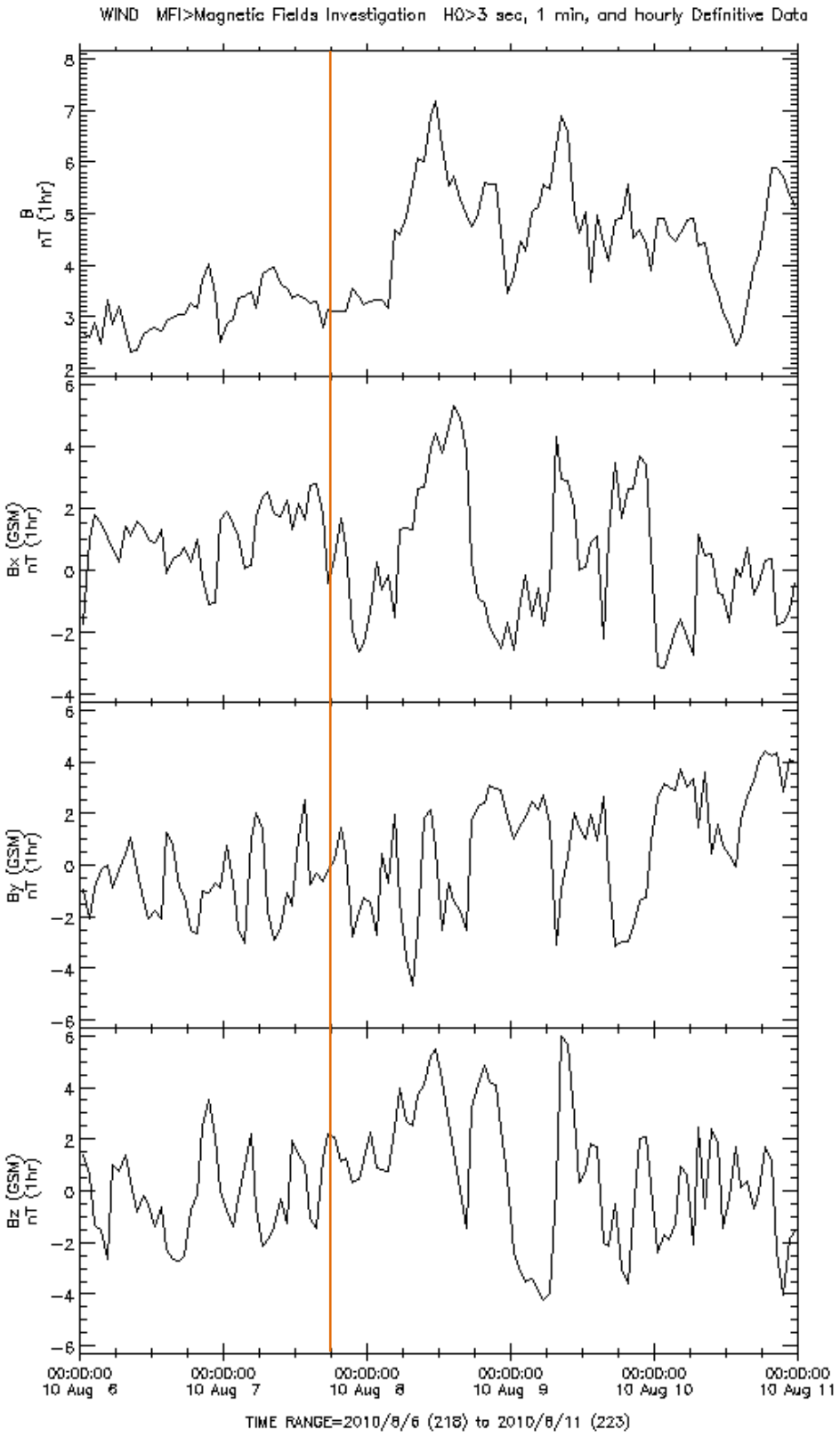

Figure 82. Interplanetary magnetic field (IMF) components of solar wind during the CME event of August 2010 (WIND data, NASA/GSFC).

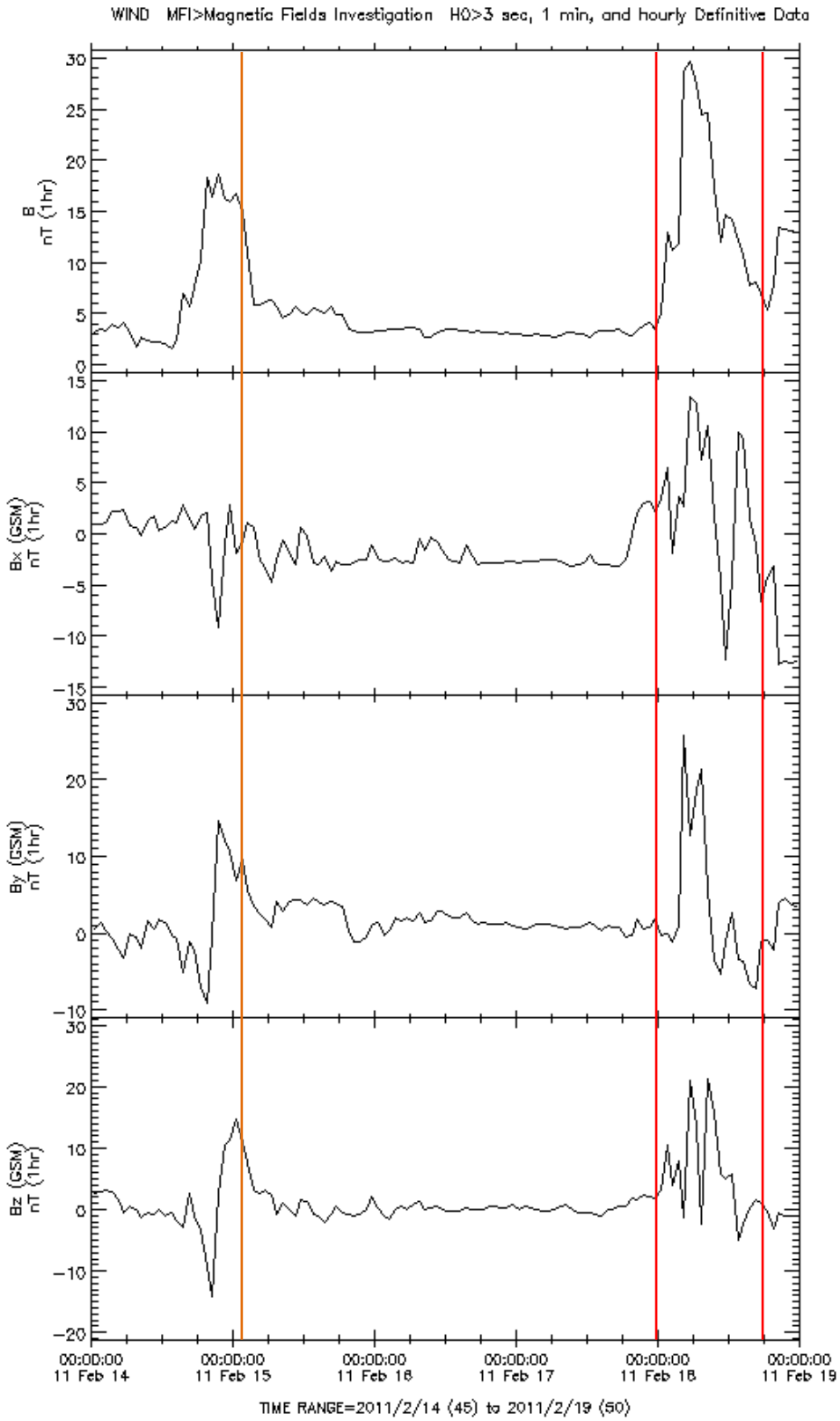

Figure 83. Interplanetary magnetic field (IMF) components of solar wind during the CME event of February 2011 (WIND data, NASA/GSFC).

Geomagnetic storms can produce severe damages to satellites. A southward magnetic field can reconnect with geomagnetic fields and thus is a key factor in producing geomagnetic storms. The Dst index, a measure of the severity of geomagnetic storms (the more negative, the more intense), has a minimum value of about −72 nT for the geomagnetic storm of April 5, 2010. The storm caused a communication failure with the Galaxy 15 satellite at 09:48 UT on April 5, 2010, soon after the arrival of the shock at L1 (07:55 UT). Although moderate, the geomagnetic storm caused a breakdown of the Galaxy 15 satellite for more than half a year. Also note a strong southward magnetic field component in the sheath region right behind the shock (Figure 81, bottom panel). This short interval accounts for the beginning of the geomagnetic storm. The geomagnetic storms are strictly connected to the *magnetic reconnection*.

The magnetic reconnection is one of the most important processes that characterize the physical interaction between plasma and magnetic field, and is a process that occurs in a region of diffusion between two magnetized plasmas, where the frozen-in condition[15] for the magnetic field is not longer valid.

The solar wind carries a magnetic field of solar origin that, near the Earth's orbit, has an intensity of a few nT and a direction that follows the Parker spiral[16].

This field is very fluctuating, and therefore its north-south component (IMF B_z), which on average is zero, may have for some time both negative and positive values.

When the solar wind encounters the magnetopause, the magnetic field transported by it, is to be contiguous to the inner magnetosphere's one, which in the subsolar region is directed from south to north (the geographic north pole is actually a south magnetic pole).

If the interplanetary magnetic field has a negative z component, there is the possibility of a configuration of fields with opposite polarities, which can give rise to the phenomenon of reconnection. The lines of force antiparallel can reconfigure and reconnect, due to the failure of the frozen-in condition within a zone of "diffusion",

[15] Alfven's theorem and the theorem of Walen describe the so-called *frozen-in condition*. In this case the magnetic field is "frozen" in the fluid, or its magnetic lines are "glued" to the particles, that are always characterized by the same particles, which move with the fluid.

[16] Because of the Sun's rotation and radial motion of the solar wind, IMF expands in the interplanetary medium, forming a spiral, called the *Parker spiral*.

and give rise to the "openness" of the lines of force of Earth's magnetic field, that is, with one end connected to the interplanetary field, which allows the solar wind to flow within the magnetosphere [Gosling et al. 1991].

In the Earth's magnetosphere, magnetic reconnection is driven primarily by the sign and the module of the IMF B_z component, followed in importance by IMF B_y. The longitudinal component (IMF B_x) helps to create the slight asymmetry between the northern and southern hemisphere, favoring reconnection in the north/south hemisphere for negative/positive IMF Bx values [Luhmann et al, 1984].

If the magnetic reconnection occurs, we have the formation of auroras also. In fact the events that we analyzed have produced intense northern lights (i.e., Figure 84).

Figure 84. Aurora of February 18, 2011 in Salluit, Quebec, Canada (photo credit: Sylvain Serre).

CHAPTER 6. *CONCLUSIONS AND FUTURE WORKS*

6.1 Discussion

In this section we summarize the results obtained by our analysis of multi-spacecraft data relevant to the halo CMEs described in the previous sections.

The halo CME occurred on 3 April 2010 was originated in AR NOAA 11059. This AR showed the presence of one main spot and several small pores, while in chromosphere a main filament was lying along the main inversion line. In the AR a B7.4 flare was observed, starting at about 09:04 UT, i.e., few minutes before the observation of the CME from COR1.

The analysis of the magnetic configuration indicated the presence of shearing motions and of emerging flux in the region hosting the main filament. These effects were able to destabilize the filament that started to rise and later erupted. Moreover, the results obtained by the force-free field extrapolation of the field of view encompassing the active region indicates the presence of a system of higher loops resembling the post-flare loops observed in STEREO EUVI images.

The study of the global magnetic configuration of the Sun on 3 April 2010 confirmed the presence of this loop system, clearly visible in all the images (from the different view angles) shown in Figure 45.

The 3D reconstruction of the CME performed using the Tie-Point technique gave us further information on how the CME was evolving during its travel towards the Earth. In particular, we stress the strong resemblance between the images shown in Figure 46 where the 3D reconstruction is reported and the STEREO A/B COR1/COR2 images for what concerns the side views of the CME, and with LASCO for what concerns the Earth-view.

The data on the interplanetary magnetic field concerning the period after the CME initiation show a high variability of the magnetic field components after about two days from the event.

Finally, the analysis of the cosmic ray flux indicates a Forbush decrease after about three days from the CME initiation. So, the effects of this event on the Earth environment are quite strong.

The second event we analyzed is a halo CME occurred on 7 August 2010, related to an M1.0 flare occurred in AR NOAA 11093. Also in this AR we noticed the presence of one main spot (characterized by negative polarity) and several small pores; in the chromosphere several filaments were observed, along a north-east pattern. In this AR the M1.0 flare started at about 17:55 UT, while the CME bright leading edge was observed by STEREO/COR1 instruments about 30 minutes after the flare.

The analysis of the magnetic configuration indicated a quite asymmetric polarity distribution, characterized by a very compact (and strong) negative polarity on the west side and a more diffuse positive polarity on the east side. The force-free field extrapolation limited to the active region area indicates a quite complex configuration, with different bundles of magnetic field lines, characterized by different magnetic connectivity, which could easily become unstable and give rise to the destabilization of the filaments in the active region and to magnetic reconnection.

The study of the global magnetic configuration of the Sun on 7 August 2010 could also evidence the main loop systems in all the images (from the different view angles) shown in Figure 57.

The 3D reconstruction of the CME is in agreement with the images shown in Figure 58 and the STEREO A/B COR1/COR2 images for what concerns the side views of the CME, and with LASCO for what concerns the Earth-view. However, in this case, the CME bright leading edge showed “footpoints” connected on both the north and the south hemispheres, a situation which was not visible in the force-free field extrapolation of the global magnetic field.

The data on the interplanetary magnetic field do not show a high variability of the magnetic field components in the days after the event. Similarly, no clear Forbush decrease was observed after the event. In this respect, it is worthwhile to mention that the estimated velocity for this and the previous CME are very similar (see Table 4).

Events	Flare associated	Active Region (AR)	v_i (km/s)	$v_{15R\odot}$ (km/s)	a (m/s^2)	Fd
April 3, 2010	B7.4 (09:04)	11059 (S23W03)	1000/1100	800	-	yes
August 7, 2010	M1.0 (17:55)	11093 (N12E31)	1000	800	-11,94	no
February 15, 2011	X4.8 (01:56)	11158 (S21W18)	800	570	-18,26	yes

Table 4.

The third halo CME we analyzed occurred on 15 February 2011: it was related to an X4.8 flare which occurred in AR NOAA 11158. This AR was characterized by the presence of several sunspots (both of positive and negative polarity), as well as by several small pores; the chromosphere showed the presence of a bright facular region in the center of the AR and by two filaments at its east and west sides. The X4.8 flare started at 01:44 UT, while the STEREO/COR1 instruments observed the CME bright leading edge about 20 minutes after the flare.

In this case the analysis of the magnetic configuration shows a quite symmetric situation, with a quite balanced polarity distribution. The force-free field extrapolation of the active region area show a lower degree of complexity in comparison with the previous AR analyzed. However, as previously stressed, the high degree of shearing indicated by the inclined field lines, indicate that a a considerable amount of magnetic energy has been stored. The study of the global magnetic configuration of the Sun on 15 February 2011 shows evidence of the main loop systems in all the images (from the different view angles) shown in Figure 71.

Also in this case the 3D reconstruction of the CME is in agreement with the images shown in Figure 72 and the STEREO A/B COR1/COR2 images for what concerns the side views of the CME, and with LASCO for what concerns the Earth-view. Note that also in this case, the CME bright leading edge “footpoints” seem to be connected on

both the north and the south solar hemispheres, (not reproduced in the force-free field extrapolation of the global magnetic field).

The interplanetary magnetic field shows a high variability of the magnetic field components three days after the event, while a strong Forbush decrease is observed 2.5 days after the event.

6.2 Conclusions

In this thesis we have investigated three halo of CMEs using multi-spacecrafts observations.

Firstly, as described in the first and second chapter, we introduce solar phenomena involved in this study and the principal instruments onboard satellites (mostly STEREO).

Secondly, as described in the third chapter, we introduce and explain the technique used for the CME analysis. In chapter four we performed an observational analysis of STEREO/COR1, COR2 data and MDI/SOHO magnetograms for a sample of CMEs during the period February 2010 and May 2011.

The purpose of this research was to acquire information on the link between flare-CME. In particular we considered flares associated with halo CMEs. This was achieved by selecting halo CMEs on LASCO/SOHO and COR1/STEREO catalogues. We found several events, but we limited our analysis to 3 halo CMEs because they best observed from STEREO. Then we investigated the behavior of the magnetic configuration of the active regions.

The main results have been summarized and discussed in the previous Section. From these results we may draw the following main conclusions:

1) The magnetic configuration of the AR originating the flare/CME event can be quite different from one event to the other: in two cases the AR showed only a main spot and several small pores, while in the third case there were several sunspots;
2) The first CME is confined to the southern hemisphere, while the other two seem to involve both hemispheres; in this respect we recall that the first CME

was associated to a B7.4 flare, less energetic than the other two (being M1.0 and X4.8, respectively);

3) the STEREO images, as well as the 3D reconstructions, showed that CMEs that are generally classified as "halo" CMEs in LASCO (front-view) images, appear as confined events in edge-side images, confirming the hypothesis that the halo appearance is mainly due to the point of view of the instrument;
4) the first and the third CMEs gave rise to variability in the IMF and caused Forbush decreases some few days after their occurrence, while the second one did not show any significant impact on the IMF and on the cosmic ray flux. Apparently, for these events there is not a correlation between the flare/CME energetic output and the impact on the Space Weather and on Earth environment.

6.3 Future Works

For the future the goal is 3-D reconstruction of CMEs with COR2 and HI instruments onboard STEREO, in order to study the evolution of the coronal mass ejections up to 1 AU.

Also we want to use the great performance of neural networks and genetic algorithms to create a model of the evolution of CMEs in order to understand the mechanisms that drive the ejection and its interaction with the heliosphere. For such study it is necessary to use a sample of at least twenty CMEs.

For the study of active regions we want to use the magnetograms provided by Helioseismic Magnetic Imager (HMI) onboard SDO, which are still not yet available. These data can provide images similar to MDI but with higher resolution. In this way the problem of the identification of initiation sites of CMEs in the solar corona may be achievable and even their prediction.

Regarding the study on the CR and the space weather, considering a larger sample of events, we will try to understand how some events, having almost the same velocity, but associated to differently energetic flares, can cause or not a change in the IMF and a Forbush decrease.

For space weather we will also try to build a model that, once revealed the ejection, can provide information about the estimated time of arrival to Earth. This is of fundamental importance today for the safety of satellites in Earth orbit, which now exceeds the number of 8000 units.

ACKNOWLEDGEMENTS

I want to first thank O. C. St. Cyr that generated COR1 CME catalog COR1 and then Hong Xie that maintain it.

I thank the CDAW Data Center (NASA) and The Catholic University of America in Cooperation with the Naval Research Laboratory, that generated and maintained the LASCO CME catalog.

I thank the Pierre Auger Observatory for making available its data, as well as all other neutron monitor station used in the thesis. I also thank A. Szabo at NASA/GSFC and CDAWeb for WIND data.

I would like to thank the researcher Marilena Mierla (Institute of Geodynamics, Romana Academy) for her great courtesy and helpfulness, both via email and during the times I've had the pleasure of working with her, in some conferences and in his short stay in Catania.

I thank very much Prof. Francesca Zuccarello for her availability, her comprehension and for her clear guidance on how to deal with problems related to my thesis work.

I thank Prof. Umberto Lombardo, coordinator of the PhD, for his professional and moral support, and Dr. Daniele Spadaro, director of the Astrophysical Observatory of Catania, for having labored to invest some ASI funds for my PhD project. I thank also Prof. Alan Hood for his availability and Dr. Paolo Romano and Dr. Francesco Zuccarello for their cooperation.

I would like to thank my PhD colleagues, in particular Danilo Jaccarino and Manlio De Domenico for their cooperation, two guys who are great physicists as well as being two dear friends.

Finally I would like to thank Dr. Bice Immè of the Scuola Superiore di Catania for her advice, her kindness and her willingness.

BIBLIOGRAPHY

Alissandrakis, C. E., *On the computation of constant alpha force-free magnetic field*, Astron. & Astrophys., 100, 197, 1981.

Aly, J.J., *On some properties of force-free magnetic fields in infinite regions of space*, Astrophys. J., 283, 349–362, 1984.

Amari, T., et al., *A Twisted Flux Rope Model for Coronal Mass Ejections and Two-Ribbon Flares*, Astrophys. J. Lett., 529, L49–L52, 2000.

Andrews, M.D., *The Front-to-Back Asymmetry of Coronal Emission*, Solar Phys., 208, 317–324, 2002.

Antiochos, S. K., *Structures and flows in coronal loops, in: A Physics of magnetic flux rope* (A92-31201, 12-75), Washington DC, Amer. Geophy. Union, 203-210, 1990.

Antiochos, S. K., DeVore, C. R., e Klimchuk, J. A., *A model for solar coronal mass ejections*, The Astrophysical Journal, 510, 485-493, 1999.

Antiochos, S. K., Karpen J. T., DeVore, C. R., *Coronal magnetic field relaxation by null-point reconnection*, The Astrophysical Journal, 575, 578-584, 2002.

Billings, D.E., *A Guide to the Solar Corona*, Academic Press, New York, 1966.

Byrne, J.P., et al., *Propagation of an Earth-directed coronal mass ejection in three dimensions*, Nature Commun., 1, 74, 2010.

Brueckner et al., *The Large Angle Spectroscopic Coronagraph (LASCO)*, Solar Phys., 162, 357-402, 1995.

Buffington, A., Jackson, B.V., Korendyke, C.M., Applied Optics, 35, 6669-6673, 1996.

Cane, H. V., Reames, D. V., and von Rosenvinge, T. T., *The Role of Interplanetary Shocks in the Longitude Distribution of Solar Energetic Particles*, J. Geophys. Res. 93, 9555–9567, 1988.

Cane, H.V., *Coronal Mass Ejections and Forbush Decreases*, Space Sci. Rev., 93, 55, 2000.

Chen, J., *Theory of prominence eruption and propagation: Interplanetary consequences*, J. Geophys. Res., 101, 27,499–27,520, 1996.

Chen P. F., *Coronal Mass Ejections: Models and Their Observational Basis*, Living Rev. Solar Phys., 8, (2011), 1.

Chen, J. and Krall, J., *Acceleration of coronal mass ejections*, J. Geophys. Res., 108(A11), 1410, 2003.

Forbes, T.G., *A review on the genesis of coronal mass ejections*, J. Geophys. Res., 105, 23,153–23,166, 2000.

Forbush, S.E., *On the Effects in Cosmic Ray Intensity Observed During the Recent Magnetic Storm*, Phys. Rev., 51, 1108–1109, 1937.

Gary, G.A., *Plasma Beta above a Solar Active Region: Rethinking the Paradigm*, Solar Phys., 203, 71–86, 2001.

Gilbert, H. R., et al., *Narrow Coronal Mass Ejections*, The Astrophysical Journal, 550, 1093-1101, 2001.

Gopalswamy, N. and Kundu, M.R., *Estimation of the mass of a coronal mass ejection from radio observations*, Astrophys. J. Lett., 390, L37–L39, 1992.

Gopalswamy, N., Lara, A., Yashiro, S., Nunes, S. and Howard, R.A., *Coronal mass ejection activity during solar cycle 23*, in Solar Variability as an Input to the Earth's Environment, International Solar Cycle Studies (ISCS) Symposium, 23 – 28 June 2003, Tatransk´a Lomnica, Slovak Republic, (Ed.) Wilson, A., vol. SP-535 of ESA Special Publication, pp. 403–414, ESA Publications Division, Noordwijk, 2003.

Gosling, J. T., McComas, D. J., Philips, J. L., & Bame, S. J., *Geomagnetic Activity Associated with Earth Passage of Interplanetary Shock Disturbances and Coronal Mass Ejections*, J. Geophys. Res., 96, 783, 1991.

Hapgood, M.A., *Space Physics Coordinate Transformations: A User Guide*, Planet. Space Sci. 40, 711-717, 1992.

Haurwitz, M.W., Yoshida, S., and Akasofu, S. I., *Interplanetary Magnetic Field Asymmetries and Their Effects on Polar Cap Absorption Events and Forbush Decreases*, J. Geophys. Res., 70, 2977–2988, 1965.

Howard, R.A., Michels, D.J., Sheeley Jr, N.R. and Koomen, M.J., *The observation of a coronal transient directed at earth*, Astrophys. J. Lett., 263, L101–L104, 1982.

Howard, R.A., et al., *Sun Earth Connection Coronal and Heliospheric Investigation (SECCHI)*, Space Sci. Rev. 136, 67, 2008.

Hudson, H.S., Acton, L.W. and Freeland, S.L., *A Long-Duration Solar Flare with Mass Ejection and Global Consequences*, Astrophys. J., 470, 629, 1996.

Hudson, H.S. and Cliver, E.W., *Observing coronal mass ejections without coronagraphs*, J. Geophys. Res., 106, 25, 199–25, 214, 2001.

Hundhausen, A.J., *Sizes and Locations of Coronal Mass Ejections: SMM Observations From 1980 and 1984–1989*, J. Geophys. Res., 98(A8), 13,177–13,200, 1993.

Jackson, B.V., *Imaging of coronal mass ejections by the HELIOS spacecraft*, Solar Phys., 100, 563–574, 1985

Inhester, B., *Stereoscopy basics for the STEREO mission*, Publ. Int. Space Sci. Inst., astro-ph/0612649, 2006.

Kivelson, M. G., e Russell, C. T., *Introduction to space physics* (CUP, 1995).

Koomen, M. J., Detwiler, C. R., Brueckner, G. E., Cooper, H. W., & Tousey, R., Appl. Opt., 14, 743, 1975.

Krall, J., Chen, J., Duffin, R.T., Howard, R.A. and Thompson, B.J., *Erupting Solar Magnetic Flux Ropes: Theory and Observation*, Astrophys. J., 562, 1045–1057, 2001.

Krall, J., Yurchyshyn, V.B., Slinker, S., Skoug, R.M. and Chen, J., *Flux Rope Model of the 2003 October 28-30 Coronal Mass Ejection and Interplanetary Coronal Mass Ejection*, Astrophys. J., 642, 541–553, 2006.

Lara, A., Gopalswamy, N., Xie, H., Mendoza-Torres, E., P´erez-Er´ıquez, R. and Michalek, G., *Are halo coronal mass ejections special events?*, J. Geophys. Res., 111, 6107, 2006.

Lin, J., Forbes, T.G., Isenberg, P.A. and Demoulin, P., *The Effect of Curvature on Flux-Rope Models of Coronal Mass Ejections*, Astrophys. J., 504, 1006. 1998.

Liu et al, 2011.

Lyot, B., *The study of the solar corona and prominences without eclipses* (George Darwin Lecture, 1939). Mon. Not. Royal Astron. Soc., 99, 580–594, 1939.

Low, B.C., *Solar Activity and the Corona*, Solar Phys., 167, 217–265, 1996.

Low, B.C. and Zhang, M., *The Hydromagnetic Origin of the Two Dynamical Types of Solar Coronal Mass Ejections*, Astrophys. J. Lett., 564, L53–L56, 2002.

Luhmann, J. G., Walker, R. J., Russell, C. T., Crooker, N. U., Spreiter, J. R., e Stahara, S. S., *Patterns of potential magnetic field merging sites on the dayside magnetopause*, J. Geophys. Res., 89, 1739–1742, 1984.

Manchester IV, W.B., Gombosi, T.I., Roussev, I., Ridley, A., De Zeeuw, D.L., Sokolov, I.V., Powell, K.G. and T´oth, G., *Modeling a space weather event from*

the Sun to the Earth: CME generation and interplanetary propagation, J. Geophys. Res., 109, A02107, 2004.

Mierla, M., et al., *A Quick Method for Estimating the Propagation Direction of Coronal Mass Ejections using STEREO-COR1 Images*, Solar Phys., 252, 385–396, 2008.

Mierla, M., et al., *On 3D Reconstruction of Coronal Mass Ejections: I Method description and application to SECCHI-COR Data*, Solar Phys., 259, 123–141, 2009.

Pariat, E., Demoulin, P., and Berger, M. A., *Photospheric flux density of magnetic helicity*, Astron. & Astrophys., 439, 1191, 2005.

Parker, E. N., *Dynamics of the Interplanetary Gas and Magnetic Fields*, Astrophys. Journal, 128, 664, 1958.

Pierre Auger collaboration, *The Pierre Auger Observatory scaler mode for the study of solar activity modulation of galactic cosmic rays*, JINST, 6, P01003, 2011

Priest, E. R., *Solar Magnetohydrodinamics*, D. Reidel Publishing Company, 1984.

Raychaudhuri, P., *Variability of Coronal Mass Ejections*, in Coronal and Stellar Mass Ejections, Beijing, China, September 13 – 17, 2004, (Eds.) Dere, K., Wang, J., Yan, Y., vol. 226 of IAU Symposia, pp. 211–212, Cambridge University Press, Cambridge; New York, 2005.

Robbrecht, E., Berghmans, D. and Van der Linden, R.A.M., *Automated LASCO CME Catalog for Solar Cycle 23: Are CMEs Scale Invariant?*, Astrophys. J., 691, 1222–1234, 2009.

Schuck, P. W., *Local Correlation Tracking and the Magnetic Induction Equation*, ApJ, 632, L53, 2005.

Schwenn, R., et al., *First view of the extended green-line emission corona at solar activity minimum using the LASCO-C1 coronograph on SOHO*, Solar Physics, 175, 667-684, 1997.

Sheeley Jr., N. R., et al., *Measurements of flow speeds in the corona between 2 and 30* R_{Θ}, Astrophysical Journal, 484, 472-478, 1997.

Stern, R. A., et al., Proc. SPIE, 5171, 77, 2004

Thompson, W.T., et al., in Keil, S.L., Avakyan, S.V. (eds.) *Innovative Telescopes and Instrumentation for Solar Astrophysics, Proc. SPIE*, 4853, 1, 2003.

Thompson, W.T., *Coordinate systems for solar image data*, Astron. & Astrophys., 449, 791, 2006.

Trucco, E. and Verri, A., *Introductory Techniques for 3-D Computer Vision*, Prentice Hall, New Jersey, 1998.

Vial, J.-C., et al., *SMESE: A SMall Explorer for Solar Eruptions*, Adv. Space Res., 40, 1787–1801, 2007.

Vourlidas, A., Buzasi, D., Howard, R.A. and Esfandiari, E., *Mass and energy properties of LASCO CMEs*, in Solar Variability: From Core to Outer Frontiers, Proceedings of the 10th European Solar Physics Meeting, Prague, Czech Republic, 9 – 14 September 2002, (Ed.) Wilson, A., vol. SP-506 of ESA Conference Proceedings, pp. 91–94, ESA Publications Division, Noordwijk, 2002.

Vourlidas, A., Wu, S.T., Wang, A.H., Subramanian, P. and Howard, R.A., *Direct Detection of a Coronal Mass Ejection-Associated Shock in Large Angle and Spectrometric Coronagraph Experiment White-Light Images*, Astrophys. J., 598, 1392–1402, 2003.

Wang, Y.-M., Sheeley Jr, N.R., Socker, D.G., Howard, R.A., Brueckner, G.E., Michels, D.J., Moses, D., St Cyr, O.C., Llebaria, A. and Delaboudini`ere, J.-P., *Observations of Correlated White-Light and Extreme-Ultraviolet Jets from Polar Coronal Holes*, Astrophys. J., 508, 899–907, 1998.

Webb, D.F. and Howard, R.A., *The solar cycle variation of coronal mass ejections and the solar wind mass flux*, J. Geophys. Res., 99(A3), 4201–4220, 1994.

Wu, S.T., Zhang, T.X., Tandberg-Hanssen, E., Liu, Y., Feng, X. and Tan, A., *Numerical Magnetohydrodynamic Experiments for Testing the Physical Mechanisms of Coronal Mass Ejections Acceleration*, Solar Phys., 225, 157–175, 2004.

Yashiro, S., Gopalswamy, N., Michalek, G., St Cyr, O.C., Plunkett, S.P., Rich, N.B. and Howard, R.A., *A catalog of white light coronal mass ejections observed by the SOHO spacecraft*, J. Geophys. Res., 109, 7105, 2004.

Zhang, Q.-M., Guo, Y., Chen, P.F., Ding, M.-D. and Fang, C., *Why are halo coronal mass ejections faster?*, Res. Astron. Astrophys., 10, 461–472, 2010.